UNIVERSITY OF CALIFORNIA SAN DIEGO

SAN DIEGO STATE UNIVERSITY

Sensitive Multi-Photon Laser Wave-Mixing Detection Methods Interfaced to Microfluidics for Cancer Biomarkers Using Thin Samples

A Dissertation submitted in partial satisfaction of the requirements
for the degree Doctor of Philosophy

in

Chemistry

by

Jie Liang

Committee in charge:

University of California San Diego

Professor John E. Crowell
Professor Mark Young

San Diego State University

Professor William G. Tong, Chair
Professor Gregory Holland
Professor Fletcher J. Miller

2023

The Dissertation of Jie Liang is approved, and it is acceptable in quality and form for publication on microfilm and electronically.

_____

_____

_____

_____

_____

Chair

University of California San Diego

San Diego State University

2023

DEDICATION

This dissertation is dedicated to my Father, Xinsheng Liang,

Mother, Xiaoyan Huang,

and all I love

EPIGRAPH

"You have to stay in school. You have to. You have to go to college. You have to get your degree. Because that's the one thing people can't take away from you is your education. And it is worth the investment."

Michelle Obama

TABLE OF CONTENTS

LIST OF ABBREVIATIONS

APTES	(3-Aminoprpyl)triethoxysilane
BCA	bicinchoninic acid
BGE	background electrolyte
BNP	brain natriuretic peptide
BSA	bovine serum albumin
CA 19-9	carbohydrate antigen 19-9
CE	capillary electrophoresis
CGE	capillary gel electrophoresis
CHES	2-(Cyclohexylamino)ethanesulfonic acid
CIEF	capillary isoelectric focusing
CITP	capillary isotachophoresis
CLIA	chemiluminescence immunoassay
CMC	critical micelle concentration
CSE	capillary sieving electrophoresis
CT	computed tomography
CZE	capillary zone electrophoresis
DFWM	degenerate four-wave mixing
DMF	dimethylformamide
DPSSL	diode-pumped solid-state laser
ECLIA	electrochemiluminescence immunoassay
EDC	1-ethyl-3-[3-dimethylaminopropyl] carbodiimide

ELISA	enzyme-linked immunosorbent assay
EOF	electroosmotic flow
ER	estrogen receptor
ERCP	endoscopic retrograde cholangiopancreatography
EUS	endoscopic ultrasound
FASS	field-amplified sample stacking
FDA	US Food and Drug Administration
F-DFWM	forward-scattering degenerate four-wave mixing
FITC	fluorescein isothiocyanate
HER-2	human epidermal growth factor receptor-2
HIV	human immunodeficiency virus
HPLC	high-performance liquid chromatography
IHC	immunohistochemistry
IR	infrared
ISH	in-situ hybridization
MASER	microwave amplification by stimulated emission of radiation
MEKC	micellar electrokinetic chromatography
MRCP	magnetic resonance cholangiopancreatography
MRI	magnetic resonance imaging
NHS-Rhodamine	5-(and 6)-carboxy tetramethylrhodamine, succinimidyl ester
PAGE	polyacrylamide gel electrophoresis
PBS	phosphate-buffered saline
PEG	polyethylene glycol

PEO	poly (ethylene oxide)
PET	positron emission tomography
RF	radio frequency
PR	progesterone receptor
SDS	sodium dodecyl sulfate
SHG	second-harmonic generation
SPECT	single photon emission computed tomography
Sulfo-NHS	N-hydroxysulfosuccinimide
Tris	tris(hydroxymethyl)aminomethane
UV	ultraviolet

LIST OF FIGURES

LIST OF TABLES

ACKNOWLEDGMENTS

I deeply appreciate my parents for their financial and spiritual supports throughout my life. I am the luckiest person growing up with loving parents. I would also like to acknowledge my family member Yiheng Yuan and my handsome husky Xenon for their endless emotional support. Thank you to my aunt, Liya Liang, for hosting me while I was studying in community college.

I also truly appreciate my Ph.D. mentor Dr. William G. Tong. You are not only the one who teaches me laser wave mixing, but also the one who demonstrates what ingenuity and dedication are. Thank you for providing the materials I needed to finish my research and showing your care for me. I would also like to acknowledge all the members of Dr. Tong's research lab for their contribution and for sharing their knowledge. Thank you to the people I directly worked with, including James Suprapto, Alexander R. Jackson, Zarina Munshi, Mya Brown, Megan Murphy, Jessica Maness, Vanessa Frausto, Irving Chavez, and more. You are amazing people, and it is joyful to work with you.

Last, my lovely friends have provided valuable academic and emotional support. Xiaoyu Li, Jiawei Zhao, Zhangxue Feng, Xintong Lin, Hoi Ki Chan, Melody Yeh, Jiarong Wu, Cheng Tsai, Jeffrey Tseng, Savio Luk, Bella Jiang, Jun Liao, Guanghui Deng, Jingyi Huang, Yan Ng, Wei He, Fei Yu, David Sung, Camila Lee, Daniel Ding, Xiaoxin Kuang, Guobao Hu. The moments we spent together all come to my mind when I wrote down your names here. Although I rarely contact some of you, it has been my pleasure to know you throughout these years.

Chapter 3, in part, has been submitted for publication of the material as it may appear in ACS Omega, 2023. Jie Liang, and William G. Tong, 2023. The dissertation author was the primary investigator and author of this manuscript.

Chapter 4, in part, is a reprint of the material as it appears in SPIE Proceedings, 2019. Jie Liang, James Suprapto, Samantha Crawford, and William G. Tong, 2019. The dissertation author was the primary investigator and author of this manuscript.

Chapter 4, in part, has been submitted for publication of the material as it may appear in ACS Omega, 2023. Jie Liang, and William G. Tong, 2023. The dissertation author was the primary investigator and author of this manuscript.

Chapter 5, in part, is currently being prepared for submission for publication of the material. Jie Liang, and William G. Tong, 2023. The dissertation author was the primary investigator and author of this manuscript.

VITA

2015 Bachelor of Science in Pharmaceutical Chemistry
University of California, Davis

2023 Doctor of Philosophy in Chemistry
University of California San Diego
San Diego State University

PUBLICATIONS

Liang, J., Suprapto, J., Crawford, S., & Tong, W. G. (2019). Sensitive multi-photon nonlinear laser wave-mixing detection of cancer and heart failure biomarkers. *Proc SPIE, 11105*. https://doi.org/10.1117/12.2529899

Liang, J., & Tong, W. G. Ultrasensitive Detection and Separation of Pancreatic Cancer Biomarker CA 19-9 Using Multi-Photon Laser Wave-Mixing Detector Interfaced to Capillary Electrophoresis. Accepted and In Print *ACS Omega (2023)*

Liang, J., & Tong, W. G. Exploring the Potential for Detecting Biomarkers on Surface or Microarray Using Laser Wave Mixing Spectroscopy. Manuscript to be submitted

ORAL PRESENTATIONS AND INVITED LECTURES

"Sensitive Analysis of Cancer Biomarkers Using Laser Wave-Mixing Detector Interfaced to Microfluidics," Liang, J., Suprapto, J., Tong, W. G., SDSU Student Research Symposium, San Diego, CA, 2022.

"Novel detection of cancer biomarkers using nonlinear multi-photon laser wave-mixing detector interfaced to microfluidics," Liang, J., Suprapto, J., Tong, W. G., ACS Spring 2022, San Diego, CA, 2022.

"Ultrasensitive Detection of Pancreatic Cancer Biomarker CA 19-9 Using Capillary Electrophoresis-Coupled Laser Wave-Mixing Detection," Liang, J., Miramar College, San Diego, 2019.

SELECTED POSTER PRESENTATIONS

"Ultrasensitive Detection of Breast Cancer Biomarker HER2 Using Laser Wave-Mixing Detector Interfaced to Microfluidics," Liang, J., Suprapto, J., Maness, J., Tong, W. G., 32nd Annual CSU Biotechnology Symposium, Santa Clara, 2020

"Sensitive Analysis of Breast Cancer Biomarkers Using Laser Wave-Mixing Detector Interfaced to Microfluidics," Liang, J., Suprapto, J., Crawford, S., Tong, W. G.,257th Fall 2019 ACS National Meeting, San Diego, CA, 2019.

"Novel Detection of Biomarkers of Pancreatic Cancer Using Nonlinear Multi-Photon Laser Detectors Interfaced to Separation Techniques," Liang, J., Pradel, J. S., Tong, W. G., 253rd ACS National Meeting, San Francisco, CA, 2017.

"Sensitive Detection of Biomarkers for Multiple Sclerosis (MS) Using Nonlinear Multi-Photon Laser Methods," Liang, J., Jackson, A., Tong, W. G., SDSU Student Symposium, San Diego, CA, 2016.

FIELD OF STUDY

Major Field: Analytical Chemistry

Studies in Laser Wave-Mixing Spectroscopy and Separation Science

Professor William G. Tong, Chair

ABSTRACT OF THE DISSERTATION

Sensitive Multi-Photon Laser Wave-Mixing Detection Methods Interfaced to Microfluidics for Cancer Biomarkers Using Thin Samples

by

Jie Liang

Doctor of Philosophy in Chemistry

University of California San Diego, 2023

San Diego State University, 2023

Professor William G. Tong, Chair

Nonlinear laser wave mixing is presented as a highly sensitive absorption-based detection method for biomarkers in a capillary electrophoresis system, and on glass surfaces or microscope slides. It offers significant advantages, including outstanding sensitivity and selectivity levels, high spatial resolution, small sample volume requirement, small probe volume (nL to pL), and portable and compact designs. Different laser wave-mixing detectors can be interfaced to capillary electrophoresis systems for enhanced chemical selectivity and microscope glass slides for inexpensive and fast detection of millimeter-thin samples.

Laser wave-mixing detection interfaced with capillary electrophoresis further enhances detection sensitivity by on-line sample concentration methods. Selectivity levels are improved by separating excess labels or dyes from dye-conjugated proteins. Different modes of capillary electrophoresis can be used to separate proteins and biomarkers, including capillary zone electrophoresis, micellar electrokinetic chromatography, and capillary sieving electrophoresis.

Since wave mixing is an absorption-based detection method, one can use both fluorophores and chromophores to label proteins and biomarkers. For example, Chromeo P503 and Chromeo P540 are used to label pancreatic cancer biomarker CA 19-9 with the optimal molar ratio of dye to protein. The concentration and mass detection limits for CA 19-9 are determined to be 0.0090 U/mL and 6.8 x 10^{-10} U, respectively. Colorimetric assays (Bradford assay and BCA assay) are used to quantify CA 19-9, and the corresponding concentration and mass detection limits for CA 19-9 are determined to be 75 pM (picomolar) and 5.6 zeptomole, respectively.

This study also demonstrates ultrasensitive detection of biomarkers held between microscope glass slides or air-dried on a microscope slide for convenient and fast detection of biomarkers and viruses. Preliminary concentration and mass detection limits are determined to be 160 U/mL and 680 attomole for CA 19-9; 40 ng/mL and 91 zeptomole for human epidermal growth factor receptor 2; and 125 pg/mL and 1 zeptomole for HIV-1 p24 antigen.

CHAPTER 1

INTRODUCTION

1.1 Basis of Lasers

1.1.1 History of Lasers

Max Planck discovered the relationship between the frequency of radiation and energy. Additionally, he introduced the concept of a quantum (a discrete amount of energy). Inspired by Max Planck, Einstein concluded that radiation could be quantified as photons (discrete amounts of electromagnetic radiation), and he built the theoretical foundation for stimulated emission in 1916. An incident photon stimulates the emission of a new photon by interacting with atoms or molecules in excited states. The incident and new photons have the same frequency, phase, amplitude, polarization, and direction (Einstein 1916).

Charles Hard Townes and his group brought Einstein's theory into reality by producing the first microwave amplification by stimulated emission of radiation (MASER) in 1955 (Gordon *et al.*, 1955). In 1960, Theodore H. Maiman constructed the first laser using synthetic ruby. High-energy photographic light flashes stimulated this laser's gain medium (Alster, 2000). Various types of lasers using different lasing media, such as solid, gaseous, and semiconductors, were invented in the 1960s.

The improvement of laser technology and the invention of new lasers have never stopped (Gianfaldoni *et al.*, 2017). Lasers are widely used in spectroscopy, such as Ramen spectroscopy and cavity ring-down spectroscopy, and in laser-induced fluorescence, among many other applications.

1.1.2 Components of Lasers

As shown in Figure 1-1, a laser (e.g., gas laser) consists of three essential components: a pumping source, lasing medium, and an optical resonator. Pumping can be accomplished using optical sources (e.g., lamps or other lasers) or electrical sources (e.g., an electrical current or discharge). The pumping source activates the lasing medium by transferring external energy into the medium. The lasing medium can be made of a solid crystal, a semiconductor, an aqueous solution, or a gas. It plays a crucial role in retaining population inversion and stimulated emission. An optical resonator (e.g., composed of mirrors or reflectors) causes photons generated by stimulated emission to bounce back and forth into the laser medium multiple times to achieve further amplification. One side of the resonator is a partially transmitting reflector ($R<1$) that enables the emission of the laser output beam. The output beam is parallel because the nonparallel radiation travels out of the medium after multiple reflections (Black & Jobling, 2014).

1.1.3 Mechanism of Laser Processes

The word "laser" is an acronym for "light amplification by stimulated emission of electromagnetic radiation." Laser action includes three main processes. The first is pumping. Figure 1-2a shows that two electrons are excited by external energy from the lower electronic energy state (E_0), and the higher electronic energy level (E_1) is populated. Figure 1-2b shows that the two electrons in E_1 undergo spontaneous emission. The wavelength of this emission is $\lambda = hc/(E_1-E_0)$, where c is the speed of light in free space, and h is Planck's constant. The emitted photons have different directions and phases. Thus, the radiation is monochromatic but not coherent. The stimulated emission process is shown in Figure 1-2c. This is the critical process of laser action. A photon generated from the previous process strikes the electrons in E_1 with an

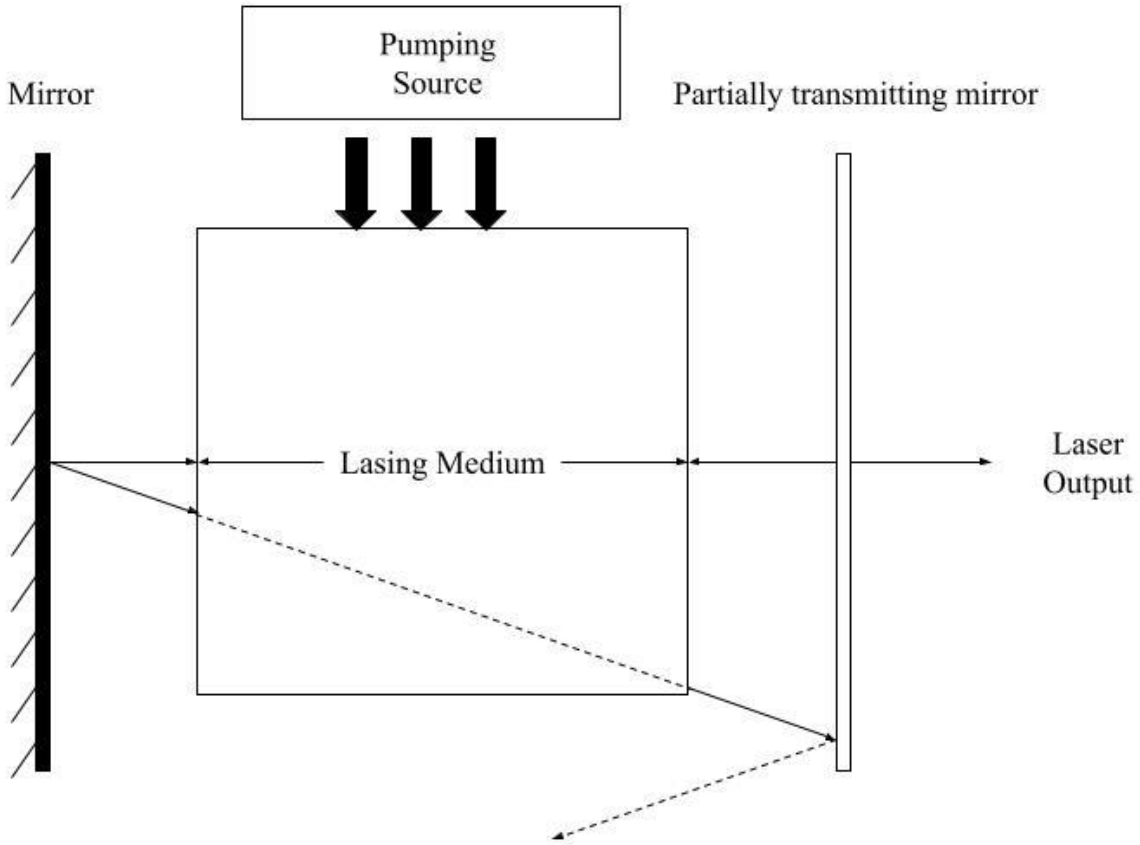

Figure 1-1 Design of a laser, including a pumping source, a lasing medium, and an optical resonator.

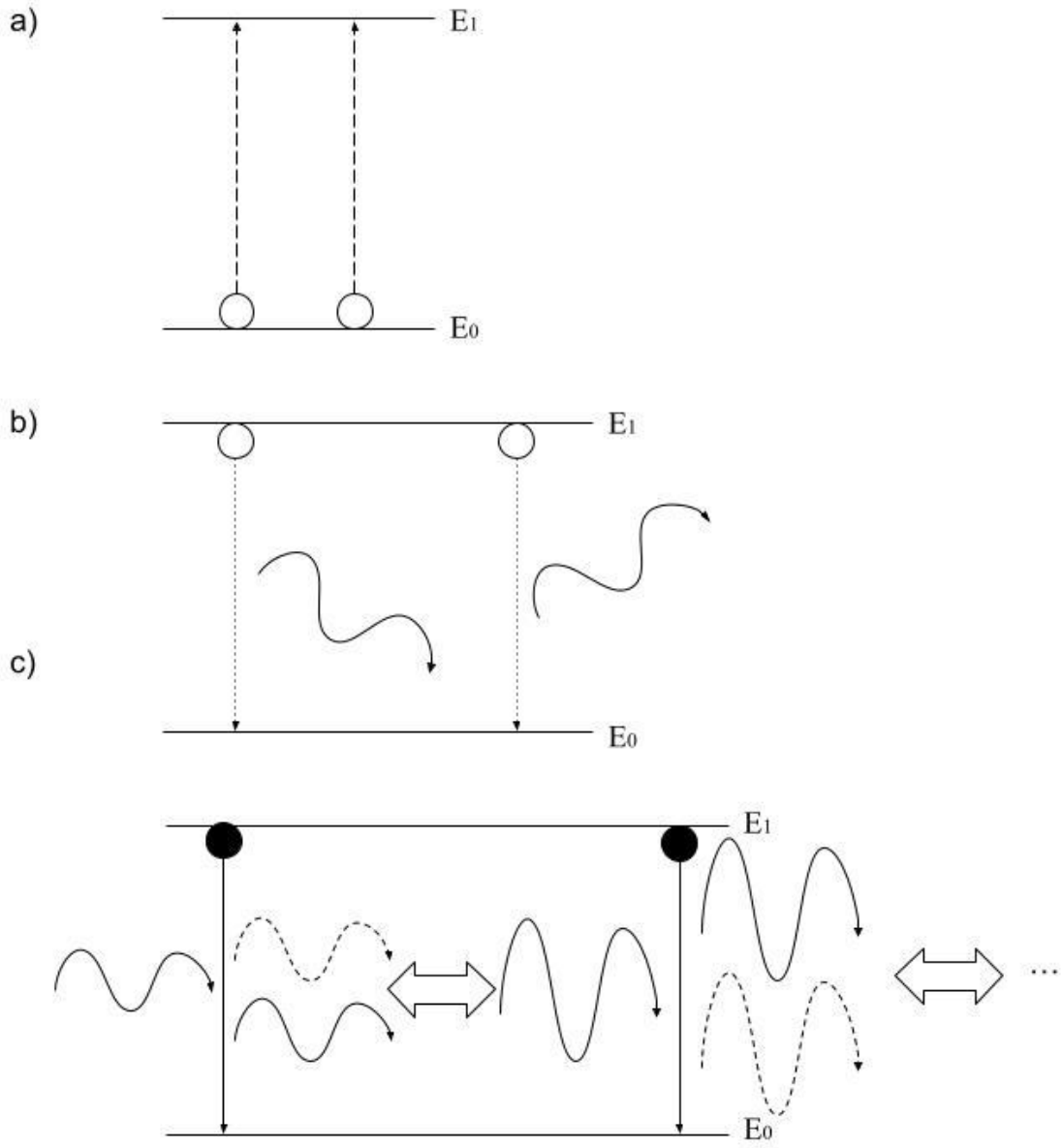

Figure 1-2 Three main processes of laser action—a) pumping, b) spontaneous emission, and c) stimulated emission. The solid dots represent electrons that stay at the energy level for a longer time, and the hollow dots represent electrons that remain at the energy level for a short time. The solid lines represent stimulated emission.

energy of (E_1-E_0) and induces the emission of a new photon. The new photon has the same travel path and phase as the original photon that induced the emission. The electromagnetic radiation is amplified and causes further stimulated emission. The resulting light is coherent (Skoog *et al.*, 2014). The solid dots represent electrons that stay at the energy level for longer, whereas the hollow dots represent electrons that remain at the energy level for a short time. The solid lines represent stimulated emission.

Population inversion guarantees that the number of photons generated by stimulated emission is larger than the number of photons absorbed. To achieve population inversion, the number of electrons in the higher energy level must be larger than the number of electrons in the lower energy level so that a net gain in emitted photons is generated (Meyers, 2001).

1.1.4 Rate Equations and Threshold Condition

According to Mitofsky (2018), the rates of absorption, spontaneous emission, and stimulated emission can be modeled as follows:

$$\text{Absorption: } \frac{dN_1}{dt} = B_{01}N_0u \qquad (1-1)$$

$$\text{Spontaneous emission: } \frac{dN_1}{dt} = -A_{10}N_1 \qquad (1-2)$$

$$\text{Stimulated emission: } \frac{dN_1}{dt} = -B_{10}N_1u \qquad (1-3)$$

N_0 and N_1 are population densities in the lower and upper states ($N_1 > N_0$). A_{10} is Einstein A coefficient, and it has units of s^{-1}. B_{01} and B_{10} are the Einstein B coefficients and have units of $m^3 \cdot J^{-1} \cdot s^{-2}$. u, in units of $J \cdot s \cdot m^{-3}$, is the radiation density for inducing a transition between the lower state and upper state:

$$u = \frac{8\pi f^2}{c^3} \times \frac{hf}{e^{\left(\frac{hf}{KT}\right)-1}} \qquad (1-4)$$

where f is the frequency in Hz, c is the speed of light, h is Planck's constant, K is the Boltzmann constant, and T is the temperature in degrees Kelvin. At equilibrium, the total rate of absorption, spontaneous emission, and stimulated emission is zero because the rate of absorption (i.e., population of the excited state) equals the rate of spontaneous and stimulated emission (i.e., depopulation of the excited state). Therefore,

$$B_{01}N_0u - B_{10}N_1u = A_{10}N_1 \qquad (1-5)$$

Hence,

$$u = \frac{A_{10}}{\frac{N_0}{N_1}B_{01} - B_{10}} \qquad (1-6)$$

The population distribution is represented by an ideal thermal Boltzmann distribution as

$$\frac{N_1}{N_0} = \frac{g_1}{g_0}e^{\frac{-hv}{KT}} \qquad (1-7)$$

where g_0 and g_1 are the numbers of ways that electrons can occupy an energy state (i.e., the statistical weights of an energy level with total angular momentum quantum number J). According to Equation 1-6 and Equation 1-7, u can be rewritten as

$$u = \frac{A_{10}}{\frac{g_0}{g_1}e^{\frac{-hf}{KT}}B_{01} - B_{10}} \qquad (1-8)$$

$$u = \frac{\frac{A_{10}}{B_{10}}}{\frac{g_0B_{01}}{g_1B_{10}}e^{\frac{-hf}{KT}} - 1} \qquad (1-9)$$

Equation 1-9 holds only if both Equations 1-10 and 1-11 are valid:

$$g_0B_{01} = g_1B_{10} \qquad (1-10)$$

and

$$\frac{A_{10}}{B_{10}} = \frac{8\pi h f^3}{c^3} \qquad (1-11)$$

Now, the total rate of change of the population density of the upper state with respect to time is:

$$\frac{dN_1}{dt} = -A_{10}N_1 + B_{01}N_0 u - B_{10}N_1 u = -A_{10}N_1 - B_{10}u\left(N_1 - \frac{g_2}{g_1}N_0\right) \qquad (1-12)$$

Lasing and amplification occur only if the term in parenthesis in Equation 1-12 is larger than zero. According to the Beer-Lambert law,

$$I_1 = I_0 e^{-(2\alpha L+\gamma)} \qquad (1-13)$$

where L is the length of the resonator and γ is the loss factor of one round trip due to reflection, absorption, and diffraction. The electromagnetic wave is amplified by a factor of $e^{-(2\alpha L+\gamma)}$. The absorption coefficient α depends on the absorption cross-section σ:

$$\alpha = [N_1 - (g_1/g_0)\, N_0]\, \sigma \qquad (1-14)$$

To achieve amplification, the gain factor is

$$e^{-\left(2\left[N_0 - \left(\frac{g_0}{g_1}\right)N_1\right]\sigma L+\gamma\right)} > 1 \qquad (1-15)$$

Hence, according to Demtröder, the threshold condition is

$$[N_1 - (g_1/g_0)\, N_0] > \frac{\gamma}{2\,\alpha\, L} \qquad (1-16)$$

During laser action, the population distribution deviates from an ideal thermal Boltzmann distribution (Demtröder, 2018). In other words, achieving population inversion in a two-level laser system is very energy costly and unsteady. The pumping transition must work against the lasing transition. Therefore, three- and four-level laser systems are more practical.

1.1.5 Three- and Four-Level Lasers

Figure 1-3 shows energy level diagrams of three- and four-level laser systems. For three-level laser system (Figure 1-3a), the energy states satisfy $E_0 < E_1 < E_2$, and the lifetimes of the energy states satisfy $\tau_1 > \tau_2$. E_1 is called a metastable state because of its long lifetime. More than 50% of the electrons need to be excited to E_2 by providing sufficient energy, and then they quickly decay to E_1. Hence, population inversion between E_0 and E_1 and stimulated emission occur.

For the four-level system (Figure 1-3b), the energy states satisfy $E_0 < E_1 < E_2 < E_3$, and the lifetimes of the energy states satisfy $\tau_2 > \tau_1 \approx \tau_3$. E_2 is the main metastable state. Laser radiation depends on the transition between E_1 and E_2. The lifetime of E_1 is very short, so the number of electrons in this state is negligible. Therefore, population inversion is achieved easily (Pearsall, 2017).

1.2 Advantages of Lasers in Spectroscopy

Laser beams have the unique characteristics of monochromaticity, spatial and temporal coherence, directionality, and brightness. These characteristics distinguish laser beams from light produced from ordinary light sources. In addition, these features make lasers highly useful for spectroscopic instruments because lasers act as light sources for various spectroscopies, enhancing sensitivity and selectivity.

1.2.1 Monochromaticity

Existing lasers can cover a significant portion of the electromagnetic spectrum extending from the ultraviolet spectral region to the mid-infrared spectral region. The laser gain medium determines the wavelength. Laser light comes from stimulated emission from one set of energy levels. Lasers have a much smaller bandwidth than other light sources. Although the laser light is nearly monochromatic, it is not ideally monochromatic because a perfect monochromatic

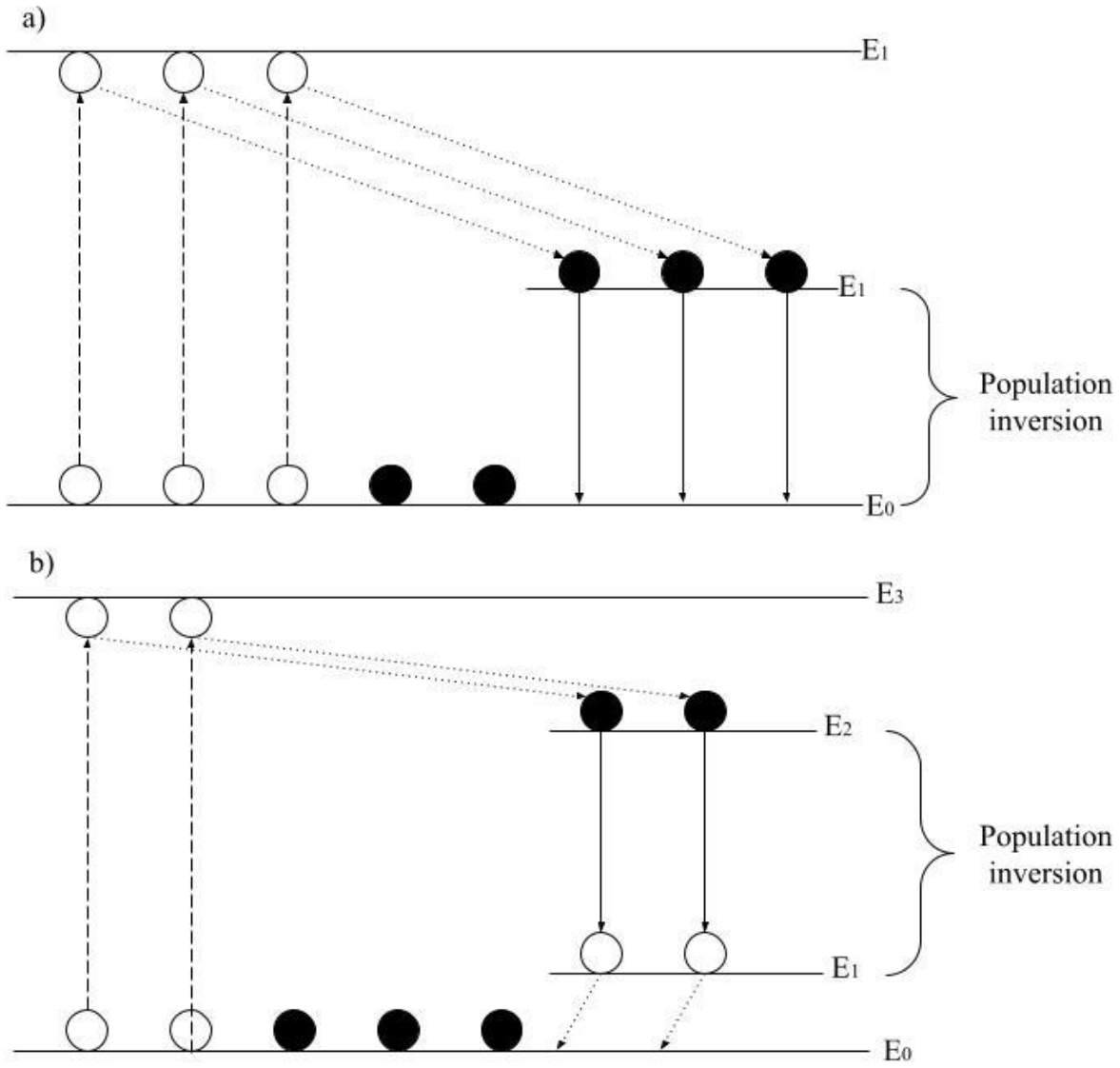

Figure 1-3 Energy level diagrams of a) three- and b) four-level laser systems. The solid dots represent electrons that stay at the energy level for a longer time, and the hollow dots represent electrons that remain at the energy level for a short time. The solid lines represent stimulated emission.

laser would violate the time-energy uncertainty principle. Based on this principle, if the wavelength of a laser is confirmed with no doubt, the laser must have been on forever and will be on forever (Hitz *et al.*, 2012). In our lab, highly monochromatic lasers enhance selectivity in chemical analysis.

1.2.2 Coherence

Unlike ordinary white light sources that emit light waves in all directions, laser-emitted light waves that are in phase in terms of location (spatial coherence) and time (temporal coherence). The coherent laser output is from the stimulated emission process. Spatial (transverse) coherence means that the light waves at the top and the bottom of the beam are in phase as they travel a certain distance. Temporal (longitudinal) coherence means that light waves stay in phase as they move past a certain point. The temporal coherence time (τ_c) and the temporal coherence length are inversely proportional to the monochromaticity:

$$\tau_c = \frac{1}{\Delta\nu} \qquad (1-17)$$

$$\tau_c = \frac{\mathrm{c}}{\Delta\nu} \qquad (1-18)$$

where $\Delta\nu$ is the laser bandwidth frequency and c is the speed of light in free space. The bandwidth of a laser beam is smaller, and its temporal coherence is greater (Svelto, 2009).

1.2.3 Directionality

Due to the use of an optical resonant cavity, a laser beam is highly collimated and spreads much less than the light from a conventional source as it travels a long distance. Mirrors reflect the photons to make them bounce back and forth in the optical resonant cavity before exiting as a collimated laser beam. The photons are built up and aligned parallelly due to these

reflections. The divergence is negligible but still exists. Based on Huygens' principle, a laser beam emitted from an aperture has a finite divergence.

$$\theta_d = \frac{\beta\lambda}{\mathrm{d}} \qquad (1-19)$$

where λ is the wavelength of the beam, d is the beam's diameter, and β is a coefficient that depends on how the beam diameter and divergence are defined and the shape of the amplitude distribution. θ_d represents half the divergence. The lasers used in this work are of the TEM_{00} mode, so the divergence of the Gaussian beam is

$$\theta_d = \frac{1.27\lambda}{\mathrm{d}} \qquad (1-20)$$

where the width of the Gaussian beam where the intensity is 86% ($1-1/e^2$) of the total intensity. The lens can better focus the collimated laser beam with less divergence because parallel light rays passing through any areas of the lens will be focused on a point. However, light rays with random directions that pass through the center of the lens are not distorted by the lens. Thus, the collimated laser beam diameter can be reduced to create a small probe volume by passing the beam through a lens. The divergence $2\theta_d$ can be expressed by the following equation:

$$2\theta_d = \frac{\mathrm{S}}{\mathrm{f}} \qquad (1-21)$$

where S is the diameter of the focal spot and f is the lens's focal length. The focal spot is smaller if the divergence is smaller (Hitz *et al.*, 2012).

1.2.4 Brightness

Unlike ordinary light that spreads randomly in all directions, a laser emits a narrow light beam. Its energy focuses on a small area because the divergence is small. The brightness is defined as the power emitted per unit surface area per unit solid angle (in steradians). The brightness is expressed as follows:

$$B = \frac{P}{A\Omega} \qquad (1-22)$$

where P is the laser power, A is the cross-sectional area of the laser beam, and Ω is the solid divergence angle.

The laser beam's cross-sectional area can be expressed as $\pi D^2/4$, and the solid angle is equal to $\pi\theta^2$. Additionally, according to Equation 1-22, Svelto (2009) concluded that the beam brightness could also be expressed by the following equation:

$$B = \frac{4P}{(\pi D\theta)^2} = \frac{4P}{(\beta\pi\lambda)^2} \qquad (1-23)$$

1.3 Different Types of Lasers Used in Spectroscopy

1.3.1 Gas Lasers

Gas lasers are lasers that use gas as the lasing medium. Gas lasers include ion lasers (e.g., argon ion laser or krypton ion laser), molecular lasers (e.g., nitrogen lasers and carbon-dioxide lasers), excimer lasers, and neutral atom lasers (e.g., helium-neon lasers).

Argon ion lasers are among the most representative ion lasers. Argon has a full valence shell. Therefore, argon atoms are ionized and excited by high electrical or radio frequency (RF) discharge energy. These lasers have a four-level laser system. The ions are excited from the ground state (principal quantum number = 3) to different 4p states and then relaxed to the 4s state. Lasing occurs during this relaxation. After that, fast decay occurs from the argon ion's 4s state to the argon atom's ground state. The main spectral lines are 488 nm and 514.5 nm.

A nitrogen laser produces high-energy (up to 1 milliwatt) and short (5-10 nanoseconds) pulses of radiation at 337.1 nm because the lifetime of the excited state is relatively short. The electrical pulse of the pumping step should be shorter than the lifetime of the excited state to maintain the laser output. Hence, the population inversion decays quickly.

Nitrogen molecules are pumped to an excited state for a carbon-dioxide laser due to collisions with electrons from electrical discharge. This excited state is close to the excited state of carbon dioxide, so resonant energy transfer occurs between them via collision to pump the carbon-dioxide molecules. After population inversion is achieved, the major lasing transitions to lower levels of different vibrational modes occur, and they result in different wavelengths (mainly 9.6 μm and 10.6 μm).

Excimer lasers produce intense pulses of radiation in the ultraviolet region. Noble gases (e.g., argon, krypton, and xenon) are excited and form an excited complex with fluorine. The excited complex is stable only in the excited state; thus, as long as pumping continues, population inversion is achieved to cause stimulated emission (Skoog *et al*., 2014).

In our lab, we usually use a helium-neon (He-Ne) laser in our basic setup because it is the most cost-effective laser that emits a 632.8 nm laser beam. Nile blue dye is selected for alignment purposes because its maximum absorption wavelength is 625 nm when dissolved in methanol. This is very close to the He-Ne laser output wavelength (Figure 1-4). Nile blue can be selectively detected when mixed with other dyes (e.g., Congo red and ethyl orange) that do not absorb much 632.8 nm light. The He-Ne laser's ratio of helium gas to neon gas is 5:1. Helium gas greatly enhances the pumping process because it collects more energy than neon. Figure 1-5 shows the energy level diagram of the He-Ne laser. Helium bears two electrons with opposite spins in the 1s state. This case is denoted by 1s $^1S_0$. One of the electrons is pumped to the higher states of 2s $^3S_1$ and 2s $^1S_0$. Their spins are opposite. The two excited states of helium are very close to the two excited states of neon. Hence, resonant energy transfer occurs between them via collision. One electron from the 2p orbitals of neon is excited to a higher energy (3s, 4s, 5s, 3p, or 4p) state. The two excited states of neon (4s and 5s) are metastable states, and atoms in these states have longer

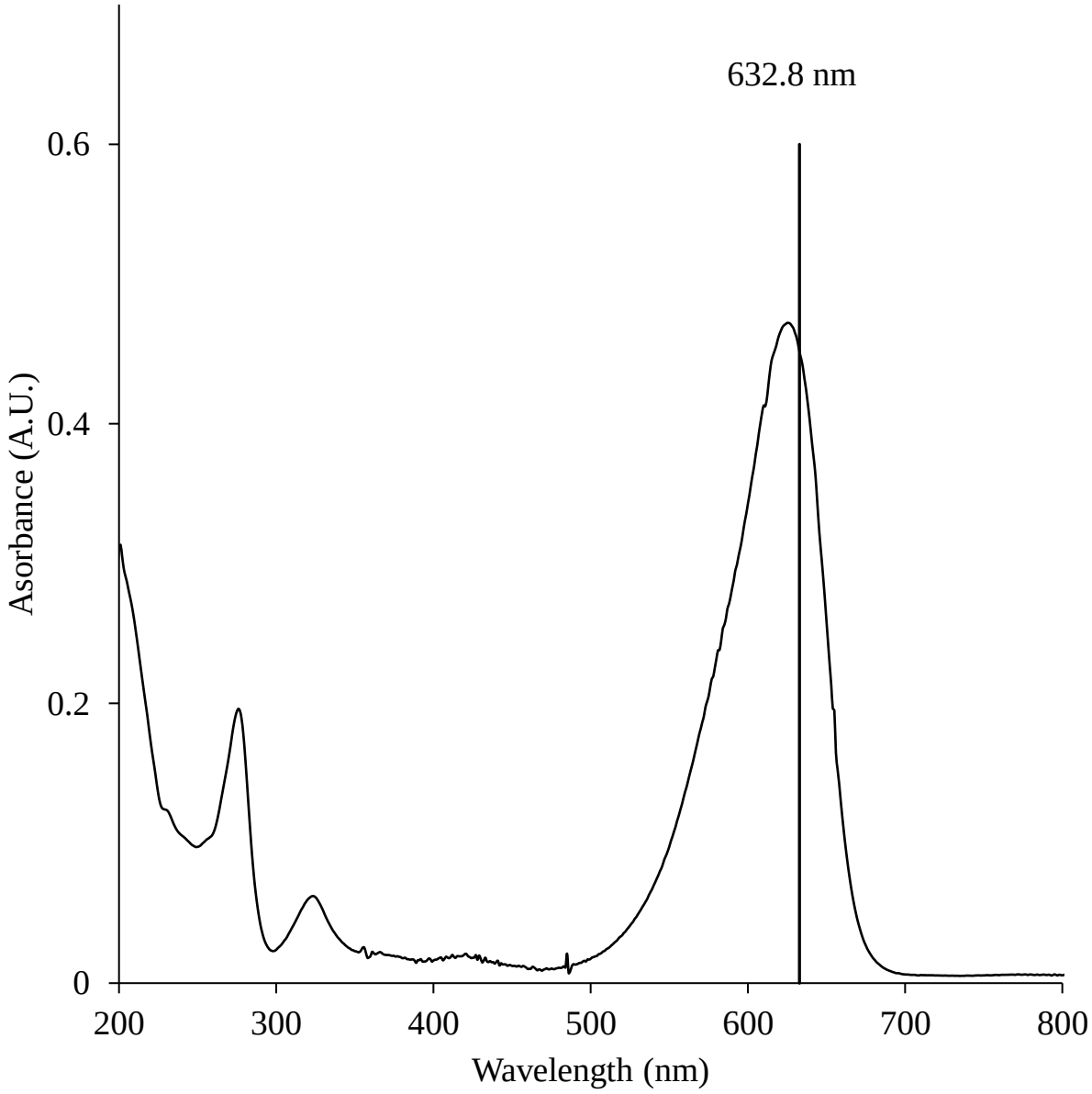

Figure 1-4 Absorbance spectrum of Nile blue dye dissolved in methanol at a concentration of 1 x 10^{-5} M. The maximum wavelength of absorption is 625 nm. A He-Ne laser is suitable for detecting this dye because the wavelength of a He-Ne laser beam is 632.8 nm.

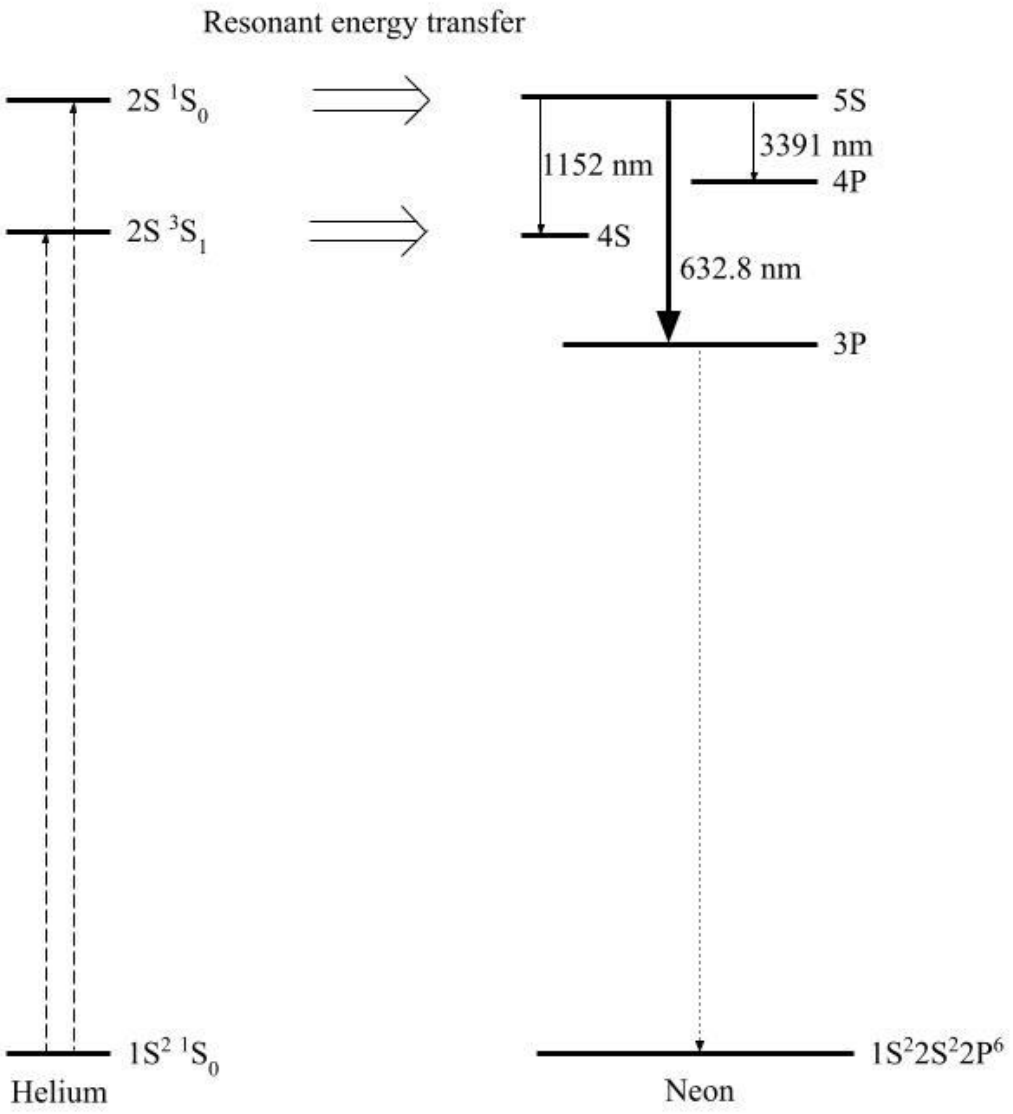

Figure 1-5 Energy level diagram of He-Ne lasers. The solid lines represent stimulated emission.

lifetimes than those in 4p states. Therefore, population inversions on various transitions of neon are achieved. The energy difference of each of these transitions is larger, and the wavelength of the produced radiation is shorter because the frequency of the produced radiation is proportional to the energy difference of the transition (E = hv). The optical resonance determines which transition, and hence wavelength, is amplified (Svelto, 2009).

1.3.2 Semiconductor Diode Lasers

Semiconductor diode lasers are more compact than gas lasers. A semiconductor requires intermediate band-gap energies (thermal or electric potential energies) to promote the electrons from the valence band at lower energy states to the conduction band at higher energy states. In comparison, to achieve this, a conductor requires lower (and insolation requires higher) band-gap energies than a semiconductor.

During the pumping step, the electrons "sink" to the lowest energy states of the conduction band, and the holes "float up" to the top of the valence band. This phenomenon is explained better by introducing two Fermi states, E_c and E_v (Figure 1-6a). When these electrons and holes combine, light is emitted. However, population inversion and optical resonance must be achieved to obtain a laser light beam. Laser radiation is produced by the junction of p-type and n-type semiconductors. E_c in the conduction band of an n-type semiconductor is very close to E_v in the valance band of a p-type semiconductor when no voltage is applied. These two Fermi states are separated until the difference between E_c and E_v is larger than the band-gap energies to achieve population inversion when a high voltage is applied (Figure 1-6b). Optical resonance can be provided by semiconductors or coating reflective layers at the ends of the laser. A laser beam is emitted from an active p-n junction layer sandwiched by a p-type semiconductor layer and an n-type semiconductor layer. These two semiconductor layers connect to a power supply. Common

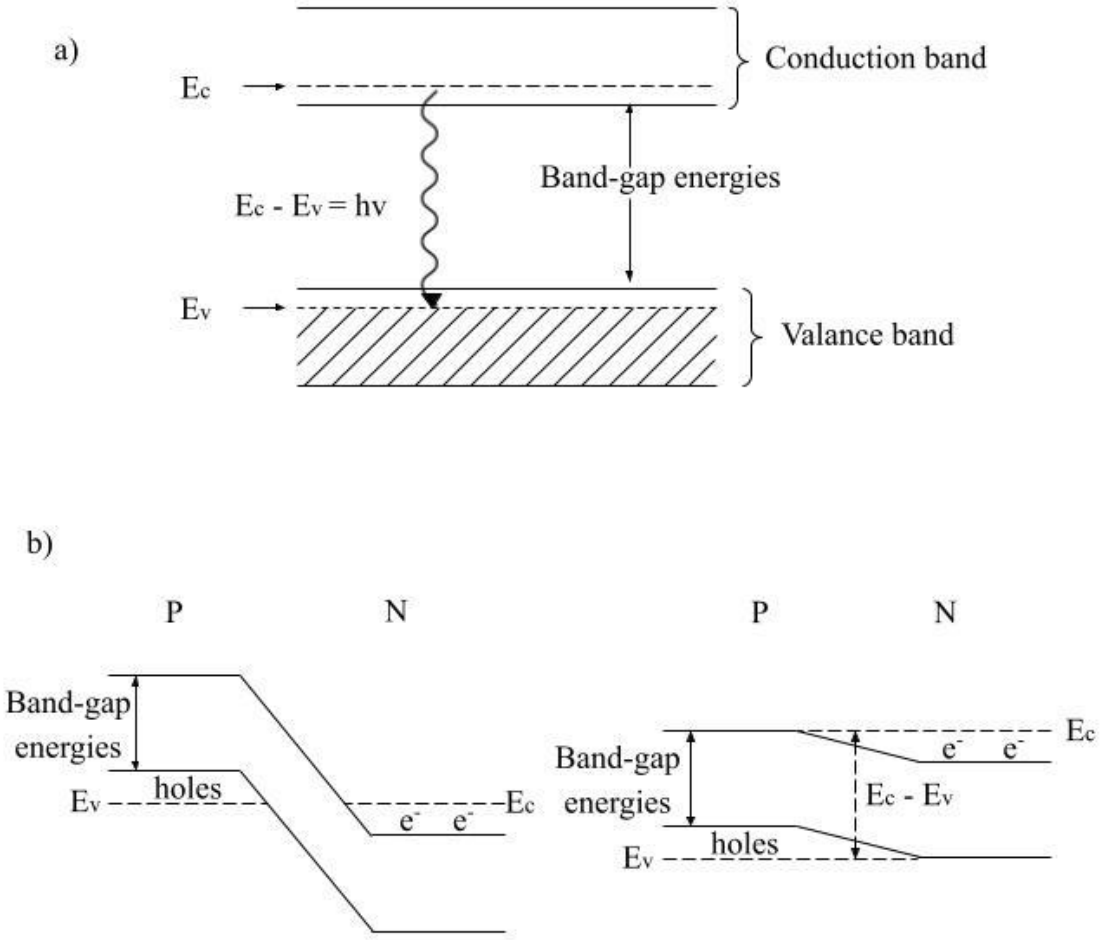

Figure 1-6 a) The semiconductor requires intermediate band-gap energies to promote the electrons from the valence band at lower energy states to the conduction band at higher energy states. During the pumping step, the electrons "sink" to the lowest energy states of the conduction band, and the holes "float up" to the top of the valence band. b) Energy level diagram of semiconductor lasers.

wavelengths of laser beams generated from semiconductor diode lasers fall in the red and infrared regions, but frequency doubling by nonlinear optics creates more possibilities in terms of wavelength (Pearsall, 2017).

1.3.3 Solid-State Lasers

The lasing medium of a solid-state laser consists of a passive host material (crystal or glass) and active dopants (impurities). Oxides or fluorides usually serve as host materials, while transition metal ions or rare-earth ions are typically used as dopants.

Ruby lasers were the earliest solid-state lasers. The host crystal in a ruby laser is Al_2O_3, and its active dopant is chromium(III) ions. Ruby lasers produce laser light at a wavelength of 694.3 nm. The electron configuration of chromium is $[Ar]3d^5 4s^1$. One 4s electron and two 3d electrons from chromium (III) are used to form an ionic bond. Transitions occur within different 3d states caused by the remaining electrons in the 3d orbital. A ruby laser is a three-level laser. Intense pumping energy is required to excite more than 50% of the chromium(III) ions because population inversion occurs between the upper metastable energy state and heavily populated ground states. The wavelengths of the pump bands are 420 nm (blue) and 550 nm (green). The total spin at the ground state and pump band is 3/2, while the total spin of the metastable state is 1/2. Hence, the lifetime of the metastable state is long due to the spin-forbidden transition between the metastable state and the ground state.

The general electron configuration of the rare-earth ion is $[Xe]4f^x 5s^2 5p^6 5d^0 6s^2$. Two 2s electrons and one 4f electron are used to form an ionic bond; hence, triply ionized ions are formed. The remaining electrons in 4f create many different energy states. The fundamental lasing steps, including pumping, spontaneous emission, and stimulated emission, occur within these 4f states under the influence of crystal field interactions.

Nd: YAG lasers are the most representative solid-state lasers that incorporates rare-earth ions. Nd: YAG stands for neodymium (Nd): yttrium aluminum garnet ($Y_3\ Al_5O_{12}$). Neodymium atoms function as dopants, and yttrium aluminum garnet serves as the crystal host. Figure 1-7 shows the energy level diagram of a diode-pumped Nd-YAG solid-state laser. This work uses a 532 nm and 473 nm diode-pumped solid-state laser (DPSSL). The DPSSL uses an 808 nm diode laser as the light source to make pumping occur because a lamp with a broader emission wavelength heats the laser with excess energy. The excited neodymium ions then spontaneously relax to the $^4F_{3/2}$ level. The most vital spectral transition from the $^4F_{3/2}$ to $^4F_{11/2}$ level occurs at 1064 nm. The transition from the $^4F_{3/2}$ level to the $^4I_{9/2}$ upper sublevel occurs at 946 nm. The output lasers from these two transitions can be frequency-doubled by using nonlinear optics to produce 532 nm and 473 nm laser beams. This system operates as a four-level laser system when producing green laser light. When producing blue laser light, it is considered a quasi-three-level laser system (the lower laser level is slightly above the ground state) (Svelto, 2009).

1. 4 Nonlinear Optics

Nonlinear crystals are widely used in the frequency-doubling process mentioned in Section 1.3.3. The electrons in a crystal are trapped in potential wells. For a linear material, the electric field exerts a force to make the electrons oscillate at the same frequency as this electric field. The extent of the polarization (P) is proportional to the electric field strength (E):

$$P = \alpha E \qquad (1-24)$$

where α is a constant; conversely, an intense light source can generate an electric field. If the electric field strength is close to the binding energy of the electrons in a nonlinear material, the force exerted on electrons is no longer proportional to the electron displacement. Thus, the

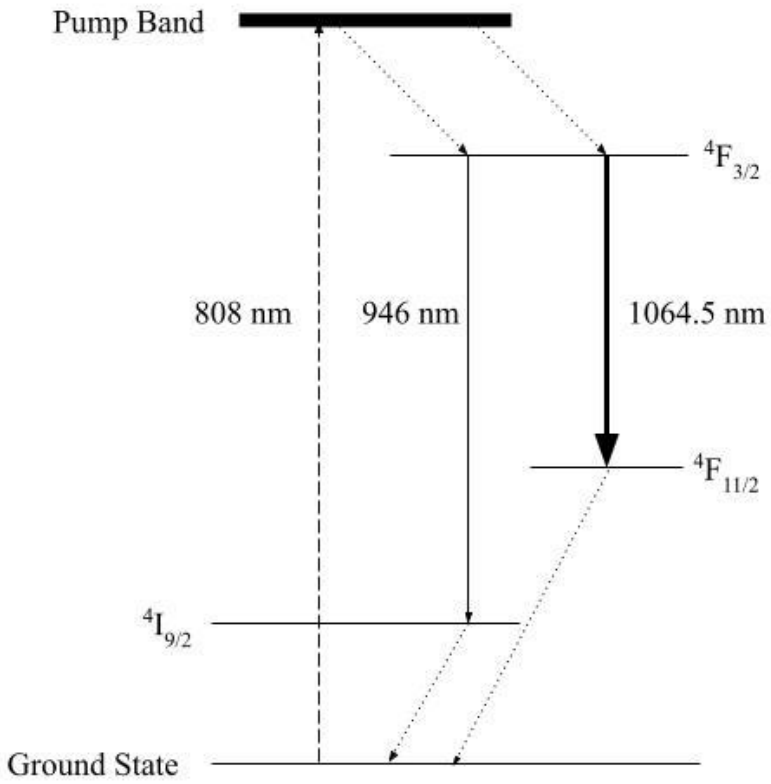

Figure 1-7 Energy level diagram of diode-pumped solid-state lasers. The solid lines represent stimulated emission.

electrons oscillate at another frequency. The relationship between the polarization and electric field can be expressed by the following equation:

$$\mathrm{P} = \alpha\mathrm{E} + \beta\mathrm{E}^2 + \gamma\mathrm{E}^3 + \cdots \qquad (1-25)$$

where β and γ are constants and their magnitudes follow the order α > β > γ. For the frequency doubling process, the second term becomes significant, so the equation can be written as

$$P = \alpha E_m \sin\omega t + \beta {E_m}^2 \sin^2 \omega t = \alpha E_m \sin\omega t + \frac{\beta {E_m}^2}{2}(1 - \cos 2\omega t) \qquad (1-26)$$

where ω is the original radiation frequency, t is time, and E_m is the amplitude of the electric field (Skoog *et al*., 2014).

According to Hitz *et al*. (2012), the conservation of energy is expressed as follows:

$$\frac{\mathrm{hc}}{\lambda_1} + \frac{\mathrm{hc}}{\lambda_2} = \frac{\mathrm{hc}}{\lambda_{\mathrm{new}}} \qquad (1-27)$$

where λ_1 and λ_2 are the two original wavelengths. The new wavelength (λ_{new}) is

$$\lambda_{\mathrm{new}} = \frac{\lambda_1\lambda_2}{\lambda_1+\lambda_2} \qquad (1-28)$$

1.5 Outline of the Dissertation

The following chapters present degenerate four-wave mixing (DFWM) and a sensitive and selective laser-based optical detector coupled to capillary electrophoresis (CE) or a glass surface for detecting cancer-related biomarkers and several other types of protein molecules. Chapter 2 introduces the fundamental concepts of DFWM, along with its significant advantages for ultrasensitive detection. Chapter 2 also demonstrates the optimization of the alignment of optics and other vital factors that enable the ultrasensitive detection of proteins with high signal-to-noise (S/N) ratio. Chapter 3 discusses the theory of CE and illustrates DFWM interfaced with different CE modes to enhance the sensitivity and selectivity of biomarker detection. Chapter 4 presents the

sensitive detection and separation of CA 19-9 using DFWM-CE and various assays for quantifying the pancreatic cancer biomarker carbohydrate antigen 19-9 (CA 19-9). In addition, Chapter 4 also includes the results of optimizing the ratio of label to protein to minimize excess dye, which affects the DFWM signal. Chapter 5 describes the surface detection and scanning of various samples in different forms using the DFWM spectroscopic technique. Notably, the scanning process can be automated with actuators.

1.6 References

Alster, T. S. (2000). *Manual of Cutaneous Laser Techniques*. Lippincott Williams & Wilkins.

Black, S., & Jobling, L. (2014, November). Physical principles of LASER. *Anaesthesia &Amp; Intensive Care Medicine*, *15*(11), 530–532. https://doi.org/10.1016/j.mpaic.2014.08.003

Demtröder, W. (2018). Lasers. *Atoms, Molecules and Photons*, 269–304. https://doi.org/10.1007/978-3-662-55523-1_8

Einstein, A. (1917). Zur Quantentheorie der Strahlung. *Physika Zeitschrift*, *18*, 121–128.

Gianfaldoni, S., Tchernev, G., Wollina, U., Fioranelli, M., Roccia, M. G., Gianfaldoni, R., & Lotti, T. (2017, July 23). An Overview of Laser in Dermatology: The Past, the Present and . . . the Future (?). *Open Access Macedonian Journal of Medical Sciences*, *5*(4), 526–530. https://doi.org/10.3889/oamjms.2017.130

Gordon, J. P., Zeiger, H. J., & Townes, C. H. (1955, August 15). The Maser—New Type of Microwave Amplifier, Frequency Standard, and Spectrometer. *Physical Review*, *99*(4), 1264–1274. https://doi.org/10.1103/physrev.99.1264

Hitz, C. B., Ewing, J. J., & Hecht, J. (2012). *Introduction to Laser Technology*. Wiley.

Meyers, R. A. (2001, October 22). *Encyclopedia of Physical Science and Technology* (3rd ed.). Academic Press.

Mitofsky, A. M. (2018, August 25). *Direct Energy Conversion*. CreateSpace Independent Publishing Platform.

Pearsall, T. P. (2017). Lasers. *Quantum Photonics*, 201–235. https://doi.org/10.1007/978-3-319-55144-9_7

Skoog, D. A., Holler, J. F., & Crouch, S. R. (2014, November 21). *Principles of Instrumental Analysis, 6th Edition* (6th ed.). Cengage Learning.

Svelto, O. (2009). *Principles of Lasers*. Springer Publishing.

CHAPTER 2

DEGENERATE FOUR-WAVE MIXING

2.1 Nonlinear Laser Wave Mixing

Nonlinear optics is a study of the behavior of light in nonlinear optical materials. When light interacts with a medium, it induces the polarization of electrons. The polarization is linearly dependent on the light wave's electric field when the light density level is low. However, intense incident light causes a nonlinear response of the properties of the incident light. For example, the second-harmonic generation (SHG) was demonstrated as a nonlinear optical process when the frequency of a red ruby laser was doubled. According to equations 1-26, the signal intensity of SHG is proportional to the square of the incident light intensity.

The third-order effect was first described by Maker and Terhune (1965). The third-order optical nonlinearity is usually the lowest order of the nonlinear process for all materials because the inversion symmetry in centrosymmetric materials does not yield a second harmonic signal. Four-wave mixing is a third-order nonlinear optical process involving four electromagnetic waves.

Degenerate four-wave mixing (DFWM) refers to the interaction of four light waves with the same frequency through third-order nonlinear polarization: three incident laser beams affecting each other in a material to generate a fourth degenerate beam (Marciu, 1999). It was first used to generate conjugate wavefronts of incident waves (Yariv & Pepper, 1977; Hellwarth, 1977). A "time-reversed" light wave is generated in phase conjugation. In other words, phase conjugation reverses the phase of the incident beam. The incident light wave passes through an inhomogeneous medium to generate a distorted light wave. The phase conjugation process corrects the aberration caused by phase distortion. When the incident light wave interacts with the phase-conjugating

element, the undistorted phase-conjugated light wave propagates in the reverse direction of the incident light wave (Durr & Bouas-Laurent, 2003).

2.2 Highly Sensitive Detection by Nonlinear Laser Wave Mixing

The nonlinear wave-mixing method is used for ultrasensitive detection of gas- and liquid-phase analytes. For gas-phase analytes, isotope-ratio analyses and hyperfine measurements can be achieved by using a backward-scattering laser wave-mixing detector interfaced with an atomizer, such as a discharge or a graphite furnace. Liquid-phase analytes, such as environmental contaminants and biomolecules, can be detected at low concentrations with our laser wave-mixing detector interfaced with different types of separation instruments, such as high-performance liquid chromatography (HPLC), microfluidics and capillary electrophoresis.

2.3 Degenerate Four-Wave Mixing Setup

2.3.1 Backward- and Forward-Scattering Degenerate Four-Wave Mixing

The geometry of DFWM can be backward or forward scattering depending on the optical setup. The interference pattern, generated by two of the three incident beams, is a dynamic grating, from which the third incident beam is scattered to generate the DFWM signal. The geometry of DFWM can be described as shown in Figure 2-1, where k denotes the wave vector. Figure 2-1a shows the k_1 wave and the k_2 wave forming a grating to scatter the k_3 wave; Figure 2-1b shows the grating formed by the k_2 wave and the k_3 wave that scatters the k_1 wave; Figure 2-1c shows the signal beam generated from the scattering of the k_2 wave by the grating formed by the k_1 wave and the k_3 wave. The wave vectors of output signals (k_4) are $k_4 = -k_1+k_2+k_3$ (Figure 2-1a), $k_4 = k_1-k_2+k_3$ (Figure 2-1b), and $k_4 = k_1+k_2-k_3$ (Figure 2-1c). When the wave vector of the output signal is $k_4 = k_1-k_2+k_3$, the phase-matching condition ($\Delta k = 0$) is fulfilled (Shen, 1984). The nonlinear medium in this case is a phase-conjugate reflector (Schmittberger Marlow, 2020). Figure 2-1d shows that

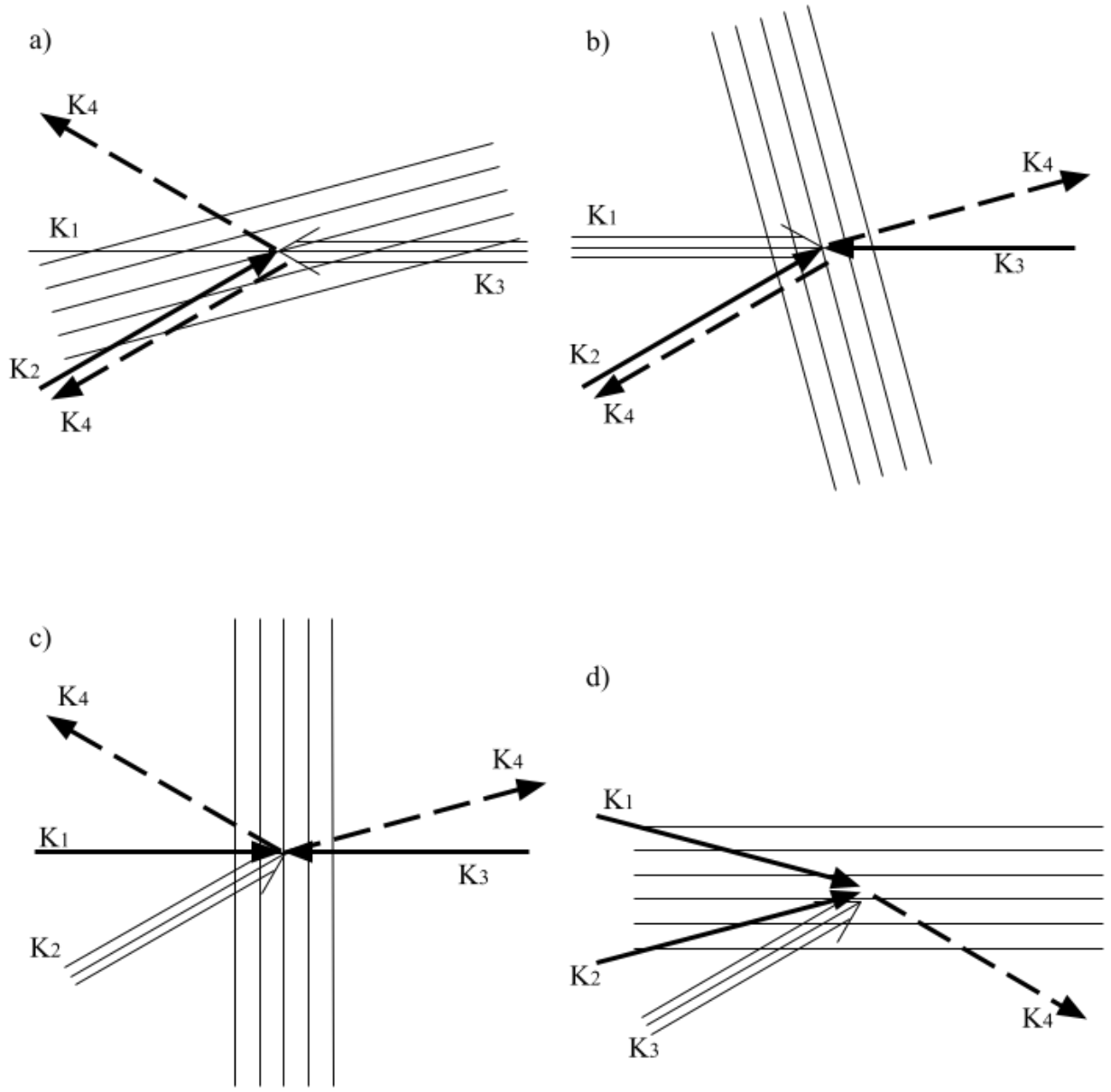

Figure 2-1 Different gratings formed by the backward-scattering and the forward-scattering DFWM setups.

the direction of the output signal is not a phase conjugate (or reverse) of the third incident beam when a forward-scattering DFWM setup is used (Khyzniak *et al*., 1984; Steel, 2004). The wave vector of the output signal is $k_4 = k_1+k_2-k_3$. This configuration is not phased-matched.

2.3.2 Forward-Scattering Degenerate Four-Wave Mixing in Self-Diffraction Geometry

The works in this dissertation employ the forward-scattering DFWM in self-diffraction geometry (Figure 2-2) due to its simple alignment. This geometry only requires two incident beams. The wavelength and the direction of propagation of the probe beam are the same as those of the pump beams. Temporal delay can distinguish the pump and probe beams. In our case, two incident beams (I_1 and I_2) cross at the analyte with a small angle (θ) and form a thermal grating that self-diffracts these two incident beams to yield the signal beams (I_3 and I_4). The intensity ratio of I_1: I_2 is 7:3. Hence, more diffracted photons are generated when I_1 is diffracted to yield I_3. One of the first-order diffracted beams of the stronger incident beam coincides with, the weaker incident beam after the sample cell. The other first-order diffracted beam (I_3) can be angularly resolved from the pump and probe beams; thus, it can be collected easily using a photodetector. When $\omega_1 = \omega_2$, energy conservation requires (Wu & Tong, 1993):

$$\omega_3 = 2\omega_1 - \omega_2 = \omega \qquad (2-1)$$

and

$$\omega_4 = 2\omega_2 - \omega_1 = \omega \qquad (2-2)$$

where ω denotes frequency. In addition, the moment conservation requires that:

$$\vec{k}_3 = 2\vec{k}_1 - \vec{k}_2 \qquad (2-3)$$

and

$$\vec{k}_4 = 2\vec{k}_2 - \vec{k}_1 \qquad (2-4)$$

The small angle (θ) between the pump and probe beam will increase the interaction length inside

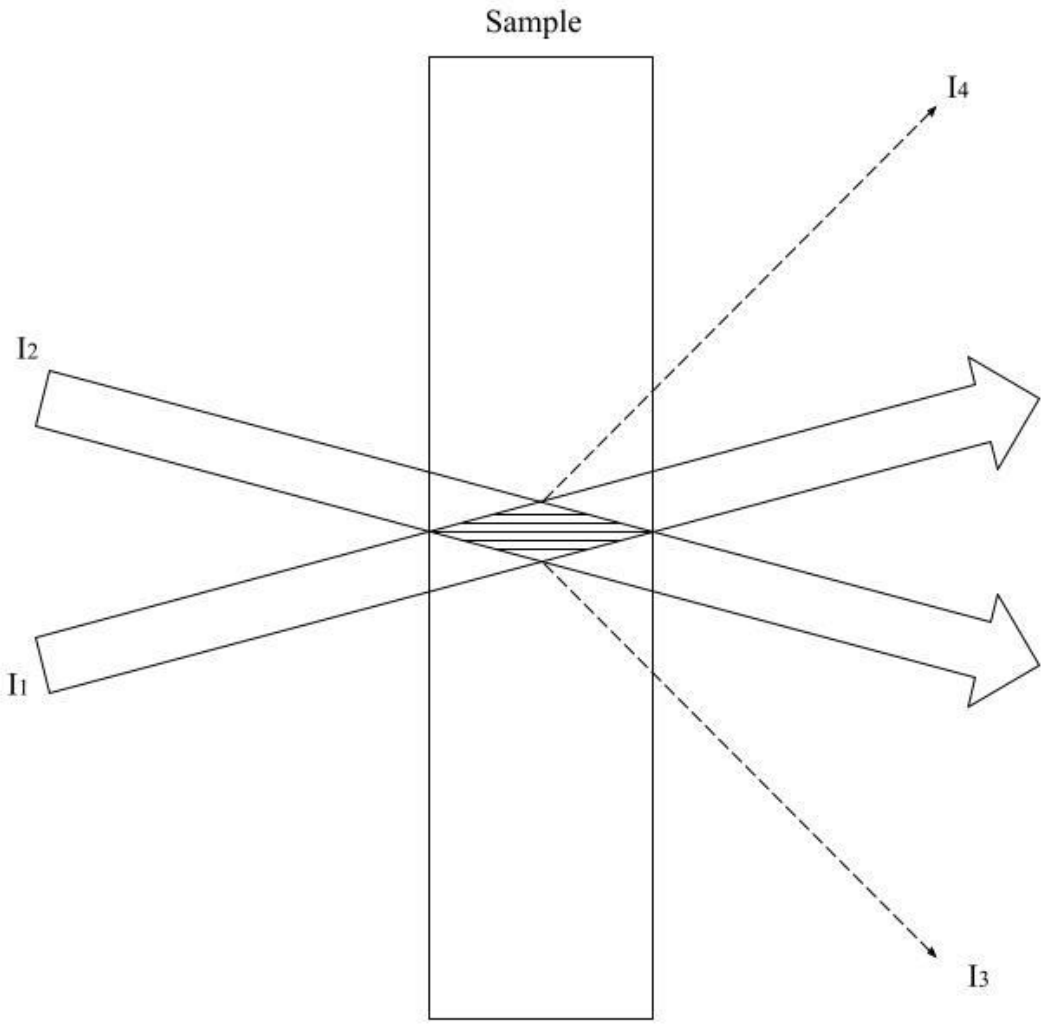

Figure 2-2 Forward-scattering DFWM setup.

the sample and minimize the phase mismatch (Δk), which can be written as follows (Khoo *et al*., 1989; Katzir *et al*., 2015):

$$\Delta\vec{k} = 2\vec{k}_1 - \vec{k}_2 - \vec{k}_3 = 2\vec{k}_2 - \vec{k}_1 - \vec{k}_4 \qquad (2-5)$$

2.4 Laser-Induced Grating

2.4.1 Types of Laser-Induced Gratings

Various types of optical gratings, including population grating, space-charge grating, and thermal grating, can be formed by the interference patterns induced by optical absorption. The analyte is excited to higher electronic states through light absorption to generate a population grating. The excited analyte subsequently relaxes to the lower electronic states to generate a secondary grating. During this relaxation process in a photorefractive material, a space charge grating is generated if charges are formed. A thermal grating is formed when heat is generated after the absorption process. Stress, strain, and density gratings accompany the temperature or thermal grating (Marciu, 1999). Concentration grating is generated by chemical reaction or by the concentration difference of one component in a mixture due to thermal grating (Eichler *et al*., 1986).

2.4.2 Formation of Laser-Induced Gratings

A dynamic grating is produced when two coherent laser beams interfere with each other. Figure 2-3 shows the constructive and destructive interferences created by the interference of two light waves. When the analyte is present, it absorbs light energy along the constructive interference region, and non-radiative thermal relaxation proceeds. Hence, a laser-induced grating is spatially modulated to the interference pattern. The Bragg equation can express the spatial grating period:

$$\Lambda = \frac{\lambda}{2}\sin(\frac{\theta}{2}) \qquad (2-6)$$

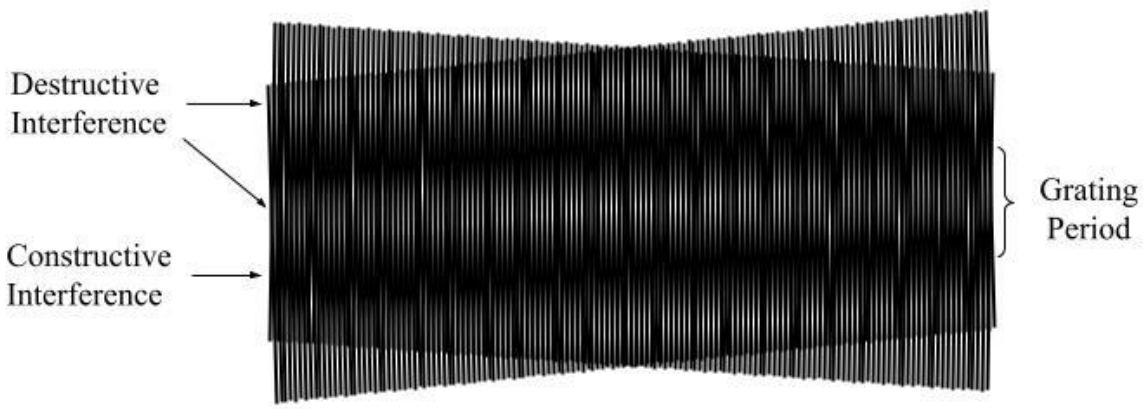

Figure 2-3 Constructive and destructive interferences created by two incident light waves. The lines represent the wave fronts of the laser beams.

where λ is the wavelength. The lifetime of the grating (milliseconds or faster) can be described as follows (Berniolles *et al.*, 1994):

$$\tau_{th} = \frac{\rho C_p \Lambda^2}{4\pi^2 \kappa} \qquad (2-7)$$

where ρ is the density, C_p is the specific heat, and κ is the thermal conductivity. Hence, using a small angle between the pump beam and the probe beams increases the grating period and extends the lifetime, and hence, the stability of the grating.

2.5 Forward-Scattering Wave Mixing in Liquids

Constructive and destructive interference patterns create the periodic temperature distribution in absorbing liquid analytes. The one-dimensional periodic temperature distribution, T(x), in the analyte can be expressed as follows (Kim *et al.*, 1995):

$$\rho C_p \frac{\partial T}{\partial t} - \kappa \frac{\partial^2 T}{\partial x^2} = \alpha I \qquad (2-8)$$

where T is the temperature, t is the time, x is the direction of heat dissipation, α is the absorption coefficient, and I is the incident light intensity modulation, which can be expressed as follows:

$$I = I_0(1 + m\cos\frac{2\pi x}{\Lambda}) \qquad (2-9)$$

where $I_0 = I_1 + I_2$ is the incident light intensity, and m is the pattern contrast that can be described as:

$$m = 2\frac{\sqrt{I_1 I_2}}{I_0} \qquad (2-10)$$

In the steady state ($\partial T/\partial t = 0$), the temperature modulation is (Richard *et al.*, 1986):

$$\Delta T = \frac{amI_0}{\kappa}(\frac{\Lambda}{2\pi})^2 \cos\frac{2\pi x}{\Lambda} \qquad (2-11)$$

The refractive index modulation is (Sanchez *et al.*, 1988):

$$\Delta n = \frac{dn}{dT}\Delta T = \frac{dn}{dT}\frac{amI_0}{\kappa}(\frac{\Lambda}{2\pi})^2\cos\frac{2\pi x}{\Lambda} \qquad (2-12)$$

where dn/dT is the temperature coefficient of the refractive index at constant pressure.

Amplitude and phase gratings contribute to the diffraction efficiency (η). The wave-mixing grating changes both the amplitude and the phase of the probe beam (Neipp *et al*., 2002). Population modulation of the electronic states of analytes and optical saturation forms the amplitude grating. The non-radiative relaxation of the excited analytes results in the formation of the grating. Therefore, heat is released to the surrounding solvent to induce a thermal grating, which corresponds to a phase grating because the temperature change affects the refractive index of the medium. The diffraction efficiency can be expressed as follows (Eichler *et al*., 1986):

$$\eta = \frac{I_3}{I_1} = (\frac{\pi\Delta nd}{\lambda})^2 + (\frac{\mathrm{b}\Delta\alpha}{4})^2 \qquad (2-13)$$

where I_3 is the intensity of the wave-mixing signal, I_1 is the intensity of the probe beam, b is the grating thickness, and $\Delta\alpha$ is the absorption coefficient modulation. The same development with I_2 can be done. In the generation of DFWM signal, thermal grating dominates other types of grating, and hence, refractive index modulation significantly influences the diffraction efficiency (Neipp *et al*., 2002; Hoffman, 1986). Hence, the intensity of the diffracted signal can be simplified as follows:

$$I_3 = (\frac{\pi\Delta nb}{\lambda})^2 I_1 \qquad (2-14)$$

and after substituting equations 2-6, 2-10, and 2-12 in equation 2-14,

$$\mathrm{I_{signal}} \approx (\frac{\mathrm{b}}{8\pi})^2 \mathrm{I_1}^2 \mathrm{I_2} \frac{\lambda^2}{\sin^4\left(\frac{\theta}{2}\right)}\left(\frac{\mathrm{dn}}{\mathrm{dT}}\right)^2 \frac{\alpha^2}{\kappa^2} \qquad (2-15)$$

This equation shows that the DFWM signal intensity exhibits a quadratic dependence on the analyte concentration and the optical path length. Also, the DFWM signal has a cubic

dependence on the laser power due to the third-order nonlinear effect. These features allow our laser wave-mixing method to yield excellent sensitivity levels for the detection of biomolecules.

2.6 References

Berniolles, S., Wu, Z., & Tong, W. G. (1994). Diode laser-based nonlinear degenerate four-wave mixing analytical spectrometry. *Spectrochimica Acta Part B: Atomic Spectroscopy*, *49*(12–14), 1473–1481. https://doi.org/10.1016/0584-8547(94)80123-1

Durr, H., & Bouas-Laurent, H. (2003). *Photochromism: Molecules and Systems* (1st ed.). Elsevier Science.

Eichler, H. J., Günter, P., & Pohl, D. W. (1986). *Laser-Induced Dynamic Gratings (Springer Series in Optical Sciences)* (1st ed.). Springer.

Hellwarth, R. W. (1977). Generation of time-reversed wavefronts by nonlinear refraction*. *Journal of the Optical Society of America*, *67*(1), 1. https://doi.org/10.1364/josa.67.000001

Hoffman, H. (1986). Thermally induced degenerate four-wave mixing. *IEEE Journal of Quantum Electronics*, *22*(4), 552–562. https://doi.org/10.1109/jqe.1986.1072992

Katzir, I., Ron, A., & Firstenberg, O. (2015). Diffraction manipulation by four-wave mixing. *Optics Express*, *23*(5), 6379. https://doi.org/10.1364/oe.23.006379

Khoo, I. C., Normandin, R., Liu, T. H., Michael, R. R., & Lindquist, R. G. (1989). Degenerate multiwave mixing and phase conjugation in silicon. *Physical Review B*, *40*(11), 7759–7766. https://doi.org/10.1103/physrevb.40.7759

Khyzniak, A., Kondilenko, V., Kucherov, Y., Lesnik, S., Odoulov, S., & Soskin, M. (1984). Phase conjugation by degenerate forward four-wave mixing. *Journal of the Optical Society of America A*, *1*(2), 169. https://doi.org/10.1364/josaa.1.000169

Kim, J. H., Chi, D., Kim, S. W., Choi, C. K., & Rhee, C. (1995). The effects of grating period and heating duration time on the measurement of thermal diffusivity of liquids using photothermal grating spectroscopy. *Measurement*, *15*(3), 159–164. https://doi.org/10.1016/0263-2241(94)00043-7

Maker, P. D., & Terhune, R. W. (1965). Study of Optical Effects Due to an Induced Polarization Third Order in the Electric Field Strength. *Physical Review*, *137*(3A), A801–A818. https://doi.org/10.1103/physrev.137.a801

Marciu. (1999). *Optical limiting and degenerate four-wave mixing in novel fullerenes* [Ph.D. dessertation]. Virginia Polytechnic Institute and State University.

Neipp, C., Pascual, I., & Belendez, A. (2002). Experimental evidence of mixed gratings with a phase difference between the phase and amplitude grating in volume holograms. *Optics Express*, *10*(23), 1374. https://doi.org/10.1364/oe.10.001374

Richard, L., Maurin, J., & Huignard, J. (1986). Phase conjugation with gain at CO2 laser line μl = 10.6 μm from thermally induced gratings in nematic liquid crystals. *Optics Communications*, *57*(5), 365–370. https://doi.org/10.1016/0030-4018(86)90276-2

Sanchez, F., Kayoun, P. H., & Huignard, J. P. (1988). Two-wave mixing with gain in liquid crystals at 10.6-μm wavelength. *Journal of Applied Physics*, *64*(1), 26–31. https://doi.org/10.1063/1.341420

Schmittberger Marlow, B. L. (2020). Degenerate four-wave-mixing as a low-power source of squeezed light. *Optics Express*, *28*(25), 38169. https://doi.org/10.1364/oe.411562

Shen, Y. R. (1984). *The Principles of Nonlinear Optics (Wiley Series in Pure & Applied Optics)* (1st ed.). Wiley-Interscience.

Steel, D. G. (2004). *Encyclopedia of Modern Optics, Five-Volume Set*. Elsevier.

Wu, Z., & Tong, W. G. (1993). Forward-scattering degenerate four-wave mixing as a simple sub-attomole-sensitive nonlinear laser analytical spectrometric method. *Analytical Chemistry*, *65*(2), 112–117. https://doi.org/10.1021/ac00050a004

Yariv, A., & Pepper, D. M. (1977). Amplified reflection, phase conjugation, and oscillation in degenerate four-wave mixing. *Optics Letters*, *1*(1), 16. https://doi.org/10.1364/ol.1.000016

CHAPTER 3

DETECTION AND SEPARATION OF PROTEINS USING MULTI-PHOTON NONLINEAR SPECTROSCOPY COUPLED WITH VARIOUS CAPILLARY ELECTROPHORESIS (CE) MODES

3.1 Abstract

Laser wave-mixing spectroscopy offers enhanced selectivity levels for protein detection when coupled with capillary electrophoresis (CE). It provides unique advantages, including portable design, small probe volume (picoliter), high spatial resolution, and absorption detection on micrometer-thin samples, allowing convenient interfacing to capillary electrophoresis. Also, it is an ideal sensor that yields significant changes in signal for small changes in analyte concentration. One can detect the native label-free form of biomarkers using a compact 266 nm UV laser. Fluorophore and chromophore labels can be used if desired or for labeled biomarkers using a visible laser. In this work, the lower detection limit of pancreatic cancer biomarker CA19-9 is 14 U/mL (1.3×10^{-6} U or 11 attomole). Different biomarkers can be separated and detected without interference from other proteins and unbound excess dyes from a dye-conjugated protein solution. CE could also enhance detection sensitivity levels by using sample concentration methods such as field-amplified sample stacking (FASS) and sweeping-micellar electrokinetic chromatography.

3.2 Introduction

3.2.1 Application of DFWM-CE

Multi-photon laser wave-mixing (DFWM) detector interfaced with capillary electrophoresis (CE) is presented as an ultrasensitive and selective detection method for various analytes. Laser wave mixing offers chemical specificity when the excitation laser wavelength is

tuned to the maximum absorption wavelength of the analyte. The specificity can be further enhanced by interfacing wave mixing to a CE or microfluidic separation system for a wide range of analytes that absorb at the same wavelength. If a label or dye is used for the analyte, the excess dye could be separated from the analyte using a CE separation system and other methods.

Capillary electrophoresis has been used to separate various analytes. Stellan Hjerten designed the first CE apparatus (Lewis *et al*., 2013). During the mid-late 1980s, a series of papers about CE was published, and CE instruments became commercially available (Lele *et al*., 2001). To date, CE can be used to separate a variety of analytes, including inorganic and organic ions, carbohydrates, nucleic acids, amino acids, peptides, and proteins, by CE modes, including capillary zone electrophoresis (CZE), capillary isotachophoresis (CITP), capillary isoelectric focusing (CIEF), micellar electrokinetic chromatography (MEKC) and capillary sieving electrophoresis (CSE).

CE offers significant advantages, including speed, high-resolution separation, small sample volumes (nL), and high throughput. Rapid separation can be achieved by increasing the electric field strength (E), which is proportional to the magnitude of the applied voltage (V). Also, the fact that all the analytes move in the same direction due to electroosmotic flow (EOF) leads to short analysis time. On the other hand, high-resolution separation is determined by three factors. The first one is the inexistence of Eddy diffusion and mass transport broadening in CE that only incorporates a single phase. The second one is limited joule heating - a long capillary with small cross-session area results in high solution resistance. The power (P) converted from electrical to thermal energy is low because the solution resistance is high ($P = \frac{V^2}{R}$). The last one is the electroosmotic flow produces a flat profile instead of a laminar (parabolic) profile. Finally, yet

importantly, the CE instrument is cost-effective and operator friendly because automation is achievable.

Laser wave mixing interfaced with CE can detect biomarkers related to pancreatic cancer (CA 19-9), breast cancer (human epidermal growth factor receptor 2), and heart failure (brain natriuretic peptide). On-line sample concentration methods in CE enhance detection sensitivity. Other common proteins, such as bovine serum albumin (BSA) and conalbumin (ovotransferrin), are used to prove the concept of different CE modes. Based on the characteristics of proteins (e.g., isoelectric point, molecular weight, conformations, and surface hydrophobicity), appropriate CE modes should be acquired to separate the proteins efficiently.

Conventional absorption-based detectors could be used for CE systems, however, fluorescence-based detection methods allow the use of smaller probe volumes. Unlike conventional absorption-based detection, laser wave mixing-based absorption detection allows the use of micrometer-thin samples and small probe volumes (nL to pL). Hence, wave mixing offers excellent mass detection limits (attomole to zeptomole range) based on nanoliter small probe volumes (Iwabuchi, 2015).

Chapter 3 presents the principles of CZE, MEKC, and CSE. In addition, biosamples (e.g., CA 19-9) can be focused by using field-amplified sample stacking (FASS) and sweeping-micellar electrokinetic chromatography (sweeping-MEKC) in CE to further enhance detection sensitivity levels. Also, CE is proven to distinguish the excess dye and labeled protein. Adding CE platforms to our novel nonlinear photon method will significantly enhance our methodology, expanding the repertoire of analytes probed in a single run as well as selectivity and detection.

3.2.2 Capillary Zone Electrophoresis

Figure 3-1 shows a typical custom-built CE system and the mechanism of capillary zone electrophoresis (CZE). It is the most straightforward CE mode. Both two ends of a running buffer-filled capillary and two platinum electrodes are immersed in two buffer reservoirs - the two platinum electrodes connected to a high-voltage power supply. Hence, the electric circuit is formed.

The electroosmotic flow is generated when a voltage is applied to a conductive running buffer in a capillary with a fixed cation layer on the negatively charged inner capillary surface. At a pH value greater than 4, the inner capillary surface has negative charges due to the ionization of silanol groups (Si-OH). The negatively charged inner surface attracts cations from the bulk solution developing an electric double layer. The closest layer to the inner surface (stern layer) is static. The density of cations decreases exponentially as the distance from the inner surface increases. The potential difference (zeta potential) will be generated across the double layer. The cations in the diffuse layer move toward the cathode under an electric field and cause the electroosmotic flow by dragging solvent molecules along with them. The velocity of EOF/analyte (ν_{EOF}/ν_{ep}) is proportional to the mobility of EOF/analytes (μ_{EOF}/μ_{ep}). The mobility of EOF can be described as the following equation:

$$\mu_{EOF} = \frac{\varepsilon\zeta}{4\pi\eta} \qquad (3-1)$$

where ε is the dielectric constant of the solution, ζ is the zeta potential, and η is the viscosity of the solution. In addition, the electrophoretic mobility levels of different analytes depend on their charge/size ratios, yielding different migration times as they travel along the capillary (i.e., separating the analytes) since the magnitude of electroosmotic flow is much larger than the

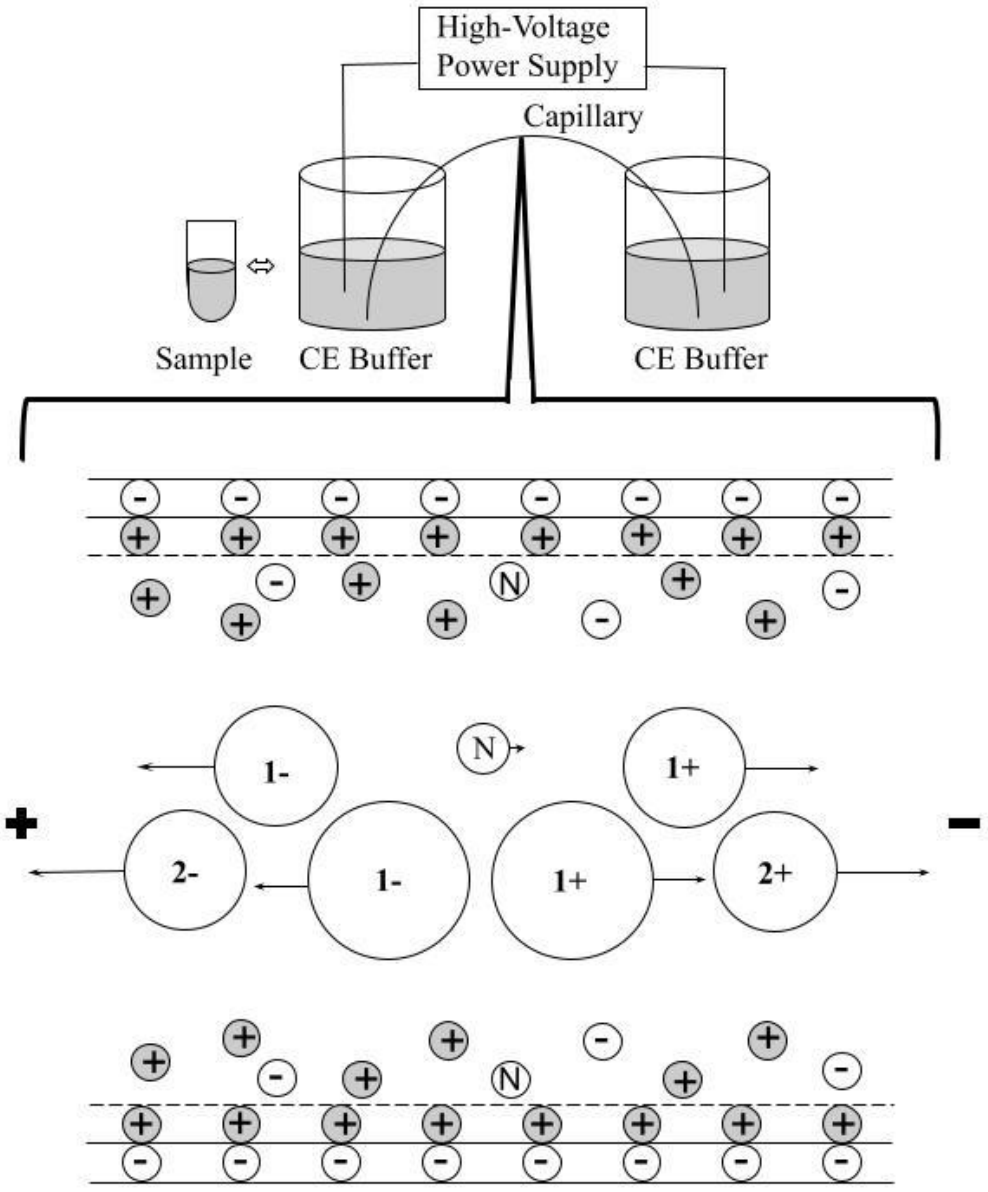

Figure 3-1 Schematic diagram of custom-built CE open system and mechanism of capillary zone electrophoresis.

magnitude of the electrophoretic mobility. The following equation governs the electrophoretic mobility (μ_{ep}):

$$\mu_{ep} = \frac{q}{6\pi\eta r} \qquad (3-2)$$

where q is the effective charge of the analyte species, r is the radius of the analyte species, and η is the viscosity of the solvent. Apparent mobility (μ_a) is the sum of the electrophoretic mobility and the mobility of the electroosmotic flow. Hence, the migration time can be calculated from the ratio between the capillary length to the detector (effective length of the capillary) and apparent velocity (ν_a) as follows:

$$t_m = \frac{l}{\nu_a} = \frac{l}{\mu_a E} = \frac{lL}{\mu_a V} \qquad (3-3)$$

where *l* is the effective length of the capillary, and L is the total capillary length (Marina *et al.*, 2005). CZE is the most basic CE mode, so CZE enlightens the innovation of other CE modes (e.g., MEKC).

3.2.3 Micellar Electrokinetic Chromatography

Micellar electrokinetic chromatography (MEKC) was first introduced by Terabe and his collaborators in 1984 (Terabe *et al.*, 1984). MEKC allows both charged species and neutral species to be separated.

Sodium dodecyl sulfate (SDS) is one of the most common anionic surfactants used to form micelles in an aqueous solution. SDS is dissolved in the desired solution above its critical micelle concentration (CMC) level. Their hydrophobic tails point at the aggregate's center, exposing their hydrophilic heads to the aqueous solution. Hence, the SDS molecules are aggregated to form spherical micelles. These micelles are negatively charged and have significant electrophoretic mobility. Thus, they migrate toward the cathode much more slowly. The micellar phase serves

as a pseudostationary phase. Like the working principle of a liquid chromatography (LC) column, the analytes distribute themselves between the mobile aqueous phases and the pseudostationary phase. The migration time of analytes depends on the interactions (e.g., hydrophobic interaction, electrostatic interaction) between the analytes and the pseudostationary phase. The migration time is longer if that interaction is strong, whereas the migration time is shorter if the analytes have stronger solvation with the mobile aqueous phase (Rizvi *et al*., 2011). Depending on the purpose of the analysis, changing the pseudostationary phase is simple and cost-effective. MEKC plays a crucial role in the invention of on-line sample concentration techniques described below.

3.2.4 On-line Sample Concentration Methods

DFWM sensitivity can be improved by optimizing CE parameters to achieve on-line sample concentration. Various types of on-line sample concentration techniques are available. Field-amplified sample stacking (FASS) and sweeping-MEKC are used in this chapter to obtain the lower detection limits of CA 19-9 (the biomarker of pancreatic cancer). These detection limits are lower than the criterion value predicting pancreatic cancer (cutoff value).

FASS is designed to enhance the sensitivity and resolution of the analysis. The principle of FASS is illustrated in Figure 3-2. According to Burgi & Chien (1991), assuming the components of the sample and running buffers are the same, the sample in a low-concentration buffer is injected from the anode into a capillary filled with a high-concentration running buffer. Following the sample injection, the high-concentration running buffer is introduced to sandwich the sample region between two running buffer regions. When voltage is applied, the electric field strength is larger in the sample buffer region than in running buffer regions because resistivities are inversely proportional to the buffer concentrations and hence, proportional to electric field strength. The ions in the high electric field region move faster than those in the low. Accordingly,

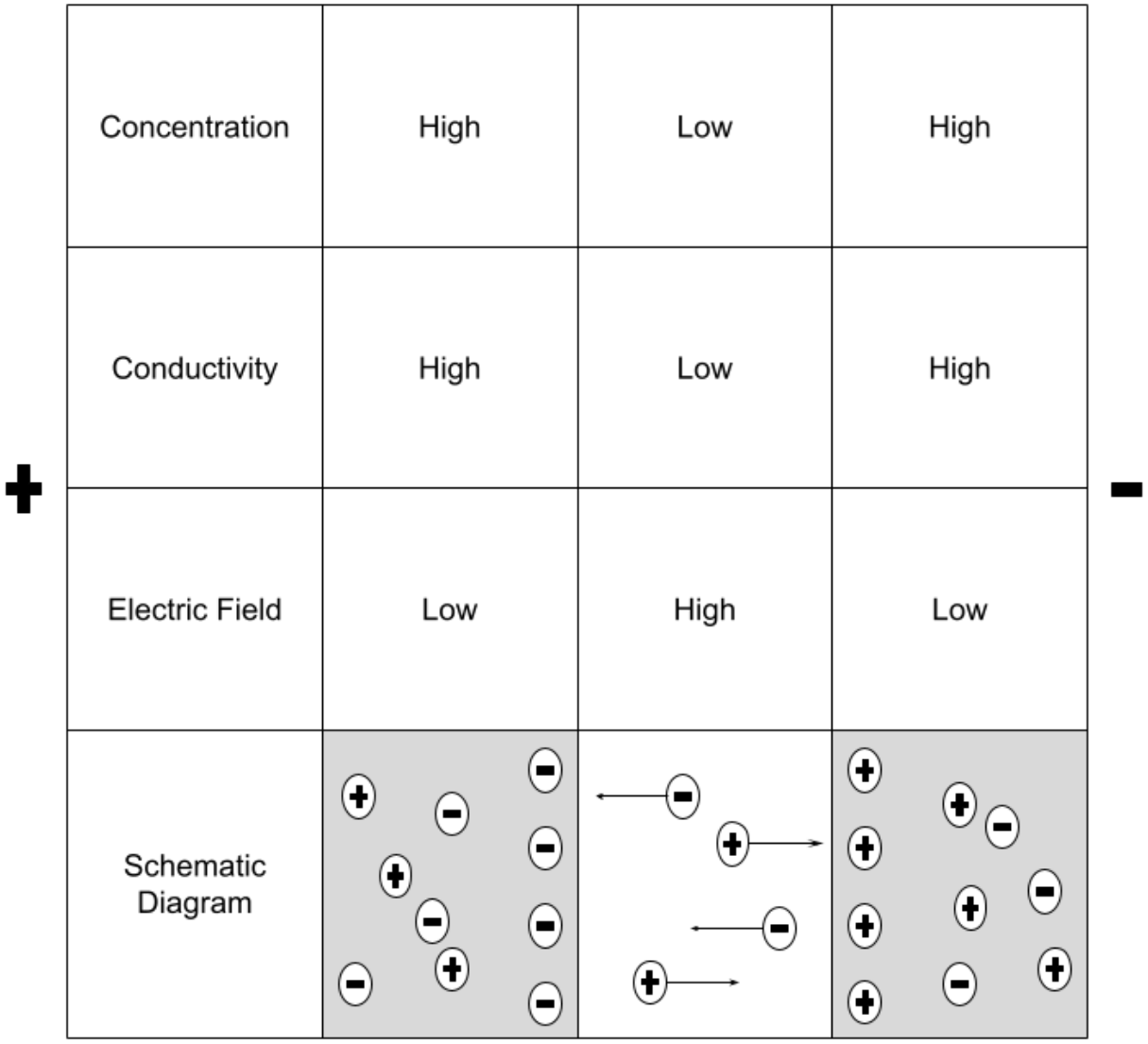

Figure 3-2 Schematic diagram of FASS working principle.

the apparent velocity of the sample ions will dramatically decrease once they cross the concentration boundary. The anionic analytes accumulate in front of the sample region, while the cationic analytes accumulate behind the sample region. FASS can be applied to enhance sensitivity levels as high as 1,000 times.

Sweeping-MEKC is introduced because it can apply to a broader range of analytes (i.e., neutral analytes) compared to FASS. The charged pseudostationary phase (SDS) is employed to give electrophoretic mobilities to a wide range of analytes (i.e., cations, anions, and neutral analytes). Figure 3-3 shows schematic diagrams of one of the sweeping-MEKC modes. The capillary is conditioned with an anionic SDS micellar background electrolyte (BGE). The analytes in the sample zone can quickly be accumulated by the pseudostationary phase that enters the sample zone and sweeps the analytes. The concentration of the sample matrix can be lower than, similar to, or higher than the concentration of BGE. Sweeping-MEKC can provide more than 1000 times improvement in sensitivity levels (Quirino & Terabe, 2000)

3.2.5 Capillary Sieving Electrophoresis

Capillary gel electrophoresis was first converted from sodium dodecyl sulfate-polyacrylamide gel electrophoresis (SDS-PAGE) by Hjerten in 1983 (Zhu *et al*., 2012). Like the working principle of SDS-PAGE, SDS is added to the sample buffer to unfold the proteins and confer similar charge-to-mass ratios. The analyte is injected from the cathode instead of the anode because SDS molecules load negative charges on proteins and guide them to move to the anode. The separation is based on the difference in the molecular weights of protein. However, capillary sieving electrophoresis (GSE) considers protein structure and separates proteins based on size (Dickerson & Dovichi, 2010). The larger protein moves slower, and the smaller protein moves faster.

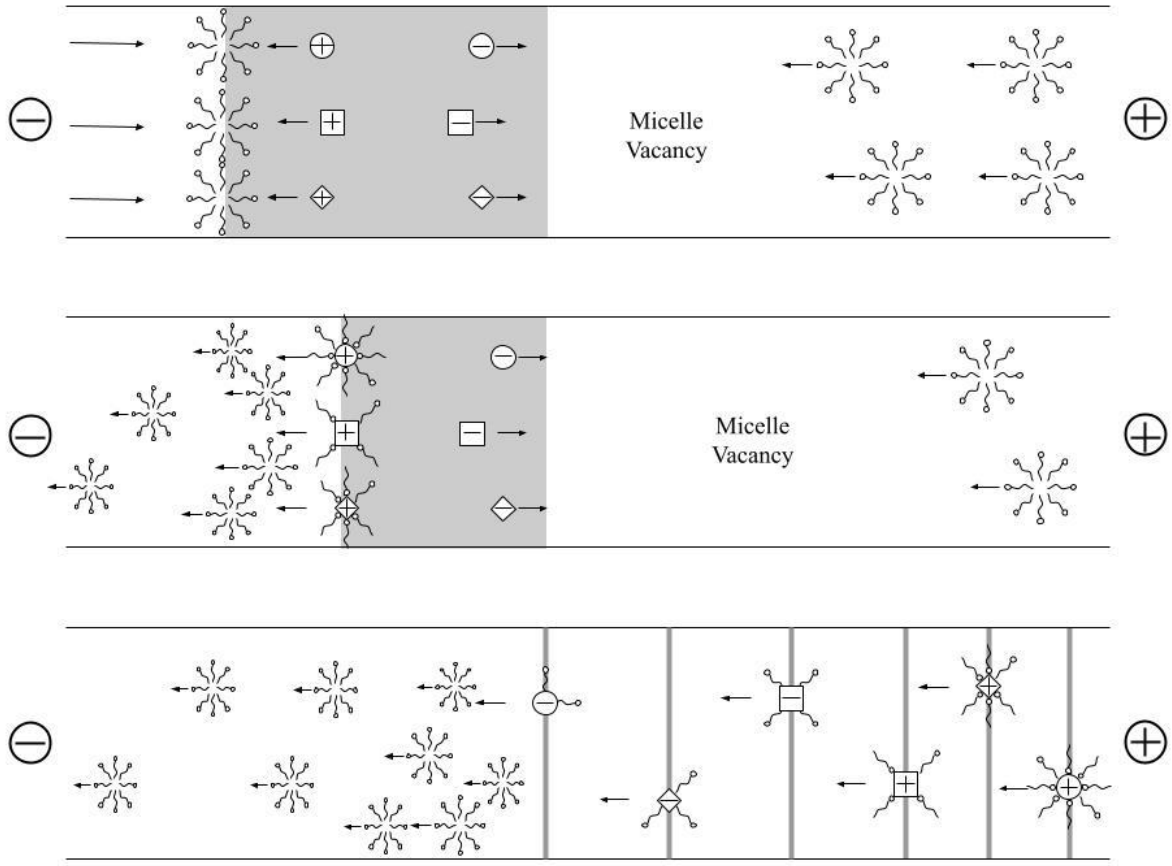

Figure 3-3 Schematic diagram of Sweeping – MEKC. The grey area represents the high-conductivity sample matrix, and the white area represents the low-conductivity BGE.

The SDS gel is an entangled polymer network in the capillary to separate the protein. Linear and crossed-linked polyacrylamide are widely used in CSE. However, the fact that they have strong UV absorption defects the purpose of detecting native proteins because most native proteins absorb UV light (Nakatani *et al.*, 1994). Poly (ethylene glycol) (PEG) and poly (ethylene oxide) (PEO) are used in this chapter because they are UV-transparent. Also, a previous study illustrates that PEG has little effect on the beam profile after the laser beam passes through the detection window on a capillary filled with 3% PEG (Iwabuchi, 2015).

The advantages of CSE over SDS-PAGE are on-line detection, short run time, software-based data collection, and potential for automation that enhances reproducibility. Furthermore, CSE requires a small sample volume. Hence, the mass detection limit is lower.

3. 2. 6 Degenerate Four-Wave Mixing Signal

In this work, we have demonstrated that the lower detection limits of pancreatic cancer biomarker CA 19-9 are lower than the cutoff value for predicting pancreatic cancer (37 U/mL) using our wave-mixing detection methods interfaced with on-line sample concentration in CE. Compared to conventional linear absorption or fluorescence techniques (e.g., UV-vis spectroscopy), DFWM allows more effective detection of minor changes in sample concentration because the wave-mixing signal intensity has a quadratic dependence on concentration. The equation 3-1 describes the signal intensity,

$$I_{signal} \approx (\frac{b}{8\pi})^2 {I_1}^2 I_2 \frac{\lambda^2}{sin^4\left(\frac{\theta}{2}\right)} \left(\frac{dn}{dT}\right)^2 \frac{\alpha^2}{\kappa^2} \qquad (3-1)$$

where b is the optical path length (diameter of the capillary), I_1 and I_2 are the intensity of the laser excitation source, λ is the wavelength of the laser source, θ is the angle between two input beams,

$\frac{dn}{dT}$ is the medium refraction index change with respect to temperature, κ is the thermal conductivity, and α is the molar absorptivity of the analyte ((Berniolles *et al.*, 1994).

Enhancement of sensitivity and selectivity can be achieved when DFWM is interfaced with CE. Our sensitive, early detection tools can conduct fast analysis with a small sample volume. Hence, it will impact not only the diagnosis of pancreatic cancer early and give hope to patients and doctors but also can be modified for other aggressive, treatment-resistant cancers. Appropriate treatments can be facilitated at an earlier stage, and the treatment progress can be monitored efficiently.

3.3 Experimental

3.3.1 DFWM Experimental Setup

A schematic diagram of a typical DFWM optical setup coupled with a CE system is shown in Figure 3-4. This work's laser excitation sources are diode-pumped all-solid-state lasers (MBL-III-473nm-100mW or MGL-III-532nm-100mW, Opto Engine LLC., Midvale, UT) with adjustable power. This laser output is split by a 70:30 (T: R) beam splitter (EBP1, Thorlabs, Newton, NJ) to produce two input beams. The stronger (transmitted) beam serves as both pump and probe beams, and the weaker (reflected) weaker beam acts as a pump beam. These two beams are refocused after traveling equal distances. They are mixed inside by a focusing lens (LA1509-A, Thorlabs, Newton, NJ). The angle between the two input beams are 1.5° (473 nm laser) and 1.2° (532 nm laser). The diameter of the laser beam is 1.5 mm and 1.9 mm. A 75 μm i.d. bare fused-silica capillary (Biotaq, Silver Springs, MD) serves as a sample cell. A polyimide coating remover can remove a detection window (07200-S, MicroSolv Technology, Leland, NC). The calculated probe volume is 95 pL. The stronger signal beam, diffracted by the stronger input beam, is collimated

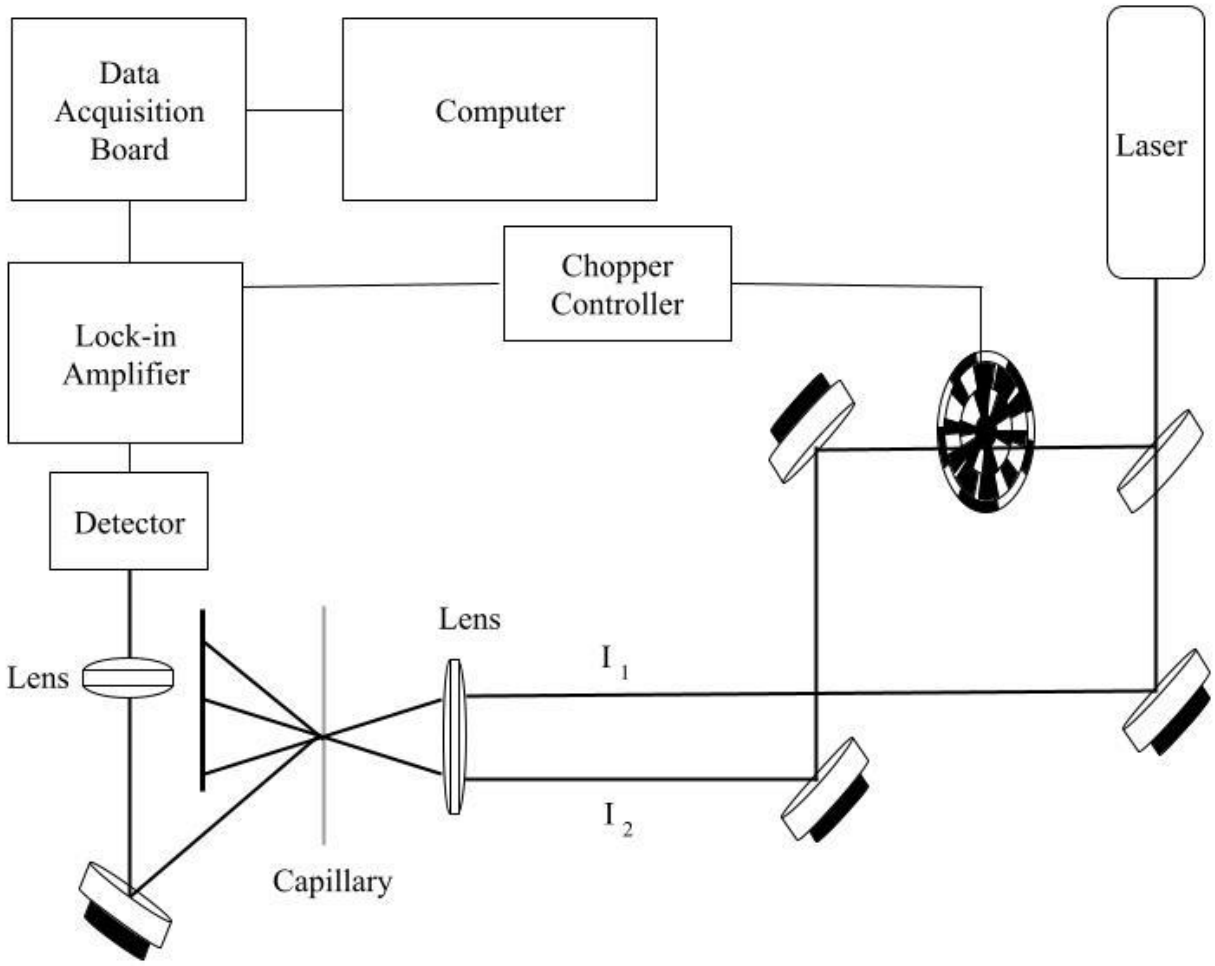

Figure 3-4 DFWM setup interfaced to CE system for protein detection.

and then collected by a photodiode detector (PDA36A, Thorlabs, Newton, NJ). The weaker beam is chopped at 320 Hz by an optical chopper (SR540, Stanford Research Systems, Sunnyvale, CA). The chopper, the photodiode detector, and the data acquisition system (1608FS, Measurement Computing, Norton, MA) are interfaced to a lock-in amplifier (SR810 DSP, Stanford Research Systems, Sunnyvale, CA) where the signal-to-noise ratios are enhanced. The digitalized signal is recorded by customized software (AIDA).

3.3.2 Chemicals and Reagents

All solutions and buffers for this study are prepared using ultrapure water from the PURELAB Flex system (ELGA LabWater North America, Woodridge, IL) and sonicated in a water bath (FS20, Fisher Scientific, Hampton, NH). If used for capillary electrophoresis, they are filtered through a 0.20 µm syringe filter (GVS North America, Sanford, ME). Phosphate-buffered saline (PBS) is obtained from United States Biological (Salem. MA). Sodium hydrogen carbonate, tris(hydroxymethyl)aminomethane (Trizma base), 2-(Cyclohexylamino)ethanesulfonic acid (CHES), sodium hydroxide, hydrochloric acid, sodium tetraborate decahydrate, electrophoresis-grade sodium dodecyl sulfate (SDS), polyethylene glycol – average M_v 10,000 (PEG), bovine serum albumin (BSA) are purchased from MilliporeSigma (Burlington, MA). Regenerated cellulose dialysis tubing (MW_{CO} 12-14 kDa), dye removal columns, N, N- *Dimethylformamide* (DMF), 5-(and 6)-carboxytetramethylrhodamine, succinimidyl ester (NHS-Rhodamine), fluorescein isothiocyanate (FITC), and Pierce unstained protein molecular weight marker (14.4 - 116 kDa) are purchased from Thermo Fisher Scientific (Waltham, MA). Chromeo P503 and Chromeo P540 are obtained from Active Motif (Carlsbad, CA). Ultratrol LN is purchased from Target Discovery (Palo Alto, CA). Brain Natriuretic Peptide (BNP) is purchased from Bachem

Americas, Inc. (Vista, CA). Conalbumin (ovotransferrin) is purchased from BioWORLD (Dublin, OH). Human Epidermal growth factor Receptor 2 (HER-2) is purchased from ACROBiosystems (Newark, DE). CA 19-9 native proteins and recombinant CA 19-9 are purchased from MyBioSource (San Diego, CA). Native CA 19-9 is handled with microliter syringes (Microliter 700, Hamilton Reno, NV) because of the large density of CA 19-9. The protein is purified from the cell free supernatant by classical chromatography methods.

3.3.3 Protein Labeling

1 mg Chromeo P503 is dissolved in 100 μL DMF to label proteins with Chromeo P503. The Chromeo P503 solution is added to the protein solution at 2 mg/mL concentration and mixed well. The reaction is incubated at room temperature for 30 minutes. Dialysis of labeled protein removes excess Chromeo P503 and changes sodium bicarbonate buffer to Tris-CHES buffer for running CE.

In addition, 1 mg of NHS-Rhodamine is dissolved in 100 μL DMF to label the CA 19-9 at a 20:1 (dye: protein) molar ratio, and 7.1 μL of this stock NHS-Rhodamine solution is transferred to 500 μL of 1,600 U/mL native CA 19-9 and dissolved in PBS (pH 7.4). The reaction is incubated at room temperature for 1 hour.

1 mg FITC is dissolved in 100 μL DMF to label the BSA, and 1 mg BSA is dissolved in 1 mL of 50 mM borate buffer (pH = 9). An aliquot of 0.1 μL FITC solution is added to the protein solution dropwise and mixed well.

To label the unstained protein molecular weight marker (14.4 - 116 kDa) that consists of seven proteins (14.4 - 116 kDa) at 0.1 - 0.2 mg/mL, an aliquot of 0.1 μL of 10 mg/mL FITC is used. An aliquot of 150 μL of the stock protein molecular weight marker is dialyzed in 50 mM

borate buffer (pH 9) and diluted 10 times. An aliquot of 0.1 μL FITC is then added to the protein solution and mixed. The FITC-conjugated protein solutions are incubated at room temperature for 1.5 hours. Excess FITC is removed by dialysis using a regenerated cellulose dialysis tubing.

3.3.4 Capillary Electrophoresis

Background electrolytes are prepared by dissolving Tris and CHES powder in ultrapure water to obtain the desired concentration. Sodium hydroxide or hydrochloric acid is added until the desired pH is reached. Depending on the mode of CE, SDS is added to BGE at different concentration levels. The sieving matrix is prepared by dissolving PEG, 10,000 (3%) into Tris-CHES buffer (100 mM).

The custom-built CE system consists of a fused silica capillary and a high-voltage power supply (PS375, Stanford research systems, Inc., Sunnyvale, CA) connected to two platinum wires, which along with the capillary ends, are placed in two plastic reservoirs containing background electrolyte/sieving matrix/samples to complete the circuit. One of the platinum wires serves as the anode and the other serves as the cathode. One could switch the polarity of this high voltage by applying a dynamic coating (e.g., UltraTrol LN).

The new capillary is rinsed with 0.1 M NaOH for 10 minutes, ultrapure water for 10 minutes, the dynamic pre-coating formulation (if applicable) for 2 minutes, and the running buffer for 10 minutes. Between runs, the capillary is flushed with 0.1 M NaOH, ultrapure water, the dynamic pre-coating formulation (if applicable), and the running buffer for 2 minutes. All cleaning and pre-coating processes are completed with a peristaltic pump (RP-1, Rainin Instrument Co., Emeryville, CA) and manifold pump tubing.

3.4 Results and Discussion

3.4.1 Detection Limit Obtained by On-line Sample Concentration Methods in Capillary Electrophoresis

Sample concentration effects in a CE system also enhance the wave-mixing detection sensitivity levels in addition to enhancing chemical specificity levels. The electropherogram in Figure 3-5 is obtained by FASS. It shows electropherograms of Chromeo P503-conjugated CA 19-9 at concentration levels of 56 U/mL and 14 U/mL detected by our laser wave-mixing detector using a 473 nm laser and a label-to-protein ratio of 1:1. The Chromeo P503 shifts the maximum absorption wavelength to 503nm only upon conjugation with lysine groups in CA 19-9. Unbound Chromeo P503 degrades in the conjugation buffer (Activemotif, n.d.). A 473 nm or 532 nm laser can be an excitation source. Chromeo P503-conjugated CA 19-9 is dialyzed into 25 mM Tris-CHES buffer to remove the excess unbound dye and obtain a high-electric field strength upon voltage application. FASS in CE achieves the detection limit of 14 U/mL in capillary electrophoresis. High- concentration (100 mM) Tris-CHES buffer serves as BGE to maintain a low-electric field strength. CA 19-9 in a low conductivity buffer tends to migrate fast with a low conductivity BGE since the sample region has a higher electric field strength (Burgi & Chien, 1991). Accordingly, the apparent mobility of sample ions dramatically decreases once they cross the concentration boundary.

Peak broadening occurs along with FASS. Zeta potential decreases as the buffer concentration increases (Skwarek *et al.*, 2016). Due to the larger zeta potential and electric field strength, the local EOF velocity in the sample buffer region is significantly larger than in running buffer regions. However, the bulk EOF velocity is constant along the capillary because of the continuity principle - the product of the cross-sectional area of the capillary and the bulk EOF

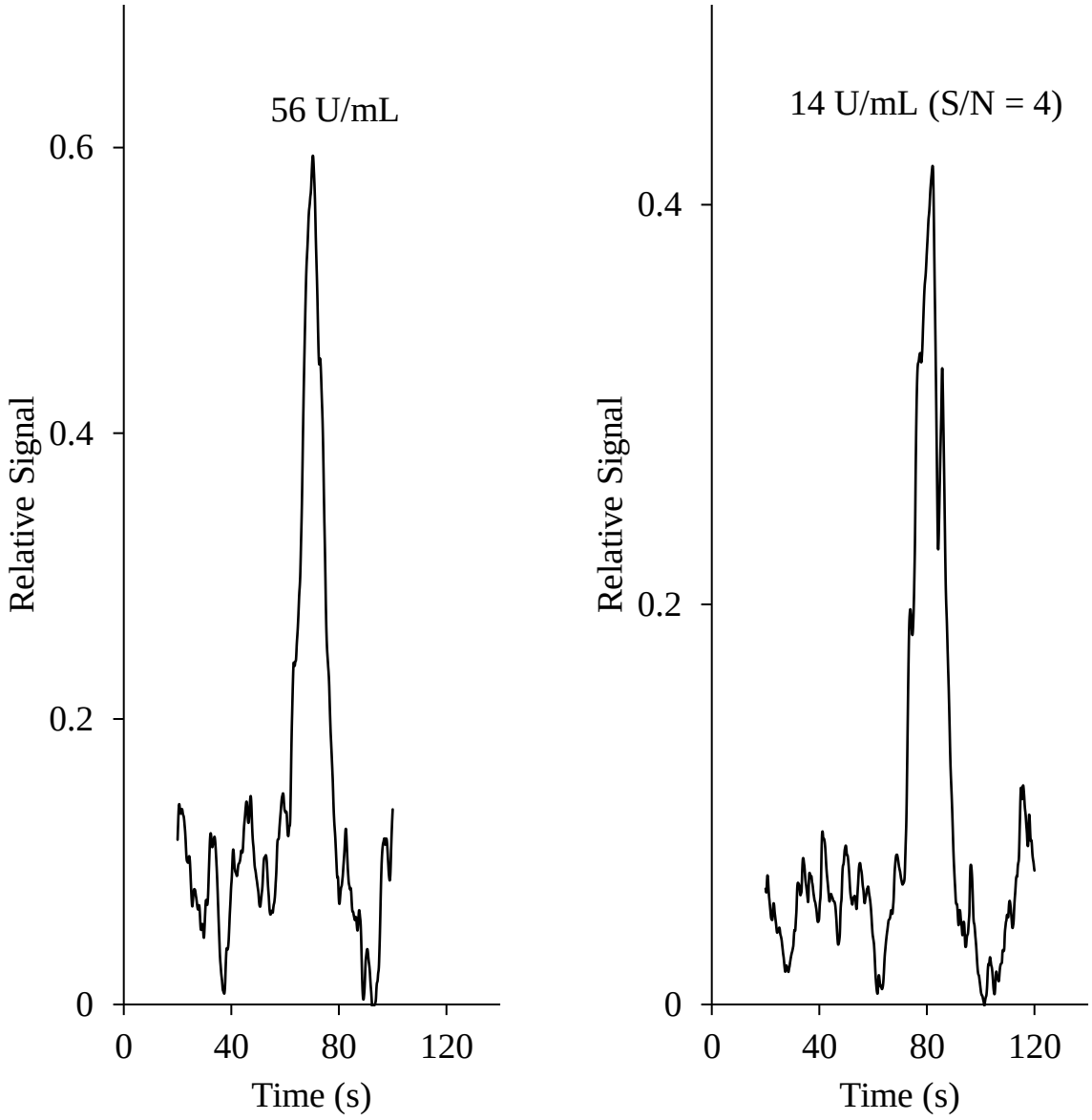

Figure 3-5 Electropherograms of Chromeo P503-conjugated CA 19-9 at a concentration of 56 U/mL (left) and 14 U/mL (right), detected by laser wave mixing detector using a 473 nm laser. Samples are in 25 mM Tris-CHES (pH 9.0) buffer. Capillary: 75 µm i.d., 40 cm (20 cm effective). The capillary is rinsed with NaOH (0.1 M), water, UltraTrol LN, and background electrolyte (100 mM Tris-CHES, pH 9.0) for 2 minutes, respectively. The sample is injected electrokinetically at -10 kV for 15 s. -18 kV is applied for each run.

velocity of the buffer at that cross-section is constant for every position along the capillary. The mismatch of local and bulk EOF velocities causes the laminar flow and hence, the broadening of the stacked zone and poor resolution (Bharadwaj & Santiago, 2005; Burgi & Chien, 1991).

The dynamic coating is used to minimize the adsorption of analytes on the internal surface of the capillary and suppress the EOF. Hence, it offers reproducible migration time and resolution (K M Al Azzam, 2022). UltraTrol LN (Target Discovery, Inc.,2017) is a cost-effective, dynamic coating, and it offers ease of coating and regeneration. Pre-coating can be achieved by flushing the capillary with the commercially available UltraTrol LN for 2 minutes. In addition, it can be removed easily by washing the capillary with sodium hydroxide. Hence, UltraTrol LN is used as a dynamic coating in this work to suppress the EOF.

Figure 3-6 also shows electropherograms of Chromeo P503-conjugated CA 19-9 at concentration levels of 56 U/mL and 14 U/mL detected by our laser wave-mixing detector using a 473 nm laser and a label-to-protein ratio of 1:1. Unlike figure 3-5, figure 3-6 shows sweeping-MEKC in CE achieves a sensitivity level of 14 U/mL. Figure 3-3 shows the working principle of separation. The capillary is filled with a micellar buffer that consists of anionic SDS and low-conductivity electrolytes. Pre-coating the Capillary with UltraTrol LN suppresses EOF, and the sample is injected from the cathode. Upon voltage application, SDS micelles from the cathodic side enter and stack at the sample zone due to the sudden decrease in mobility. The stacked SDS micelles pick up the analyte until the entire sample zone is completely swept (Lin & Kaneta, 2004). The complexes of analyte and stacked micelles accumulate and form a completed swept zone. Afterward, the destacking of SDS micelles occurs and causes swept zone broadening because the SDS micelles continually travel to the anodic side. Hence, they enter the BGE region again with micelle vacancy; thus, the micellar concentration decreases (Aranas *et al.*, 2009; Joselito *et al.*).

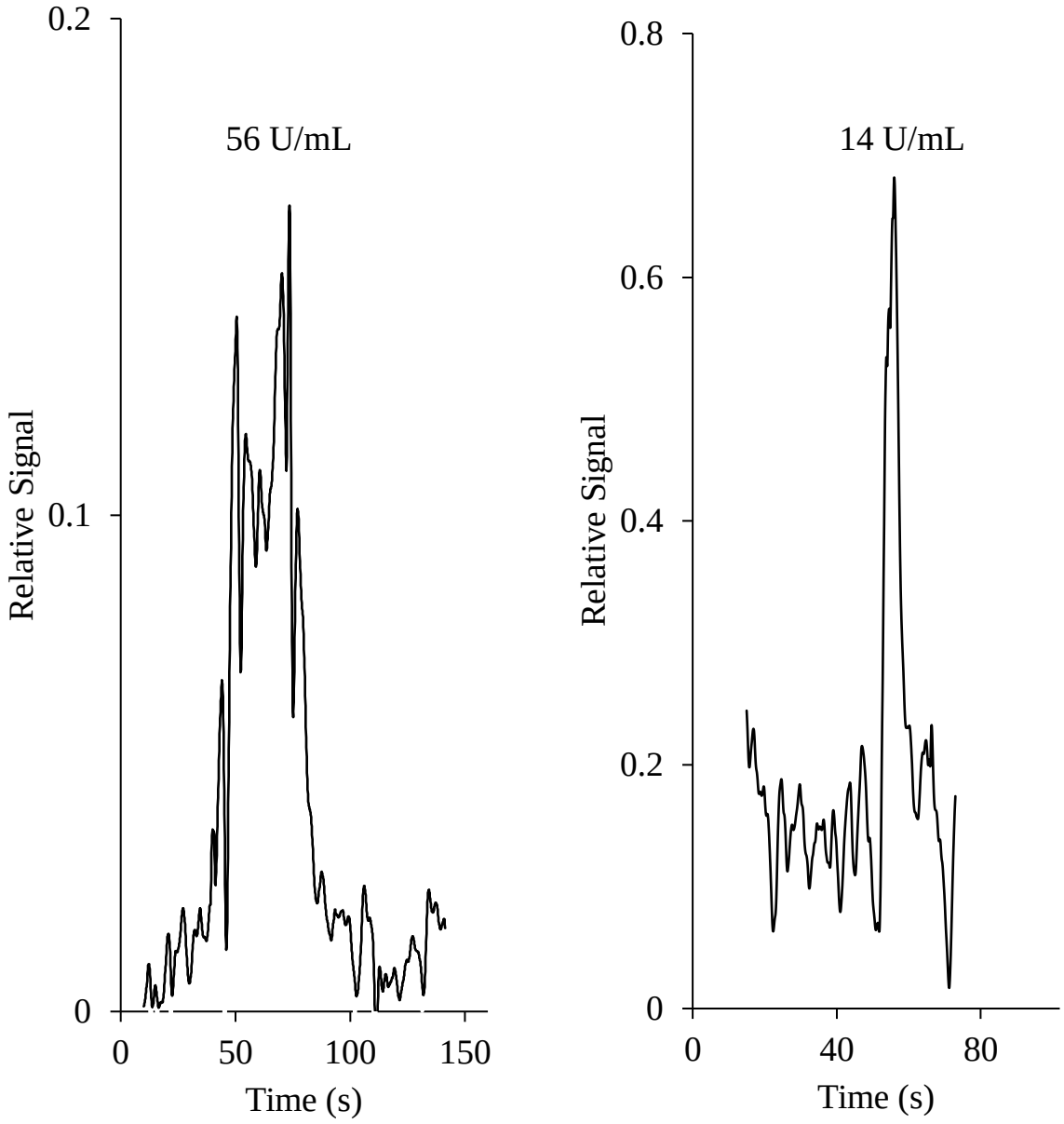

Figure 3-6 Electropherograms of Chromeo P503-conjugated CA 19-9 at a concentration of 56 U/mL (left) and 14 U/mL (right), detected by laser wave mixing detector using a 473 nm laser. Samples are in 50 mM Tris-CHES (pH 9.0) buffer. Capillary: 75 µm i.d., 30 cm (15 cm effective). The capillary is rinsed with NaOH (0.1 M), water, UltraTrol LN, and background electrolyte (12.5 mM Tris-CHES, pH 9.0) with 80 mM SDS buffer for 2 minutes, respectively. The sample is injected electrokinetically at -10 kV for 15 s. -18 kV is applied for each run.

2000).

DFWM interfaced with CE on-line sample concentration modes (i.e., FASS and sweeping-MEKC) in CE can achieve a sensitivity level of 14 U/mL, which is significantly below the cutoff value (37 U/mL) of CA 19-9 for the diagnosis of pancreatic cancer. The mass detection limit is impressive (1.3×10^{-6} U or 11 attomole) due to the small probe volume (95 pL) of the 473nm laser.

3.4.2 Separation of Proteins in Capillary Electrophoresis

The main reason CE is chosen to work with our sensitive DFWM detector is to enhance specificity. CE can identify the excess dyes and distinguish different proteins. Excess dye can be easily removed by dialysis (6 hours) or dye removal columns for reduction of interference, as shown in this work. Interfacing the wave-mixing detector to a CE separation system allows one to enhance both detection sensitivity and chemical selectivity levels and also separate and identify the excess labels from a labeled CA 19-9 sample.

The simplest CE mode (CZE) can effectively separate excess NHS-Rhodamine from NHS-Rhodamine-labeled CA 19-9. Figure 3-7 shows the electropherograms of NHS-Rhodamine and NHS-Rhodamine conjugated-CA 19-9 using a 20:1 molar ratio. Excess NHS-Rhodamine can be easily separated and identified. The absorption maximum of NHS-Rhodamine-conjugated CA 19-9 is at 520 nm, and it does not shift upon conjugation with CA 19-9. Hence, a 532 nm laser is selected as the laser excitation source for our wave-mixing setup. Commercially available NHS-Rhodamine consists of two different molecules (5-carboxy tetramethylrhodamine, succinimidyl ester, and 6-carboxy tetramethylrhodamine, succinimidyl ester), and hence, one can observe two peaks in the electropherogram of free NHS-Rhodamine.

Since the same amount of NHS-Rhodamine is dissolved in both the PBS buffer and the CA

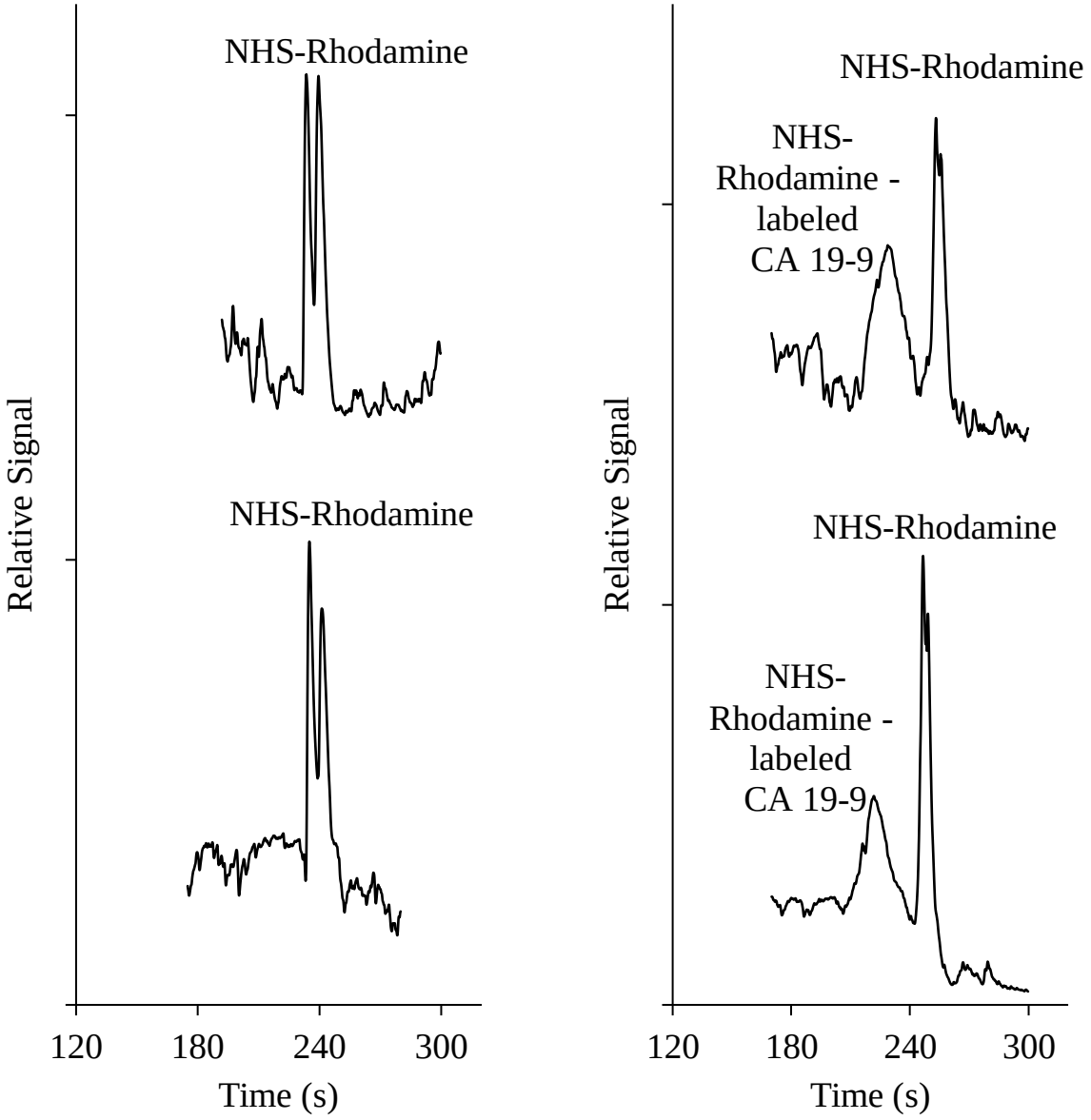

Figure 3-7 Electropherograms of 13.3 μM NHS-Rhodamine (left) and 80 U/mL NHS-Rhodamine conjugated-CA 19-9 using 20:1 molar ratio (right), detected by laser wave mixing using a 532 nm laser and a sample buffer with 25 mM Tris-CHES, pH 9.0, 0.1% SDS. The capillary (75 μm i.d., 45 cm total, 25 cm effective) is rinsed with NaOH (0.1 M), water, UltraTrol LN, and background electrolyte (100 mM Tris-CHES, pH 9.0) for 2 minutes. The sample is injected electrokinetically at -18 kV for 20 s, and -16 kV is applied for each run.

19-9 solution, the amount of free NHS-Rhodamine in PBS buffer is less than that in the CA 19-9 solution because a portion of free NHS-Rhodamine is conjugated with CA 19-9 to form a complex of NHS-Rhodamine-labeled CA 19-9. Therefore, free NHS-Rhodamine is injected more from PBS solution if CE conditions are the same. Hence, the observation of some peak broadening as in electropherograms of free NHS-Rhodamine.

CE can distinguish different proteins. Figure 3-8 shows electrograms of BSA and the separation of conalbumin and BSA. The concentration of sample matrix can be lower than the concentration of BGE. Hence, as opposed to the condition of buffer concentrations of figure 3-6, BGE is a high conductivity solution, whereas the sample is prepared in a lower conductivity solution. Upon voltage application, SDS micelles from the cathodic side sweep the sample region and interact with analytes. The complexes of the sample and micelles then accumulate at the anodic end of the sample region due to the sudden decrease in their velocity (Quirino & Terabe, 1999).

The sizes of proteins and the affinity of analytes towards the micelles (i.e., electrostatic interaction, hydrophobic interaction) determine the order of protein peaks in the electropherogram. Since BSA has a smaller molecular weight and more hydrophobic amino acids than conalbumin, the peak of BSA appears before the peak of conalbumin. BSA's signal is stronger than conalbumin's signal because BSA has many more binding sites (lysine) than conalbumin.

Figure 3-9 shows electropherograms of BNP and the separation of BSA and BNP. The CE condition is the same as the separation of conalbumin and BSA. BNP is an important biomarker for heart failure. It is a hormone to suppress the progression of heart failure and was first identified in the porcine brain (Suprapto & Tong, 2023). It is a small cationic peptide that can strongly interact with negatively charged SDS micelles from the BGE region. In addition, although BSA

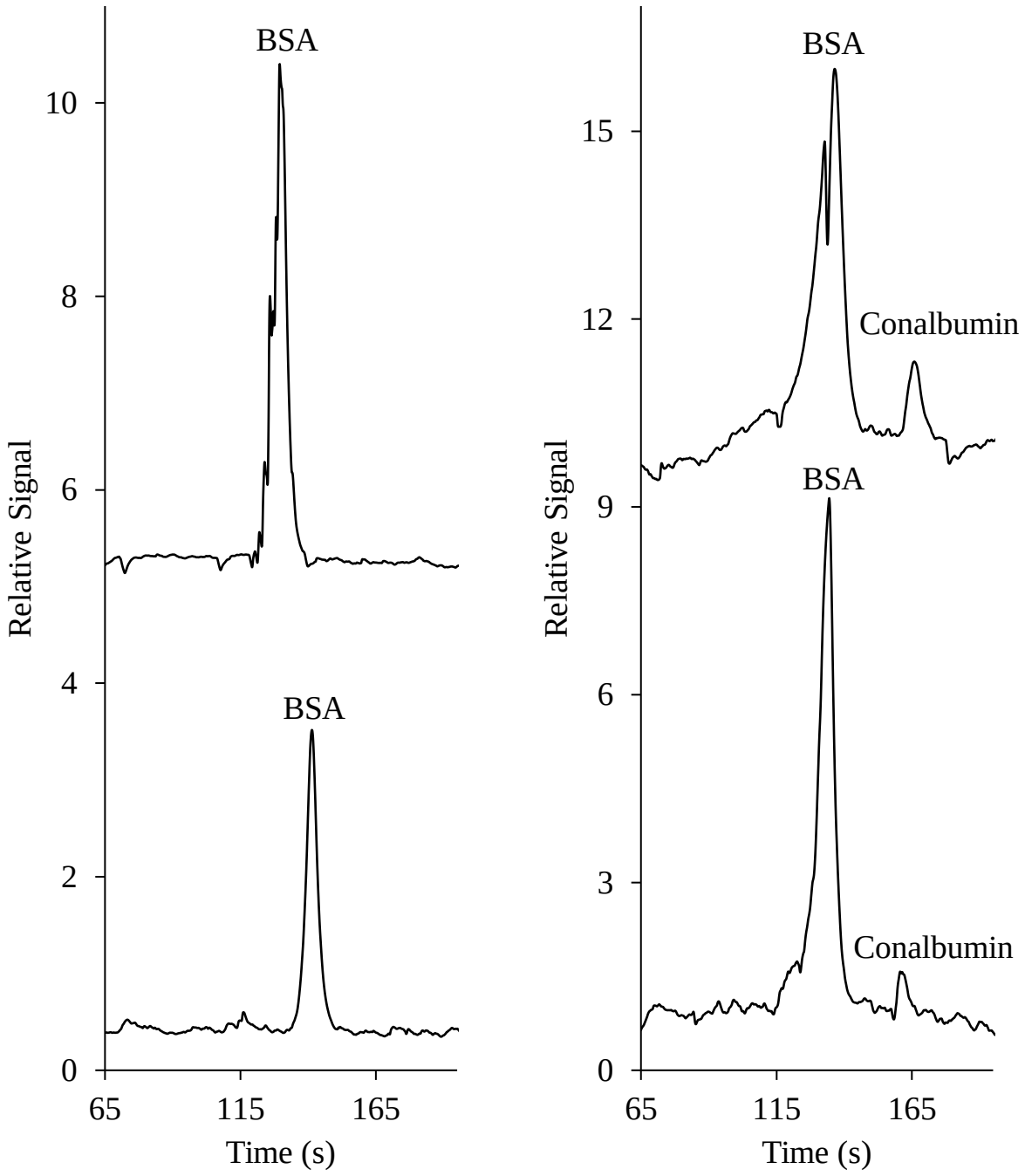

Figure 3-8 Electropherograms of Chromeo P503-conjugated BSA at a concentration of 6 μM (bottom two) and separation of Chromeo P503-conjugated BSA and Chromeo P503-conjugated conalbumin at a concentration of 3 μM (top two), detected by laser wave mixing detector using a 473 nm laser. Samples are in sample buffer (25 mM Tris-CHES, pH 9.0). Capillary: 75 μm i.d., 40 cm (20 cm effective). The capillary is rinsed with NaOH (0.1 M), water, UltraTrol LN, and BGE (50 mM Tris-CHES, pH 9.0, 40 mM SDS) for 2 minutes, respectively. The sample is injected electrokinetically at -10 kV for 15 s. 18 kV is applied for each run.

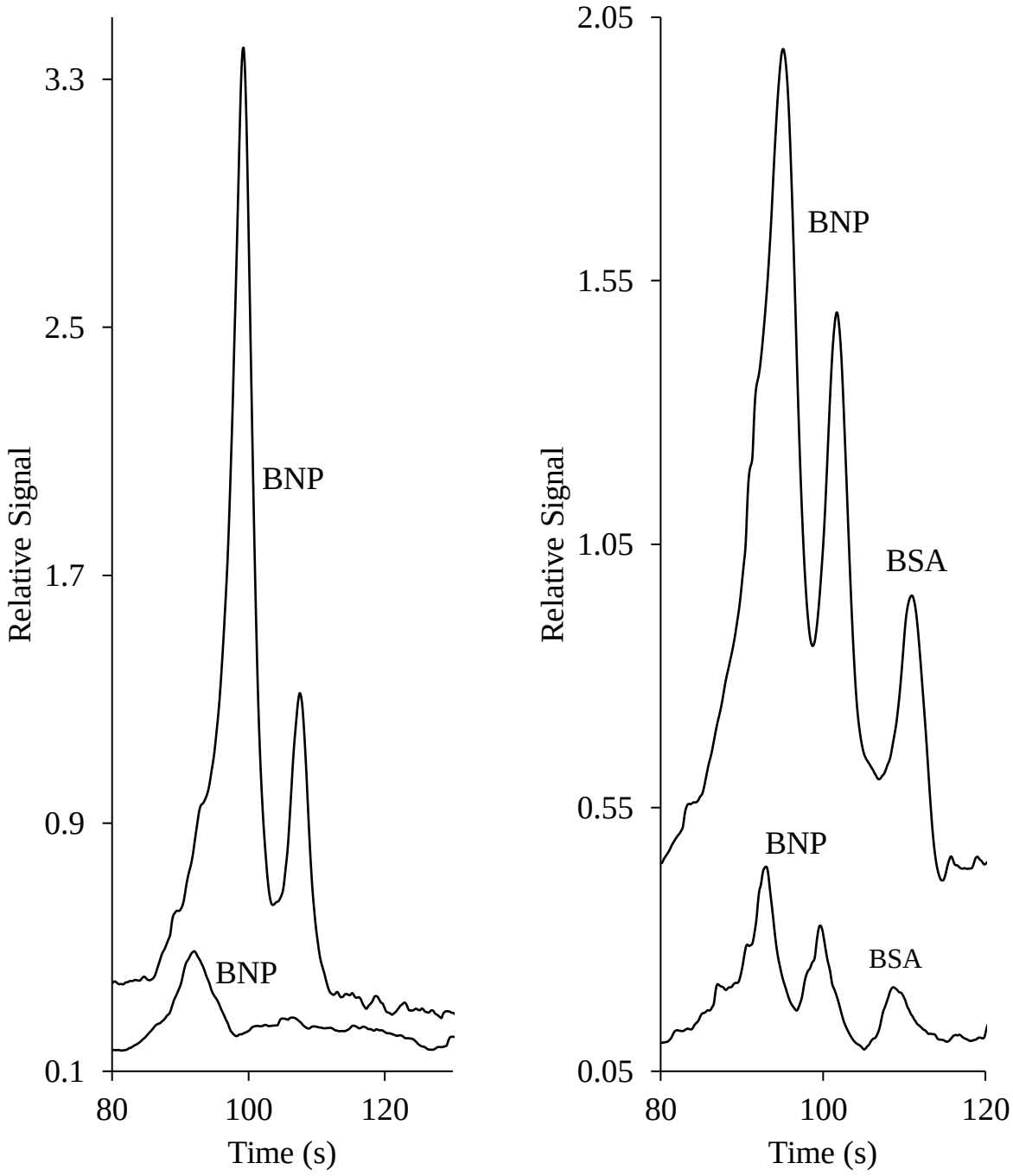

Figure 3-9 Electropherograms of Chromeo P503-conjugated BNP at a concentration of 40 μM (left) and separation of Chromeo P503-conjugated BNP at 20 μM and Chromeo P503-conjugated BSA at a concentration of 5 μM (right), detected by laser wave mixing detector using a 473 nm laser. Samples are in sample buffer (25 mM Tris-CHES, pH 9.0). Capillary: 75 μm i.d., 40 cm (20 cm effective). The capillary is rinsed with NaOH (0.1 M), water, UltraTrol LN, and background electrolyte (50 mM Tris-CHES, pH 9.0, 40 mM SDS) for 2 minutes, respectively. The sample is injected electrokinetically at -10 kV for 15 s. -18 kV is applied for each run.

is also negatively charged under basic solution, the molecular weight of BSA (66.4 kDa) is significantly larger than the molecular weight of BNP (4.9 kDa). Therefore, BNP migrates toward the anode faster than BSA. In research from Gao *et al*., SDS may interact with BNP differently and cause multiple peaks due to the different number of SDS molecules incorporated (2019).

The performance of Sweeping-MEKC depends on many factors, such as the concentration of micelles, the concentration of BGE and sample buffer, and separation voltage and sample injection length. Sample injection length is related to the interaction between analytes and micelles. If the interaction is not strong enough, sample injection length should be limited due to micelles' lack of sweeping capacity. Injection length can be modified by injection time (Zheng *et al*., 2021). The sample solution (HER-2) is injected at 10 kV (reserved polarity) for 5, 10, 15, and 20 s into the capillary to optimize the condition of sample injection time. HER-2 is overexpressed in about 25% of breast cancers. Patients with less HER2 overexpression are generally in a better situation, and there are FDA-approved methods targeting HER2 (Tai *et al*., 2010). From figure 3-10, we can see the signal intensity of HER-2 increases when the injection time increases from 5s to 15s (Zheng *et al*., 2021). When the injection time is 15s, better sensitivity with a decent resolution is obtained. Hence, 15 s is chosen as the optimal sample injection time. The different number of SDS molecules may interact with HER-2 and cause peak broadening (Gao *et al*., 2019).

Normal polarity can also be used to achieve protein separation. Without pre-coat the Capillary with UltraTrol LN, the direction of EOF is from anode to cathode, and its magnitude is more prominent than electrophoretic mobility. Upon voltage application, the anionic SDS micelles move to the sample region from the BGE region at the cathodic side and interact with the sample. Afterward, the complexes of the sample and micelles accumulate at the interface between the anodic end of the sample zone and the BGE region at the anodic side because the complexes slow

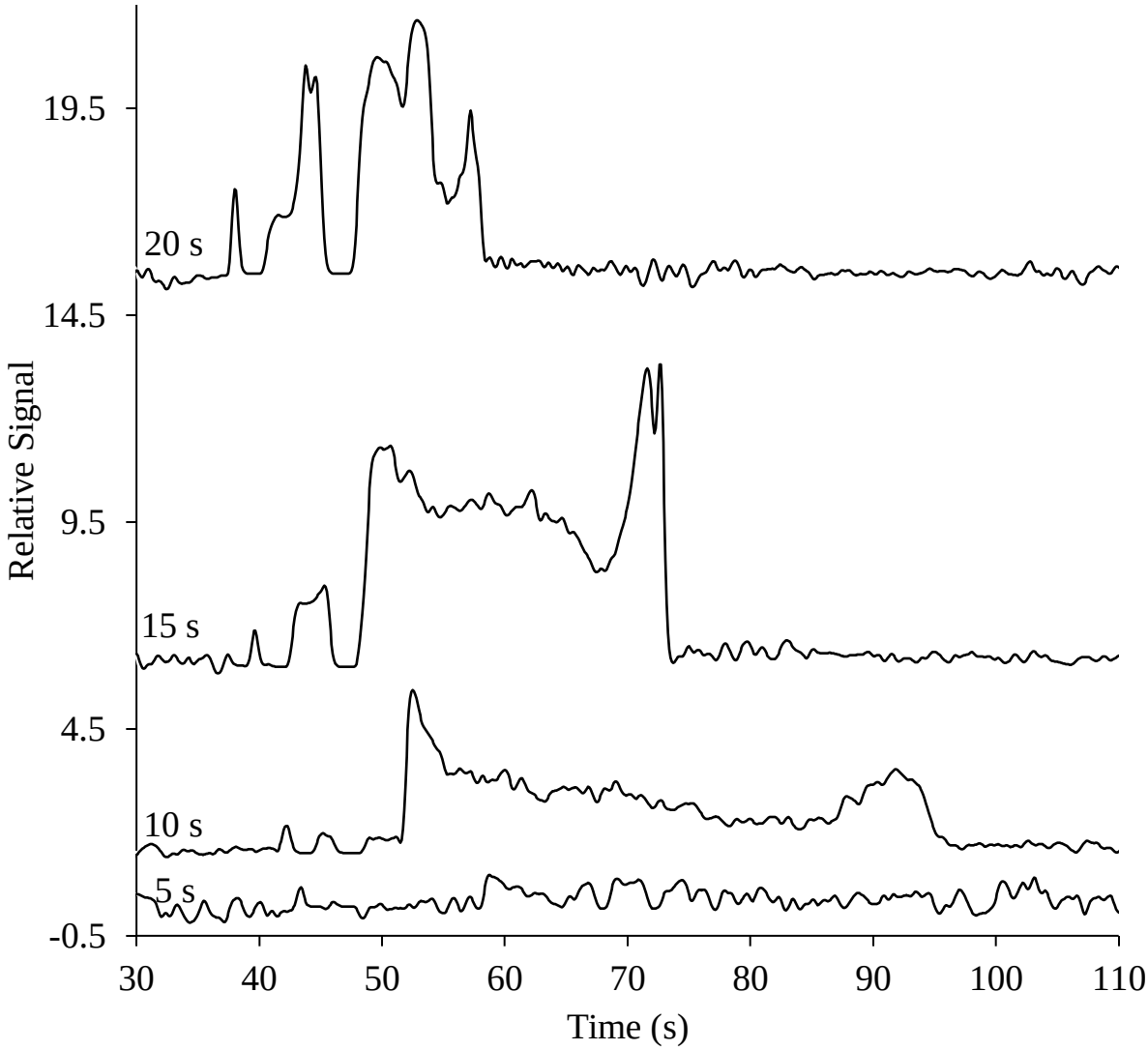

Figure 3-10 Electropherograms of Chromeo P503-conjugated HER2 at a concentration of 4.2 μM detected by laser wave mixing detector using a 473 nm laser. Samples are in sample buffer (25 mM Tris-CHES, pH 9.0). Capillary: 75 μm i.d., 30 cm (15 cm effective). The capillary is rinsed with NaOH (0.1 M), water, UltraTrol LN, and background electrolyte (50 mM Tris-CHES, pH 9.0, 40 mM SDS) for 2 minutes, respectively. The sample is injected electrokinetically at -10 kV for 5 s, 10 s, 15 s, and 20 s, respectively. -18 kV is applied for each run.

down when they encounter the BGE region with low electric field strength (Kim & Terabe, 2003).

3.4.3 Capillary Sieving Electrophoresis

CSE separates proteins based on the difference in their molecular size. Figure 3-11 shows the CE separation of FITC-labeled protein molecular weight markers, including β-galactosidase (116.0 kDa), BSA (66.2 kDa), ovalbumin (45.0 kDa), lactate dehydrogenase (35.0 kDa), REase Bsp98I (25.0 kDa), β-lactoglobulin (18.4 kDa) and lysozyme (14.4 kDa). UltraTrol LN is used as a dynamic coating to suppress EOF because EOF causes the sieving matrix (PEG) extrusion out of the bare fused silica capillary (Nakatani *et al*., 1994). PEG matrix is used as a sieving matrix because it is a water-soluble, low-viscosity polymer. Unlike rigid gels that are easily contaminated by samples and hard to be regenerated, PEG can be replaced after each run (Shieh *et al*., 1994). Increasing the concentration of PEG enhances resolution, but it can also cause uneven distribution of the sieving matrix in capillary and fluctuation of the CE current. The wave-mixing signal of BSA is the strongest among the seven proteins because it has the most lysine groups (59 total), and β-galactosidase yields more multiple peaks because it is a tetramer enzyme (Huber, 2013).

Figure 3-12 shows the linear plot of the log of molecular weight and average migration time in CSE. The average migration time is proportional to the log of protein molecular weight. The linear relationship ($R^2 > 0.99$) proves the sieving mechanism of PEG, a size-based separation. Relative standard deviations for the migration times of seven peaks are lower than 1.7%, and this low value indicates a small spread of migration times. The calibration curve can estimate the molecular weights of unknown samples.

One could use different excitation sources and protein labels that exhibit significantly different maximum absorption wavelengths to establish the standard migration times of proteins. Figure 3-13 shows the separation of FITC-conjugated BSA and Chromeo P503-conjugated

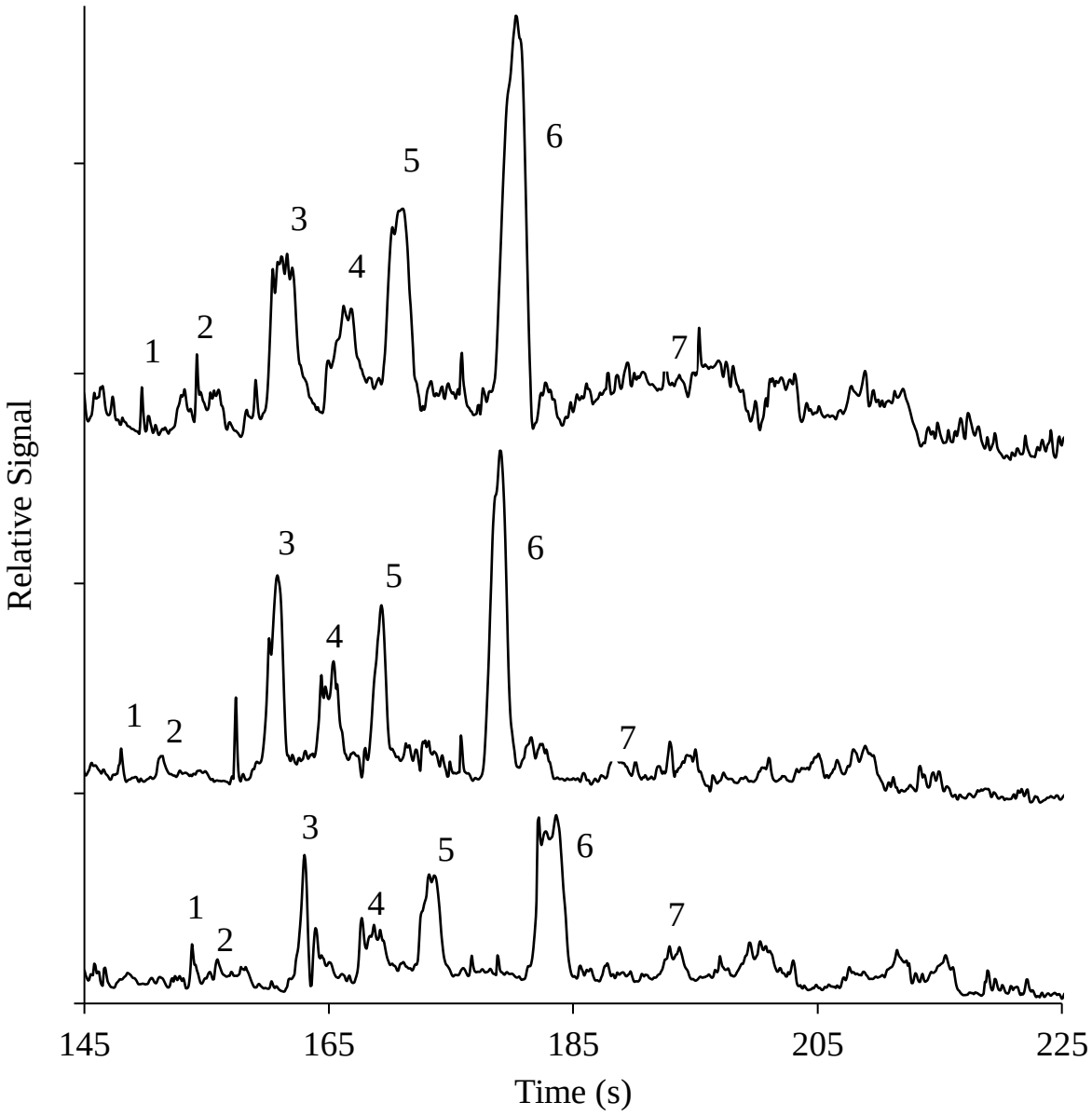

Figure 3-11 Electropherograms of FITC-labeled protein ladder, including (1) lysozyme, (2) β-lactoglobulin, (3) REase Bsp98I, (4) lactate dehydrogenase, (5) ovalbumin, (6) bovine serum albumin, and (7) β-galactosidase, detected by laser wave mixing using a 473 nm laser. The protein ladder is at a concentration of 10 to 20 μg. The sample buffer is 25 mM Tris-CHES, pH 9.0, 0.1% SDS, and the capillary (75 μm i.d., 40 cm total, 20 cm effective) is rinsed with NaOH (0.1 M), water, UltraTrol LN, and sieving matrix (100 mM Tris-CHES, pH 9.0, 3% PEG 10,000) for 2 minutes. The sample is injected electrokinetically at -5kV for 3 s, and -15 kV is applied for each run.

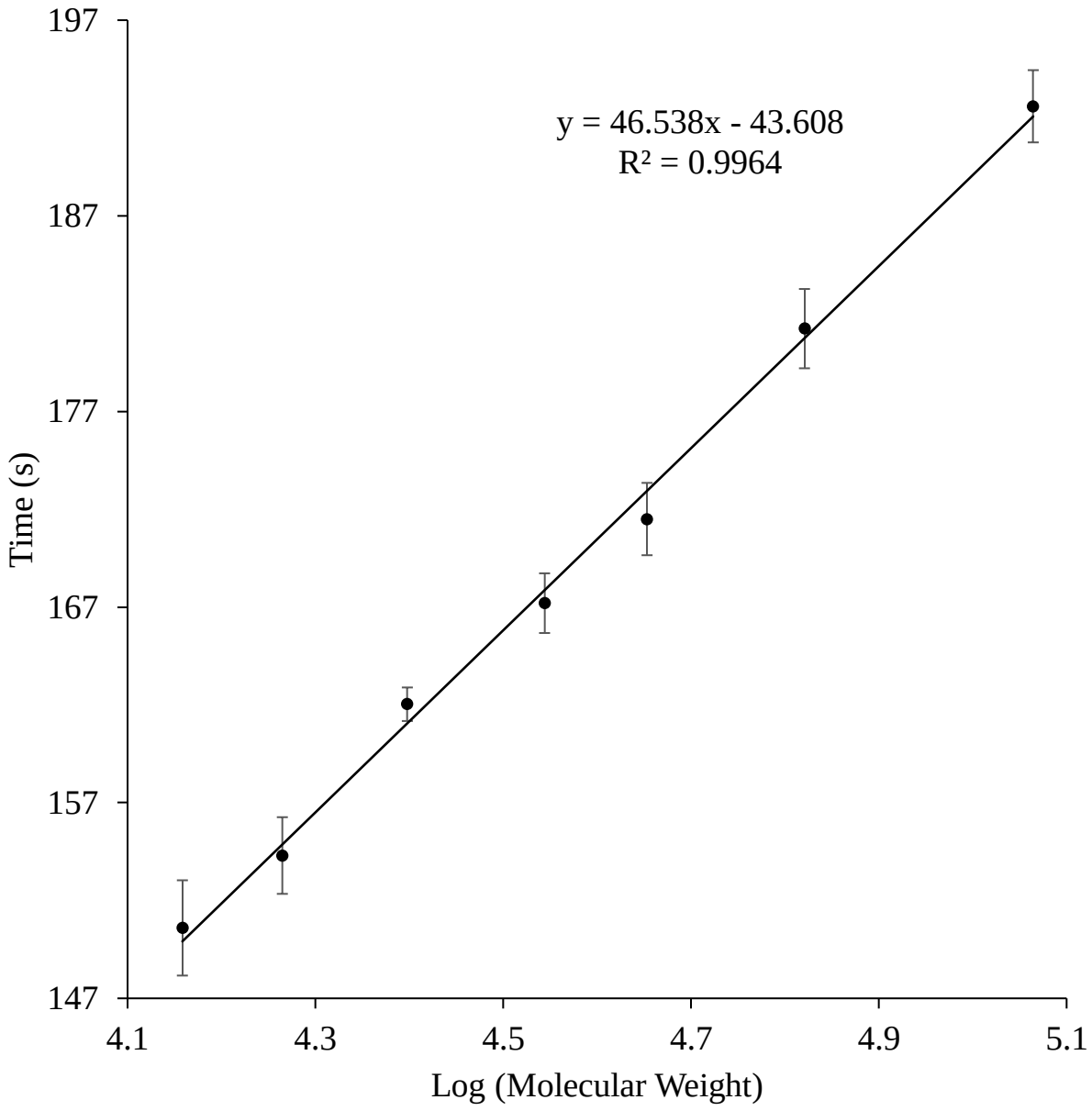

Figure 3-12 Calibration curve for seven protein markers.

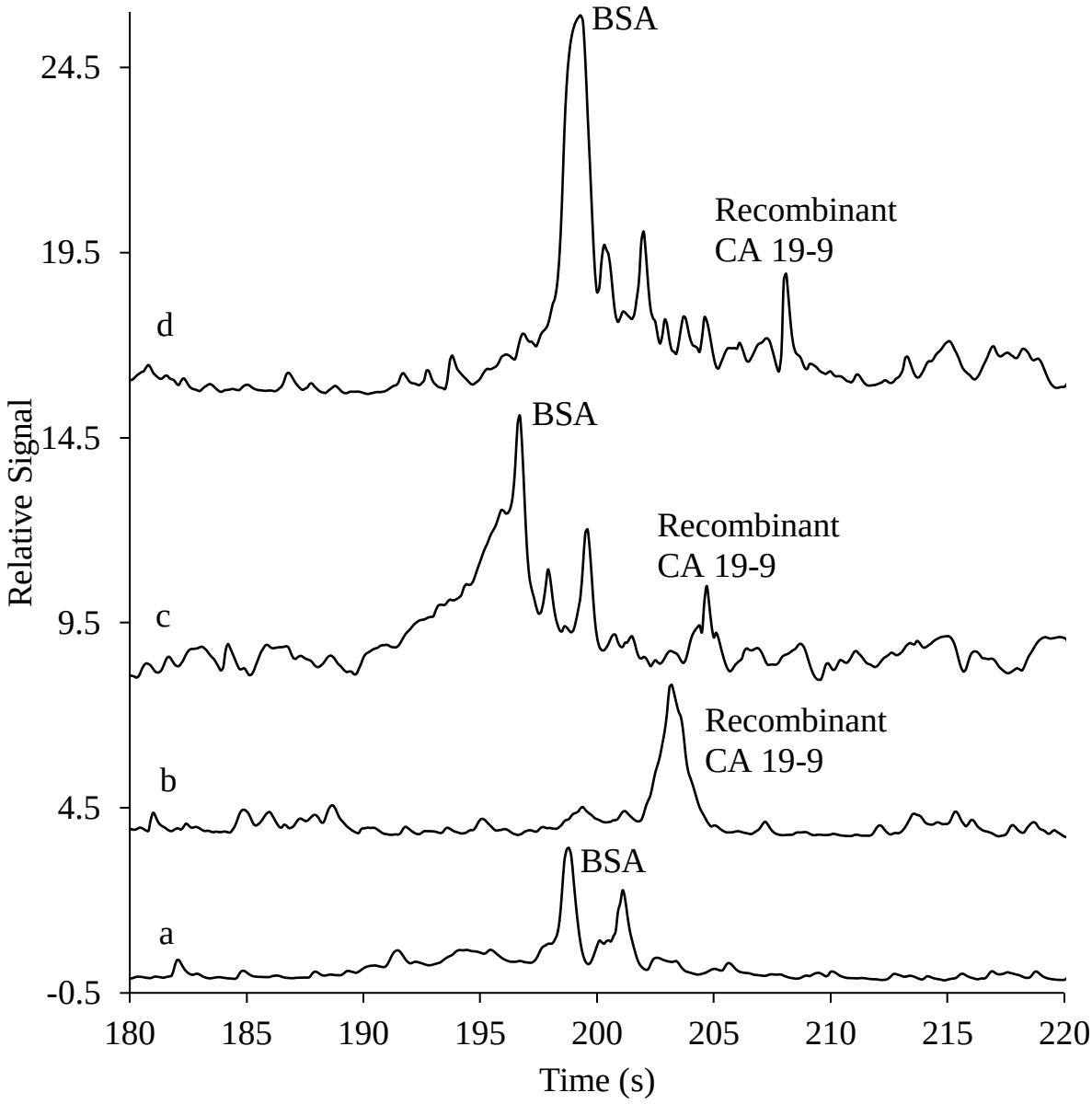

Figure 3-13 Electropherograms of a) Chromeo P503-conjugated recombinant CA 19-9 at a concentration of 5 μM, b) FITC-conjugated BSA at a concentration of 5 μM, and c) and d) separation of Chromeo P503-conjugated recombinant CA 19-9 and FITC-conjugated BSA at a concentration of 2.5 μM detected by laser wave mixing detector using a 473 nm laser. Samples are in sample buffer (25 mM Tris-CHES, pH 9.0, 0.1% SDS). Capillary: 75 μm i.d., 45 cm (25 cm effective). The capillary is rinsed with NaOH (0.1 M), water, UltraTrol LN, and background electrolyte (100 mM Tris-CHES, pH 9.0, 3% PEG 10,000) for 2 minutes, respectively. The sample is injected electrokinetically at -10 kV for 5 s. -15 kV is applied for each run.

recombinant CA 19-9. Recombinant CA 19-9 is galactoside 3(4)-L-fucosyltransferase that aids the synthesis of CA 19-9 by adding fucose to the precursor in the last step of biosynthesis (US National Library of Medicine, 2022). Like NHS-rhodamine, the maximum absorption and emission wavelength of FITC are similar before and after binding to BSA (Lai *et al*., 2013; Kästner *et al*., 2018). The FITC-conjugated BSA emits green fluorescence. However, Chromeo P503 exhibits a shorter maximum excitation and emission wavelength upon conjugation with CA 19-9. Chromeo P503-conjugated recombinant CA 19-9 emits red fluorescence (Activemotif, n.d.). Their maximum absorption wavelengths are too close, so using two laser excitation sources to distinguish them is challenging. However, our naked eyes can observe the different fluorescence colors because the concentrations of analytes are relatively high (5 μM). Therefore, the fluorescence color difference can distinguish BSA and recombinant CA 19-9. Multiple labeling sites can cause multiple peaks because not all proteins are labeled completely.

Both the protein structures and molecular weights affect migration times in CSE. The molecular weight of recombinant CA 19-9 is 43 kDa as determined by SDS-PAGE (MyBioSource, 2016), whereas the molecular weight of BSA is 66.4 kDa. However, the migration time of recombinant CA 19-9 is longer than the migration time of BSA. Post-translation modification (e.g., phosphorylation and glycosylation) might cause the actual migration time differs from the predicted one (Guttman *et al*., 1994). On the other hand, a larger recombinant CA 19-9 molecule could be attributed to its irregular shape predicted by AlphaFold.

3.5 Conclusion

A laser wave-mixing detector provides highly sensitive absorption-based optical detection of proteins. When interfaced with CE, wave mixing yields enhanced sensitivity and specificity

levels. Analytes are focused by online sample concentration effects in the capillary and yield enhanced detection sensitivity. The lower detection limit of pancreatic cancer biomarker CA19-9 is 14 U/mL, below the cutoff value. Also, CE can offer specificity by identifying free dyes and dye-conjugated protein, and it can also separate protein by various CE modes: (1) charge-to-size ratio (CZE), (2) affinity of analyte toward phase, and (3) molecular size. Therefore, a wide range of proteins can be detected simultaneously. DFWM-CE exhibits inherent advantages. For example, it requires a small sample volume, and the probe volume is small. Hence, the mass detection limit is impressively low. It is a compact and cost-effective detector because the inexpensive and low-power laser serves as the excitation source of the DFWM-CE setup.

3.6 Acknowledgements

A part of the material for this chapter comes from a manuscript entitled “Ultrasensitive Detection and Separation of Pancreatic Cancer Biomarker CA 19-9 Using a Multiphoton Laser Wave-Mixing Detector Interfaced to Capillary Electrophoresis,” by Jie Liang and William G. Tong, published in ACS Omega, 2023. The Dissertation author is the first author of this manuscript.

We acknowledge partial support of this work by the U.S. Dept. of Homeland Security Science and Technology Directorate, the U.S. Dept. of Defense, the Army Research Office, the NSF, the NIH (R01), and the NIH IMSD (2R25GM058906).

3.7 References

Activemotif. (n.d.-a). *Chromeo™ P503*. https://www.activemotif.com/documents/1641.pdf

Aranas, A. T., Guidote, A. M., & Quirino, J. P. (2009). Sweeping and new on-line sample preconcentration techniques in capillary electrophoresis. *Analytical and Bioanalytical Chemistry*, *394*(1), 175–185. https://doi.org/10.1007/s00216-009-2646-7

Berniolles, S., Wu, Z., & Tong, W. G. (1994). Diode laser-based nonlinear degenerate four-wave mixing analytical spectrometry. *Spectrochimica Acta Part B: Atomic Spectroscopy*, *49*(12–14), 1473–1481. https://doi.org/10.1016/0584-8547(94)80123-1

Bharadwaj, R., & Santiago, J. G. (2005). Dynamics of field-amplified sample stacking. *Journal of Fluid Mechanics*, *543*(1), 57. https://doi.org/10.1017/s0022112005005975

Burgi, D. S., & Chien, R. L. (1991). Optimization in sample stacking for high-performance capillary electrophoresis. *Analytical Chemistry*, *63*(18), 2042–2047. https://doi.org/10.1021/ac00018a028

Chien, R. L., & Burgi, D. S. (1992). On-column sample concentration using field amplification in CZE. *Analytical Chemistry*, *64*(8), 489A-496A.

Dickerson, J. A., & Dovichi, N. J. (2010). Capillary sieving electrophoresis and micellar electrokinetic capillary chromatography produce highly correlated separation of tryptic digests. *ELECTROPHORESIS*, *31*(14), 2461–2464. https://doi.org/10.1002/elps.201000200

GAO, F., WANG, X. F., & ZHANG, B. (2019). Research and Application Progress of Micellar Electrokinetic Chromatography in Separation of Proteins. *Chinese Journal of Analytical Chemistry*, *47*(6), 805–813. https://doi.org/10.1016/s1872-2040(19)61163-1

Guttman, A., Shieh, P., Lindahl, J., & Cooke, N. (1994). Capillary sodium dodecyl sulfate gel electrophoresis of proteins II. On the Ferguson method in polyethylene oxide gels. *Journal of Chromatography A*, *676*(1), 227–231. https://doi.org/10.1016/0021-9673(94)80464-8

Huber, R. (2013). Beta (β)-Galactosidase. *Brenner's Encyclopedia of Genetics*, 326–328. https://doi.org/10.1016/b978-0-12-374984-0.00149-2

Iwabuchi, M. F. (2015). *Degenerate Four-Wave mixing interfaced with capillary electrophoresis as a bioanalytical method for small molecules, peptides, and proteins* [Ph.D. Dissertation]. University of California, San Diego.

Joselito P. Quirino, Shigeru Terabe, & Petr Boček. (2000). Sweeping of Neutral Analytes in Electrokinetic Chromatography with High-Salt-Containing Matrixes. *Analytical Chemistry*, *72*(8), 1934–1940. http://doi.org/10.1021/ac990566

K M Al Azzam. (2022). A novel and simple dynamic coating capillary electrophoresis method for the chiral separation and quantification of mitiglinide enantiomers using hydroxyethyl cellulose as a dynamic coating agent. *Die Pharmazie*, *77*(3), 95–102. https://doi.org/10.1691/ph.2022.1166

Kästner, C., Böhmert, L., Braeuning, A., Lampen, A., & Thünemann, A. F. (2018). Fate of Fluorescence Labels—Their Adsorption and Desorption Kinetics to Silver Nanoparticles. *Langmuir*, *34*(24), 7153–7160. https://doi.org/10.1021/acs.langmuir.8b01305

Kim, J. B., & Terabe, S. (2003). On-line sample preconcentration techniques in micellar electrokinetic chromatography. *Journal of Pharmaceutical and Biomedical Analysis*, *30*(6), 1625–1643. https://doi.org/10.1016/s0731-7085(02)00509-5

Lai, Y., Lin, L., Pan, F., Huang, J., Song, R., Huang, Y., Lin, C., Fuchs, H., & Chi, L. (2013). Bioinspired Patterning with Extreme Wettability Contrast on TiO_2Nanotube Array Surface: A Versatile Platform for Biomedical Applications. *Small*, *9*(17), 2945–2953. https://doi.org/10.1002/smll.201300187

Lele, M., Lele, S. M., Petersen, J. R., & Mohammad, A. (2001). Capillary Electrophoresis. *Clinical and Forensic Applications of Capillary Electrophoresis*, 3–19. https://doi.org/10.1007/978-1-59259-120-6_1

Lewis, A. H., Cranny, A., Harris, N., Green, N. G., Wharton, J., Wood, R., & Stokes, K. (2013). Review on the development of truly portable and *in-situ* capillary electrophoresis systems. *Measurement Science and Technology*, *24*(4), 042001. https://doi.org/10.1088/0957-0233/24/4/042001

Lin, C. H., & Kaneta, T. (2004). On-line sample concentration techniques in capillary electrophoresis: Velocity gradient techniques and sample concentration techniques for biomolecules. *ELECTROPHORESIS*, *25*(23–24), 4058–4073. https://doi.org/10.1002/elps.200406172

Marina, M. L., Ríos, A., & Valcárcel, M. (2005, November 9). *Analysis and Detection by Capillary Electrophoresis (Volume 45) (Comprehensive Analytical Chemistry, Volume 45)* (1st ed.). Elsevier Science.

MyBioSource (2016). *Recombinant Carbohydrate Antigen 19-9 (CA19-9)*. Retrieved November 9, 2022, from https://cdn.mybiosource.com/tds/protocol_manuals/800000-9999999/MBS7233106.pdf

Nakatani, M., Shibukawa, A., & Nakagawa, T. (1994). High-performance capillary electrophoresis of SDS-proteins using pullulan solution as separation matrix. *Journal of Chromatography A*, *672*(1–2), 213–218. https://doi.org/10.1016/0021-9673(94)80609-8

Quirino, J. P., & Terabe, S. (1999). Sweeping of Analyte Zones in Electrokinetic Chromatography. *Analytical Chemistry*, *71*(8), 1638–1644. https://doi.org/10.1021/ac9810866

Quirino, J. P., & Terabe, S. (2000). Sample stacking of cationic and anionic analytes in capillary electrophoresis. *Journal of Chromatography A*, *902*(1), 119–135. https://doi.org/10.1016/s0021-9673(00)00812-8

Rizvi, S. A. A., Do, D. P., & Saleh, A. M. (2011). Fundamentals of micellar electrokinetic chromatography (MEKC). *European Journal of Chemistry*, *2*(2), 276–281. https://doi.org/10.5155/eurjchem.2.2.276-281.401

Shieh, P. C., Hoang, D., Guttman, A., & Cooke, N. (1994). Capillary sodium dodecyl sulfate gel electrophoresis of proteins I. Reproducibility and stability. *Journal of Chromatography A*, *676*(1), 219–226. https://doi.org/10.1016/0021-9673(94)80463-x

Skwarek, E., Bolbukh, Y., Tertykh, V., & Janusz, W. (2016). Electrokinetic Properties of the Pristine and Oxidized MWCNT Depending on the Electrolyte Type and Concentration. *Nanoscale Research Letters*, *11*(1). https://doi.org/10.1186/s11671-016-1367-z

Suprapto, J., & Tong, W. G. (2023). Sensitive detection of heart-failure biomarkers natriuretic peptides using multi-photon laser wave-mixing spectroscopy. *Talanta*, *253*, 123859. https://doi.org/10.1016/j.talanta.2022.123859

Tai, W., Mahato, R., & Cheng, K. (2010). The role of HER2 in cancer therapy and targeted drug delivery. *Journal of Controlled Release*, *146*(3), 264–275. https://doi.org/10.1016/j.jconrel.2010.04.009

Target Discovery, Inc. (2017). *UltraTrol® Dynamic Coatings User Manual*. https://veritomyx.sharefile.com/share/view/sa5fcf917eeb4d6cb

Terabe, S., Otsuka, K., Ichikawa, K., Tsuchiya, A., & Ando, T. (1984). Electrokinetic separations with micellar solutions and open-tubular capillaries. *Analytical Chemistry*, *56*(1), 111–113. https://doi.org/10.1021/ac00265a031

US National Library of Medicine. (2022, October 26). *FUT3 fucosyltransferase 3 (Lewis blood group) [Homo Sapiens (human)] - gene - NCBI*. National Center for Biotechnology Information. Retrieved November 8, 2022, from https://www.ncbi.nlm.nih.gov/gene/2525#reference-sequences

Zheng, Z., Li, X., Gao, F., Liu, H., & Gao, Y. (2021). A sweeping-micellar electrokinetic chromatography method for the detection of three chlorophenols in cosmetic samples. *Acta Chromatographica*, *33*(4), 387–393. https://doi.org/10.1556/1326.2020.00812

Zhu, Z., Lu, J. J., & Liu, S. (2012). Protein separation by capillary gel electrophoresis: A review. *Analytica Chimica Acta*, *709*, 21–31. https://doi.org/10.1016/j.aca.2011.10.022

CHAPTER 4

ULTRASENSITIVE DETECTION AND SEPARATION OF PANCREATIC CANCER BIOMARKER CA 19-9 USING MULTI-PHOTON LASER WAVE-MIXING DETECTOR INTERFACED TO CAPILLARY ELECTROPHORESIS

4.1 Abstract

Carbohydrate antigen 19-9 (CA 19-9) is the most commonly used biomarker in the clinical diagnosis of pancreatic cancer. Multi-photon nonlinear laser wave-mixing spectroscopy is presented as an ultrasensitive detection method for pancreatic cancer biomarker CA 19-9. Wave mixing is an optical absorption-based method, and hence, it can detect both fluorescing and non-fluorescing biomarkers, i.e., labeled and label-free samples. Without time-consuming labeling steps, one can detect biomarkers in their native form using compact UV lasers. The wave-mixing signal beam is strong, collimated, and coherent (laser-like) and it can be efficiently collected using a simple photodetector with an excellent signal-to-noise ratio (S/N) against a dark background. The wave-mixing signal has a quadratic dependence on the analyte concentration, and thus, small changes in analytes can be monitored more effectively. In addition, the signal has a cubic dependence on the laser power, and hence, low power levels from compact lasers can be used efficiently. Compared to currently available detection methods, wave mixing offers inherent advantages such as short optical path length (micrometer-thin samples instead of 1-cm cuvette) and high spatial resolution (micrometer probe). Since the laser wave-mixing probe volume is small (picoliter), it is convenient to interface to microfluidics or capillary-based electrophoresis systems to enhance chemical specificity. Our wave-mixing detectors could be configured as

portable battery-powered devices suitable for field use. Potential real-world applications include the detection of various biomarkers, cancer cells, and early detection of diseases. We report a preliminary concentration detection limit of 0.009 U/mL, and a corresponding mass detection limit of 6.8 x 10^{-10} U (5.7 zeptomole), and these detection limits are better than those of chemiluminescence- or ELISA- based methods. Due to more optimal laser wave-mixing alignment and CE parameters, the detection sensitivity we obtained in this chapter is better than those in last chapter.

4.2 Introduction

4.2.1 Pancreatic Cancer

Pancreatic cancer is the third leading cause of cancer-related deaths in the U.S. and one of the most aggressive cancers in the world (Centers for Disease Control and Prevention, 2022). By 2030, pancreatic cancer will be the second most common cause of death from cancer (Rahib, 2014). The five-year survival rate of a pancreatic cancer patient is 11%, lower than most cancers (Siegel, 2021; American Cancer Society, 2022). Patients show physical and psychological symptoms such as severe pain, fatigue, loss of appetite, and a low sense of well-being (Tang, 2018). Approximately 80% of patients have already progressed to unresectable metastatic cancer at diagnosis because no currently available detection methods can reliably detect pancreatic cancer at an early stage (American Society of Clinical Oncology, 2022; Poruk *et al.*, 2013). Imaging techniques such as magnetic resonance imaging (MRI) and computed tomography (CT) lack the sensitivity levels needed for early detection. Other clinical methods, such as endoscopic ultrasound (EUS), endoscopic retrograde cholangiopancreatography (ERCP), and aspiration, are invasive (Zhang *et al.*, 2015). Thus, sensitive detection methods for biomarkers for the early

detection of pancreatic cancer are urgently needed. We report ultrasensitive detection of carbohydrate antigen 19-9 (CA 19-9) using a nonlinear multi-photon absorption-based detector interfaced with capillary electrophoresis (CE).

4.2.2 CA 19-9 as Biomarker for Pancreatic Cancer

CA19-9 is a gold-standard biomarker for pancreatic cancer and it is the only pancreatic cancer biomarker approved by the U.S. FDA (Ballehaninna & Chamberlain, 2013; Winter *et al*., 2012). It is a 210 kDa glycoprotein with tetrasaccharide carbohydrate epitope (Neu5Aca2,3Galb1,3 (Fuca1,4) GlcNAc) located on the protein core mucin (MUC-1) that could be released by the cancer cell (Bio-Rad Laboratories, 2019; Scarà *et al*., 2015; MyBioSource, n.d.). However, under native conditions, this carbohydrate determinant containing glycoprotein can reassociate to form aggregates with an average molecular weight of 1,000 kDa (Zhu *et al*., 2016; Zhang *et al*., 2016; Klug *et al*., 1988). Monoclonal antibodies against the human colon carcinoma cell lines can recognize and define units of CA 19-9 (Figure 4-1). Hence, CA 19-9 can form a biomarker panel with several proteins, e.g., carbohydrate antigen 242 (CA 242) and laminin gamma C (LAMC2), to improve the diagnosis of pancreatic cancer (Song *et al*., 2021). The normal level of CA 19-9 is lower than 37 U/mL, which corresponds to a desired detection sensitivity level of 81% and a specificity of 90% (Duffy, 1998).

4.2.3 Commercially Available and Published Detection Methods

Table 4-1 shows that chemiluminescence immunoassay (CLIA) and electrochemiluminescence immunoassay (ECLIA) are the two most popular commercially available methods (La'ulu & Roberts, 2007). Using CLIA, the CA 19-9 antigens are sandwiched

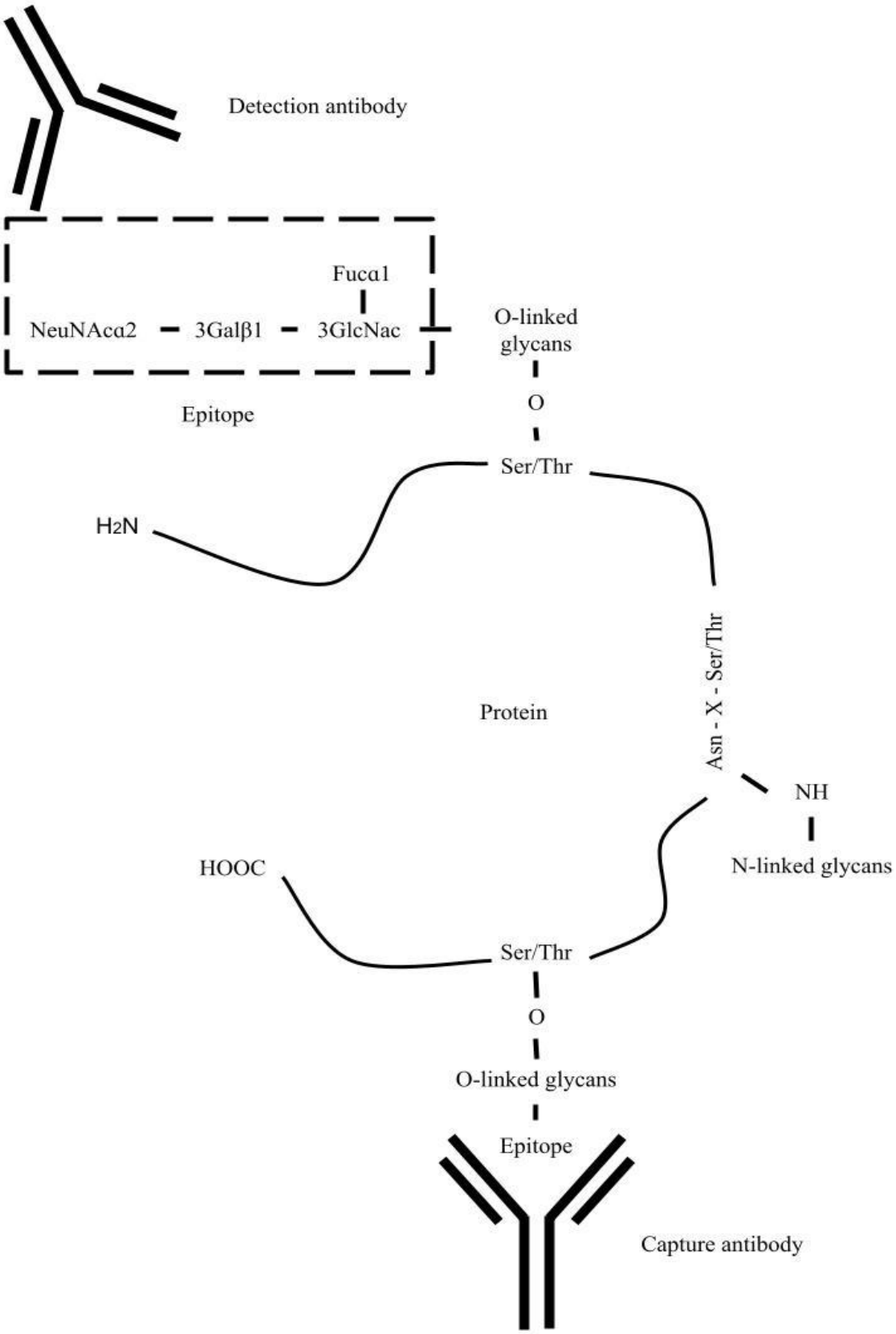

Figure 4-1 Structure of 1 unit of CA 19-9 (Klug *et al*. 1988)

Table 4-1 Comparison of selected commercially available methods for detection of CA19-9

Company	Instrument	Types of Assays	Volume (µL)	Lower Detection Limit (U/mL)	Unit Detection Limit (U)	Reference
Bayer Diagnostics	ADVIA Centaur	Direct Chemiluminescence using Acridinium Ester Technology	≥ 10.	0.43	4.3e-3	La'ulu & Roberts, 2007; Siemens Healthineers, n.d.
Abbott Diagnostics	ARCHITECT i2000	Chemiluminescent Microparticle Immunoassay	≥ 10.	0.23	2.3e-3	La'ulu & Roberts, 2007; Abbott, n.d.
Beckman Coulter	UniCel DxI 800	Chemiluminescent Immunoassay	≈ 25	0.070	1.8e-3	La'ulu & Roberts, 2007; Beckman Coulter, 2015
Diagnostic Products	IMMULITE 2000	Chemiluminescent Immunoassay	≥ 50.	0.32	1.6e-2	La'ulu & Roberts, 2007; Siemens Medical Solutions Diagnostics, 2007
Roche Diagnostics	Elecsys E170	Electrochemiluminescence Immunoassay	10.	0.070	7.0e-4	La'ulu & Roberts, 2007; Roche Diagnostics, 2017

between monoclonal CA 19-9 antibodies on pre-coated wells with the other monoclonal antibodies conjugated with label enzymes, e.g., horseradish peroxidase. The washing steps remove unbound antibodies. The substrate solution is then added to develop chemiluminescence for optical measurement. In ECLIA (ANOVA, n.d.), CA 19-9 is sandwiched between two CA 19-9 antibodies, and the detection antibodies are bound to the ruthenium complexes instead of enzymes, and the capture antibodies are immobilized on the electrodes instead of the wells. Applying a voltage triggers the redox reactions of the ruthenium complexes to initiate chemiluminescence. The ruthenium complex then relaxes to the ground state by emitting light captured by the detector (Richter, 2004). However, both CLIA and ECLIA methods require bulky instruments and large sample volumes. The mass detection limit of our laser wave-mixing method is orders of magnitude better than those possible using these commercially available detection methods. Additionally, our wave-mixing detection setup is compact, portable and suitable for field use.

Table 4-2 and Table 4-3 summarizes current available optical and non- optical detection methods, and many of them lack detection sensitivity, require large sample volumes, radioactive labels, or time-consuming and complicated experimental procedures. Among those methods, the near-infrared fluorescence enhancement immunoassay using plasmonic gold nano triangular arrays exhibits the best detection sensitivity, however, it is more time consuming and expensive to fabricate nanostructured arrays and immobilize proteins. Wave-mixing detection methods offer simple and fast detection and excellent mass detection limits that are comparable or better than those of fluorescence enhancement immunoassay.

4.2.4 DFWM as a Newly Developed CA 19-9 Detection Method

In this work, we have demonstrated excellent detection sensitivity levels for pancreatic

Table 4-2 Comparison of wave-mixing detection to other methods for CA 19-9

Method	Volume (μL)	Detection Limit (U/mL)	Detection Limit (U)	Reference
Fluorescence Immunoassay	50	7.0e-3	3.5e-4	Alarfaj *et al.*, 2018
Near-Infrared Fluorescence Enhancement Immunoassay Using Nanoarray	40.	7.7e-7	3.1e-8	Jawad *et al.*, 2017
Radioimmunometric Assay	1.0e2	1.4	1.4e-1	Del Villano *et al.*, 1983
ELISA	50.	3.0e-1	1.5e-2	Thermo Fisher Scientific, 2021
Photoelectrochemical Immunoassay	20.	3.9e-3	7.8e-5	Zhu *et al.*, 2016
Photoluminescence Immunoassay	30.	2.5e-1	7.5e-3	Gu *et al.*, 2011
Chemiluminescence Immunoassay	10.	1.6e-2	1.6e-4	Shi *et al.*, 2014
Electrochemiluminescence Immunoassay	5.0	5.0e-4	2.5e-6	Sha *et al.*, 2015
Flow cytometry	1.0e2	6.5e-1	6.5e-2	Leng *et al.*, 2016
Imaging Ellipsometry (IMBIE)	60.	1.0e1	6.0e-1	Huang *et al.*, 2016
Wave-mixing CE	7.5e-5	1.6e-1	1.2e-8	This work

Table 4-3 Comparison of published newly developed non-optical detection methods for CA19-9

Method	Volume (μL)	Lower Detection Limit (U/mL)	Unit Detection Limit (U)	Reference
Electrochemical immunoassay	1.0e3	1.4	1.4	Du *et al.*, 2007
Electrochemical Immunoassay	30.	5.0e-3	1.5e-4	D. Tang *et al.*, 2013
Electrochemical Immunoassay	30.	4.0e-2	1.2e-3	Gu *et al.*, 2011
Electrochemical Immunoassay	5.0	1.2e-3	6.0e-6	Sun & Qi, 2016
Electrochemical Immunoassay	N/A	6.0e-3	N/A	Yang *et al.*, 2015
Electrochemical Immunoassay	1.0e2	4.0e-3	4.0e-4	Hu *et al.*, 2013
Inductively coupled plasma mass spectrometry	10.	2.0e-2	2.0e-4	Ko & Lim, 2014

cancer biomarker CA 19-9 using our wave-mixing detection method. The laser wave-mixing signal intensity has a quadratic dependence on molar absorptivity and a cubic dependence on the laser input power intensity, as shown in Eq. 1.

$$I_{signal} \approx (\frac{b}{8\pi})^2 {I_1}^2 I_2 \frac{\lambda^2}{\sin^4\left(\frac{\theta}{2}\right)} \left(\frac{dn}{dT}\right)^2 \frac{\alpha^2}{\kappa^2} \qquad (4-1)$$

where b is the optical path length, I_1 is the intensity of the pump/probe input beam, I_2 is the intensity of the pump beam, λ is the wavelength of the input laser beams, θ is the angle between two input beams, dn/dT is the refractive index change based on temperature change, κ is the thermal conductivity of the medium, and α is the molar absorptivity of the analyte (Berniolles *et al*., 1994). The two put beams are tightly focused and mixed inside the sample in the capillary to create a small probe volume (nL to pL), as described by Eq. 4-2.

$$V = (\frac{2\lambda F}{\pi\omega})^2 \pi D \qquad (4-2)$$

where λ is the wavelength of the input laser beam, F is the focal length, ω is the beam radius, and D is the capillary diameter (Sirohi, 2017).

Hence, wave mixing allows effective interfacing to microchannels, microfluidics, and capillary-based separation systems for enhanced detection sensitivity and excellent chemical specificity, especially for challenging applications such as early detection of biomarkers for pancreatic cancer. These biomarkers can be detected in their native form label-free using a UV laser or labeled with a fluorophore or a chromophore using inexpensive and compact visible lasers. Since the wave-mixing signal beam is a coherent laser-like beam, one can collect virtually 100% of the signal beam against a dark background with excellent signal-to-noise ratios using simple, compact detection systems. Hence, laser wave mixing detectors can be designed to be portable

and compact for field use for early diagnosis of a wide range of diseases, including pancreatic cancer and other aggressive cancer types.

4.3 Experimental Setup

4.3.1 DFWM Setup

Figure 4-2 describes a typical laser wave-mixing optical setup coupled with a CE system. A continuous-wave diode-pumped solid-state laser (MGL-III-532nm or MBL-III-473nm, Opto Engine LLC., Midvale, UT) output is split (70:30 T:R) by a beam splitter (Thorlabs, Newton, NJ) to create two excitation beams and then focused and mixed inside the capillary using a lens (LA1509-A, Thorlabs, Newton, NJ) with a focal length of 10 cm. The angle between the two input beams is small (1.2° for the 532-nm laser setup and 1.5° for the 473-nm laser setup with a beam diameter of 1.9 mm and 1.5 mm, respectively). The sample cell is a fused silica capillary (75 μm i.d. and 365 μm o.d.) from Biotaq (Silver Springs, MD, USA). Burning off a portion of the polyimide coating (1 cm in length) on the capillary using a butane torch makes a clear optical detection window. Based on the radius of the beam waist at the focal point and the inner diameter of the capillary, the calculated probe volumes are 75 pL (532 nm laser) and 95 pL (473 nm laser). The stronger wave-mixing signal beam is collimated by a lens and collected using a photodiode (PDA36A, Thorlabs, Newton, NJ) with high efficiency since the signal beam is a coherent laser-like beam. An optical chopper (SR540, Stanford Research Systems, Sunnyvale, CA) is used to modulate one of the input beams at 320 Hz. The chopper is interfaced to a lock-in amplifier (SR810 DSP, Stanford Research Systems, Sunnyvale, CA) and the signal is digitized using a data acquisition system (1608FS, Measurement Computing, Norton, MA) and a custom-built software (AIDA).

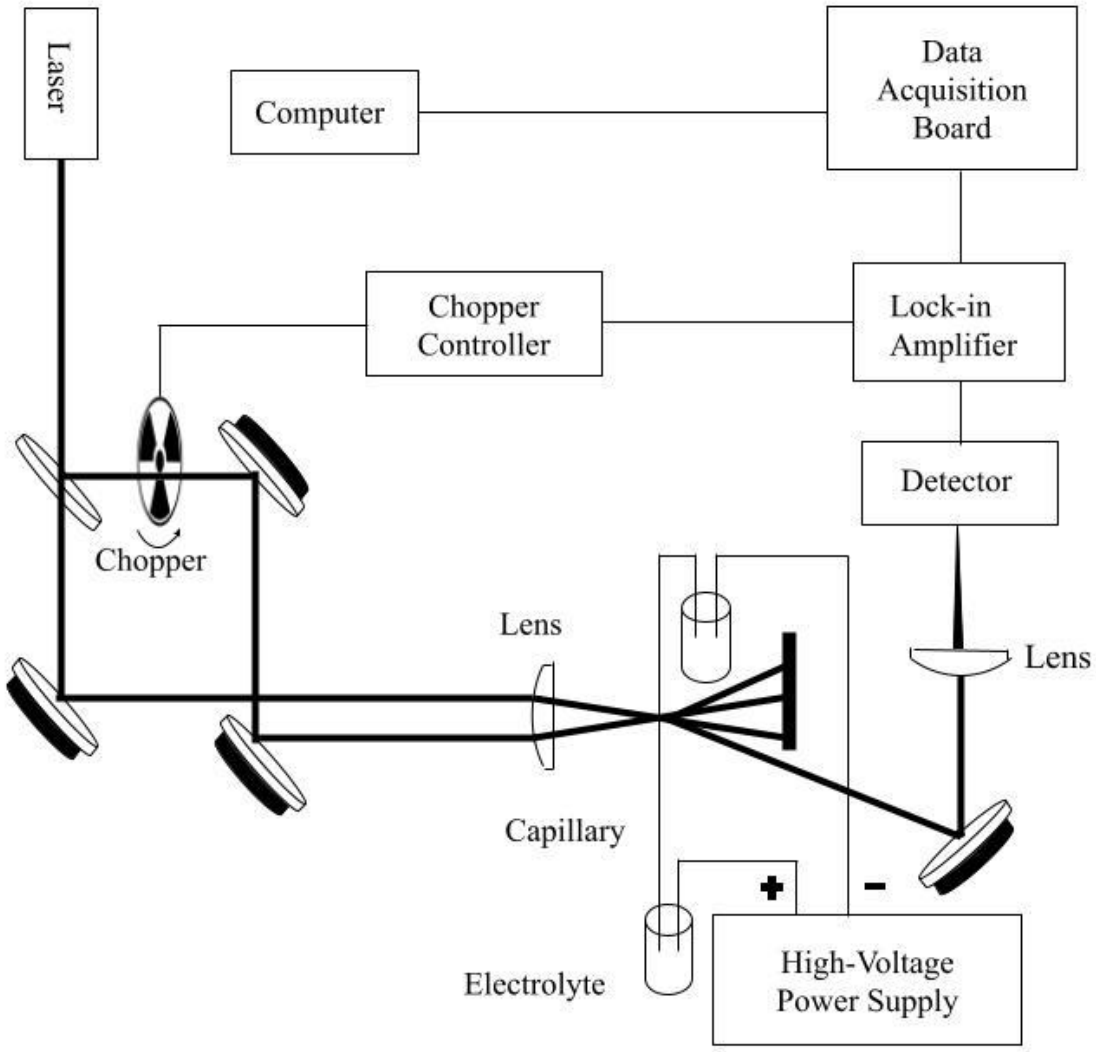

Figure 4-2 DFWM setup interfaced to CE system for CA 19-9 detection and separation.

4.3.2 Chemicals and Reagents

All solutions and buffers are prepared with ultrapure water from the PURELAB Flex system (ELGA LabWater North America, Woodridge, IL) and sonicated in a water bath (FS20, Fisher Scientific, Hampton, NH) for 10 minutes. All solutions and buffers used for capillary electrophoresis are filtered through a 0.20 μm syringe filter (GVS North America, Sanford, ME). Phosphate-buffered saline (Salem, MA), Bradford reagent, sodium bicarbonate, tris(hydroxymethyl)aminomethane (Trizma base), 2-(Cyclohexylamino) ethane sulfonic acid (CHES), hydrochloric acid, sodium hydroxide, electrophoresis-grade sodium dodecyl sulfate (SDS), sodium tetraborate decahydrate, polyethylene glycol (average M_v 10,000), polyethylene oxide (average M_v 100,000), cytochrome c from bovine and bovine serum albumin (BSA) are purchased from Millipore Sigma (Burlington, MA). Regenerated cellulose dialysis tubing (MW_{CO} 12-14 kDa), dye removal columns, N, N- *Dimethylformamide* (DMF), 5-(and 6)-carboxy tetramethylrhodamine, succinimidyl ester (NHS-Rhodamine), fluorescein isothiocyanate (FITC), Pierce unstained protein molecular weight marker (14.4 - 116 kDa) and BCA protein assay kit are obtained from Thermo Fisher Scientific (Waltham, MA). CA 19-9 native proteins (MyBioSource, San Diego, CA) are handled with microliter syringes (Microliter 700, Hamilton Reno, NV) because of the large density of CA 19-9. The protein is purified from the cell free supernatant by classical chromatography methods.

4.3.3 Protein Assays

For the Bradford assay, the stock CA 19-9 native protein solution is diluted to 314.87 U/mL with PBS buffer, and 3.0 mL of Bradford reagent are added to 100 μL of BSA in PBS buffer at concentrations of 0 mg/mL, 0.25 mg/mL, 0.5 mg/mL, 1.0 mg/mL, and 1.4 mg/mL, and 100 μL of

314.87 U/mL native CA 19-9. These samples are incubated at room temperature for 30 minutes. The optical absorbance at 595 nm is measured using a UV-visible spectrophotometer in order to prepare the standard curve.

For the bicinchoninic acid (BCA) assay, the working reagent is prepared by mixing 50 parts of 4% $CuSO_4$ (reagent A) and 1 part of 1% of BCA (reagent B) from Pierce BCA protein assay kit. The stock CA 19-9 protein solution is diluted to 314.87 U/mL with PBS buffer. Then, 2.0 mL of working reagents are added to 100 μL of BSA in PBS buffer at concentrations of 0 μg/mL, 25 μg/mL, 125 μg/mL, 250 μg/mL, 500 μg/mL, 750 μg/mL, 1000 μg/mL, 1500 μg/mL, 2000 μg/mL, along with 100 μL of 314.87 U/mL native CA 19-9. These samples are incubated at 37°C for 30 minutes. The optical absorbance at 562 nm is measured using a UV-visible spectrophotometer in order to prepare the standard curve.

4.3.4 Protein Labeling

Stock CA 19-9 native protein is diluted to 1600 U/mL. Dialysis of 500 μL 1,600 U/mL native CA 19-9 using regenerated cellulose dialysis tubing changes phosphate buffer (pH 7.4) to the desired levels for protein labeling.

For labeling, 1 mg of Chromeo Py dye (ActiveMotif, Carlsbad, CA) is dissolved in 100 μL DMF and the dye solution is added to the protein solution to obtain the desired label-to-protein molar ratios. The Chromeo P503-conjugated protein solution is incubated at room temperature for 30 minutes. The Chromeo P540-conjugated protein solution is incubated at room temperature for 1 hour or at 55 °C for 2 hours. The labeled protein is dialyzed and dissolved in the desired buffer in preparation for CE runs.

4.3.5 UV-Visible Spectroscopy

All the UV-visible absorption spectra are collected using a UV-visible spectrophotometer (Model 8453, Agilent, Santa Clara, CA). Samples are placed in Quartz cuvettes (Starna Cells, Inc., Atascadero, CA) or disposable UV cuvettes (Brand Tech Scientific Inc., Essex, CT) with a 1-cm path length. The blanks are obtained using corresponding solvents for the analytes.

The direct A280 absorbance measurement is taken using a NanoDrop Spectrophotometer (Model 2000c, Thermo Fisher Scientific, Waltham, MA). The optical absorbance of 2 μL of 2099 U/mL CA 19-9 is measured at 280 nm.

4.3.6 Power-Plot and Concentration-Plot

A compact power meter console (PM100A, Thorlabs, Newton, NJ) measures 473 nm laser input power before the detection window. The Chromeo P503 conjugated CA 19-9 are injected through the capillary using a peristaltic pump (RP-1, Rainin Instrument Co., Emeryville, CA) and manifold pump tubing (Thermo Fisher Scientific, Waltham, MA). Signals are collected by blocking two input beams alternatively. Running 0.1 M NaOH for 2 minutes through the capillary between runs cleans the capillary.

4.3.7 Capillary Electrophoresis

Background electrolytes are prepared by dissolving sodium tetraborate decahydrate powder, or Tris and CHES powder, in ultrapure water. Sodium hydroxide or hydrochloric acid is added until the desired pH is reached. Depending on the CE mode used, SDS is added to BGE at different concentration levels. The sieving matrix is prepared by dissolving PEO, 100,000 (2%) into Tris-CHES buffer (100 mM).

Before CE runs, the capillary is flushed with 0.1 M NaOH for 10 minutes, ultrapure water for 10 minutes, Ultratrol LN (Target Discovery, Palo Alto, CA) for 2 minutes, and the background electrolyte/sieving matrix for 10 minutes using a peristaltic pump (RP-1, Rainin Instrument Co., Emeryville, CA). After each run, 0.1 M NaOH, ultrapure water, Ultratrol LN, and the background electrolyte/sieving matrix are used to flush the capillary for two minutes each.

4.4 Results and Discussion

4.4.1 Quantification of CA 19-9 by Colorimetric Assays

Electrochemiluminescence immunoassay and enzyme immunoassay defines the arbitrary unit of CA 19-9. Direct A280 measurement and colorimetric assays, including Bradford and BCA assays, quantify CA 19-9. The Bradford reagent is prepared as an acidified solution of Coomassie Brilliant Blue G-250 (CBB) since CBB is cationic under acidic conditions. As shown in Figure 4-3, CBB is stabilized as an anionic form when binding to the protein via electrostatic interaction with the amino acids (arginine, lysine, and histidine) and hydrophobic interaction with the hydrophobic pockets (Gee *et al.*, 2017; Sherovski *et al.*, 2018). CBB exhibits a color change from reddish-brown to blue upon binding to protein. The absorption peak of CBB shifts from 465 nm to 595 nm, as shown in Figure 4-4, for the protein-dye complex in the concentration range of 0 - 1.4 mg/mL. BSA serves as a standard protein, and as its concentration is increased, the optical absorbance increases linearly at 595 nm.

The protein standards in the concentration range from 0 to 1.4 mg/mL are used to prepare the standard curve, as shown in Figure 4-5. The mass concentration of CA 19-9 is adjusted to fall within the concentration range of standard proteins. Different concentrations of CA 19-9 are tested with the Bradford reagent, and 314.87 U/mL concentration is chosen for CA 19-9. The mass

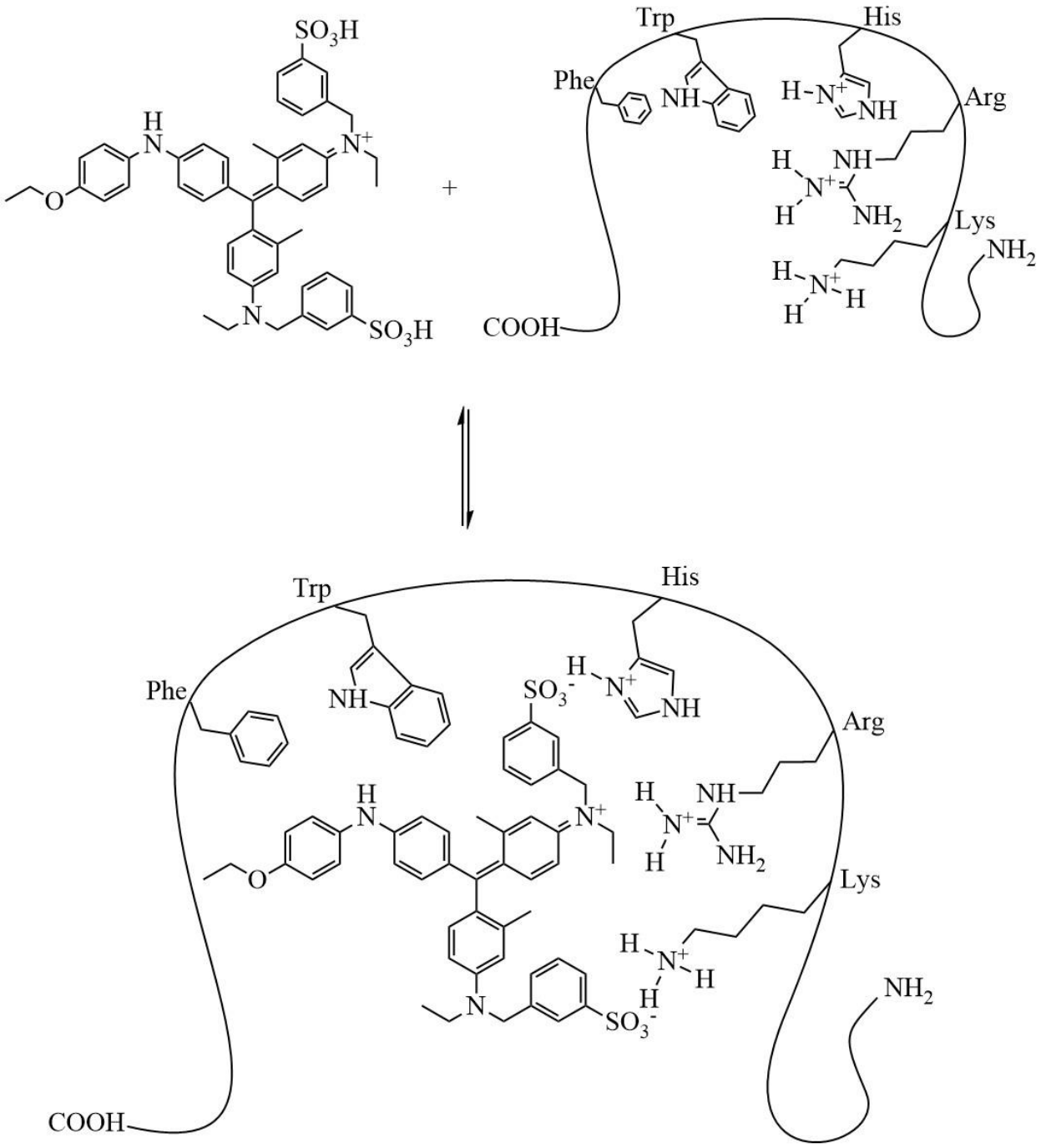

Figure 4-3 Chemical reaction schematic for the Bradford assay (Gee *et al*., 2017; Sherovski *et al*., 2018)

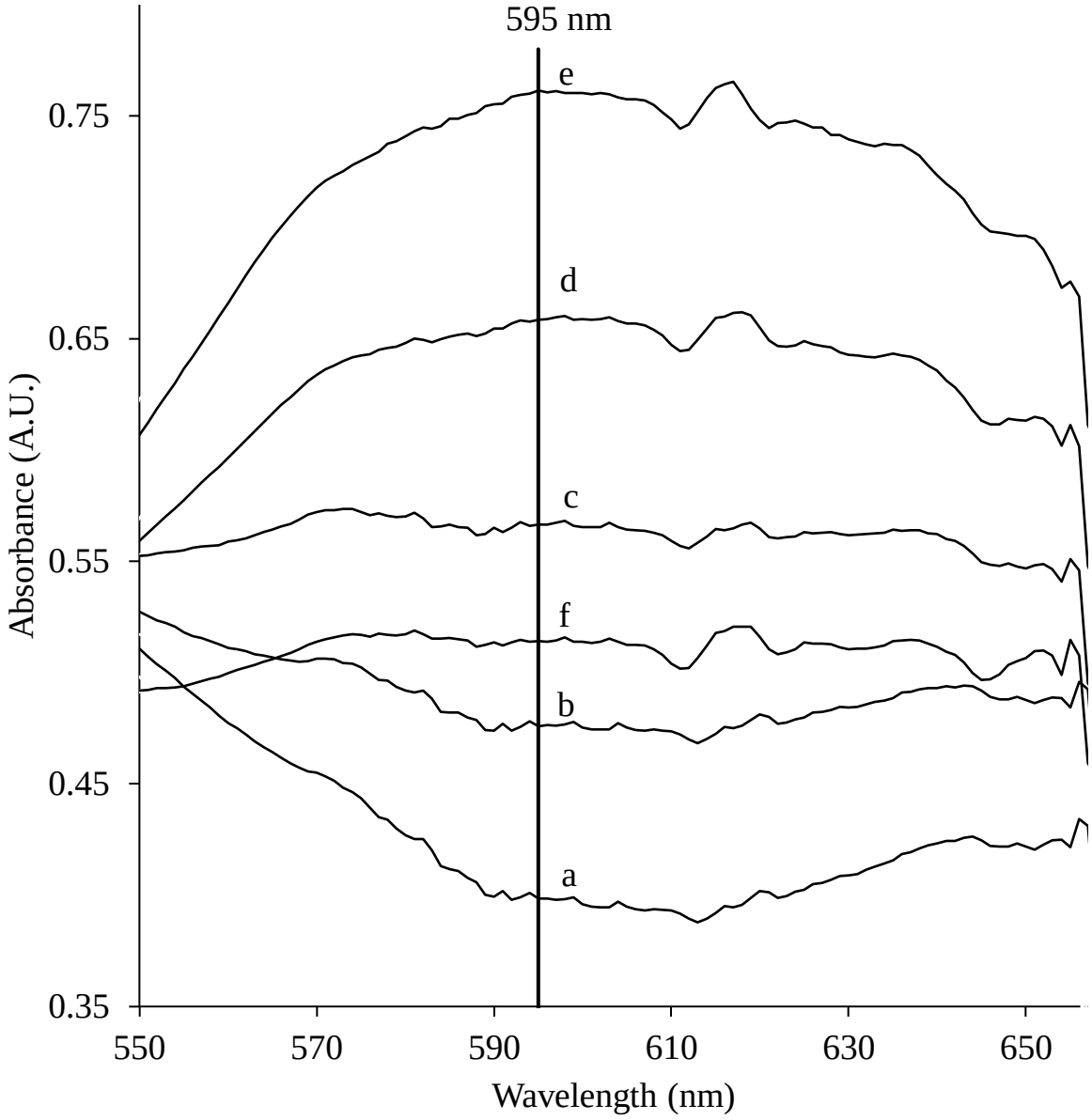

Figure 4-4 UV-visible absorption spectra of 3.0 mL Bradford reagent mixed with BSA at concentrations of (a) 0 mg/mL, (b) 0.25 mg/mL, (c) 0.5 mg/mL, (d) 1.0 mg/mL, (e) 1.4 mg/mL, and (f) CA 19-9 concentration of 314.87 U/mL.

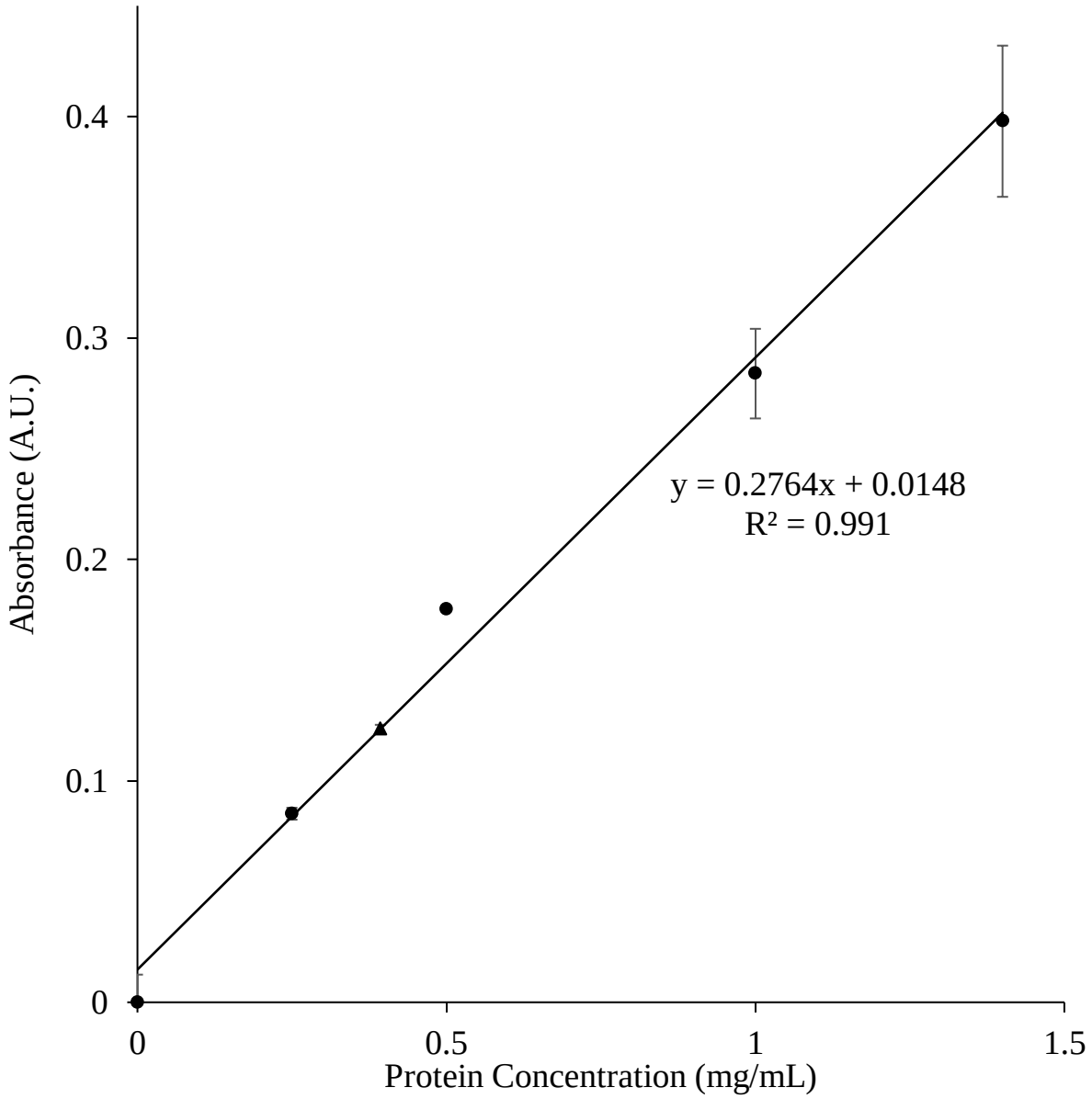

Figure 4-5 Bradford assay standard curve of BSA concentration (●) vs. absorbance at 595 nm and CA 19-9 concentration at 314.87 U/mL (▲) vs. absorbance at 595 nm.

concentration of protein present in the original 314.87 U/ml CA 19-9 is 0. 394 mg/mL, and hence, one unit of CA19-9 is estimated to contain 1.25 μg of protein.

As shown in Figure 4-6, The BCA assay is a copper-based colorimetric assay, with two BCA molecules forming a purple complex, and one Cu^{1+} is created by reducing Cu^{2+} in a basic environment (Smith *et al.*, 1985). The reduction of Cu^{2+} relies on the peptide bonds and four amino acids (cysteine, cystine, tryptophan, and tyrosine) side chains (Wiechelman *et al.*, 1988). Chelation of one Cu^{1+} and two molecules of BCA complex exhibits a color change from green to purple with the maximum absorbance at 562 nm.

Figure 4-7 shows UV-visible absorption spectra of the Cu^{1+} - BCA complex at increasing concentrations of BSA (from 0 to 2 mg/mL). As the concentration of BSA increases, the optical absorbance increases at 595 nm. The blank-corrected absorbance of protein standards in the concentration range of 0 - 2 mg/mL is used to make the standard curve, as shown in Figure 4-8.

A third-order polynomial equation provides a suitable method for interpolating the test sample concentration (two factors cause the nonlinearity). The relation between the protein concentration and the concentration of cuprous ions is nonlinear because nearly all the Cu^{2+} was reduced to Cu^{1+} when the protein is present at a high concentration level (saturated region). In addition, the protein competes with BCA for binding to Cu^{1+}. The presence of two-side complexes (BCA-Cu^{1+}- peptide bond and the peptide bone - Cu^{1+}- peptide bond) negatively affects the forming of a chromogenic complex of BCA-Cu^{1+}-BCA (Huang *et al.*, 2010).

The concentration of CA 19-9 needs to fall within the concentration range of standard proteins. Different concentrations of CA 19-9 are tested with the BCA working reagent, and 314.87 U/mL of CA 19-9 is used. The mass concentration of protein present in the original 314.87 U/ml CA 19-9 is 0. 396 mg/mL, and hence, one unit of CA19-9 is estimated to contain 1.26 μg of

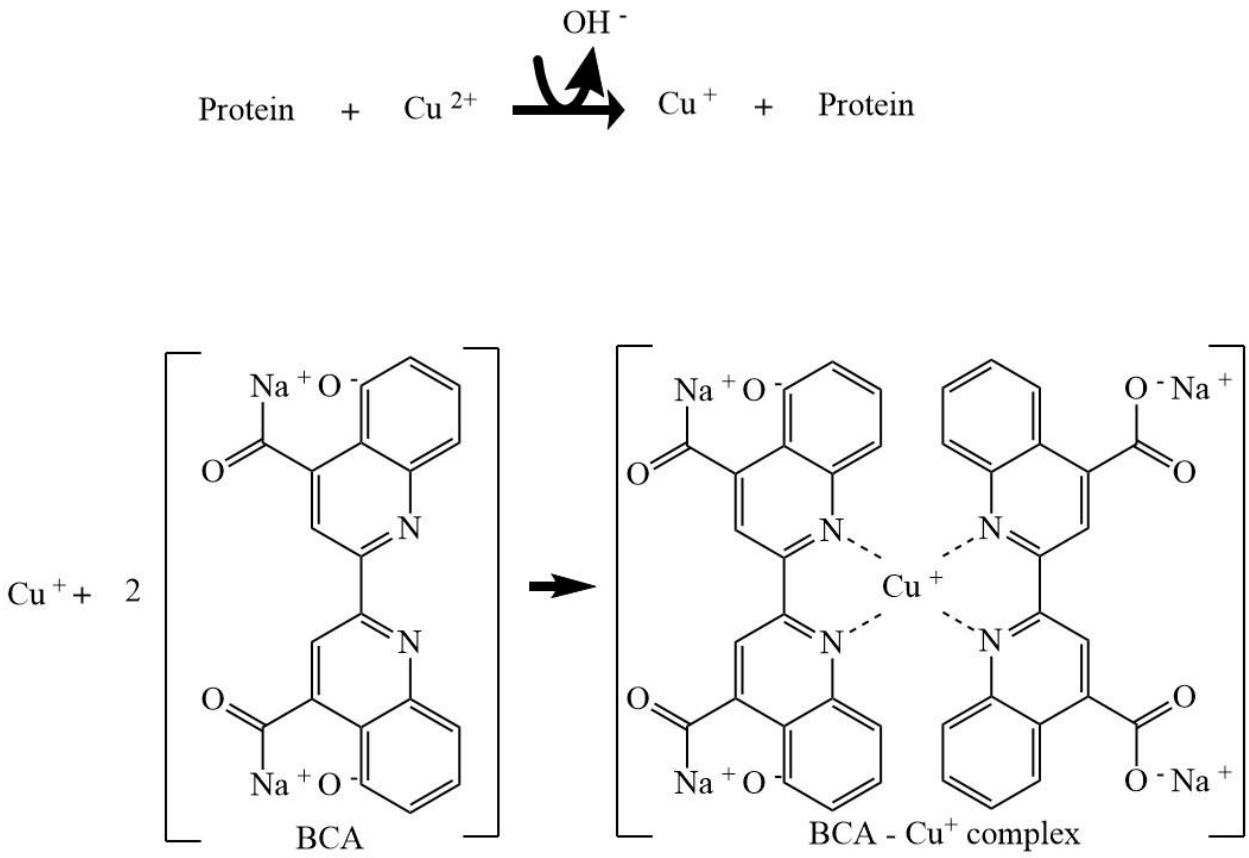

Figure 4-6 Reaction schematic for the BCA assay (Smith *et al*., 1985; Wiechelman *et al*., 1988).

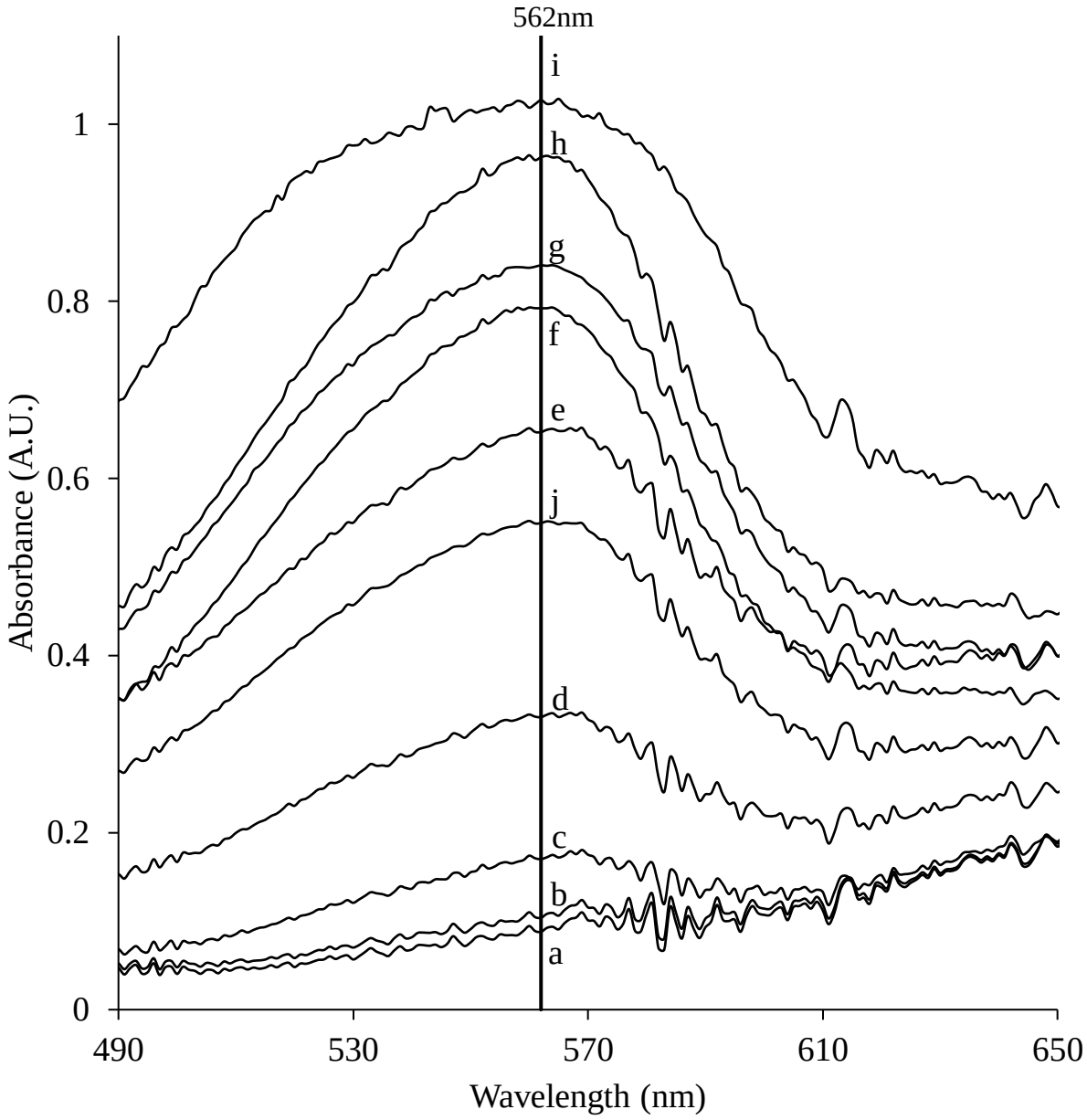

Figure 4-7 UV-visible absorption spectra of 2.0 mL BCA reagent mixed with BSA at concentrations of (a) 0 μg/mL, (b) 25 μg/mL, (c) 125 μg/mL, (d) 250 μg/mL, (e) 500 μg/mL, (f) 750 μg/mL, (g) 1000 μg/mL, (h) 1500 μg/mL, (i) 2000 μg/mL, and (j) CA 19-9 concentration of 314.87 U/mL.

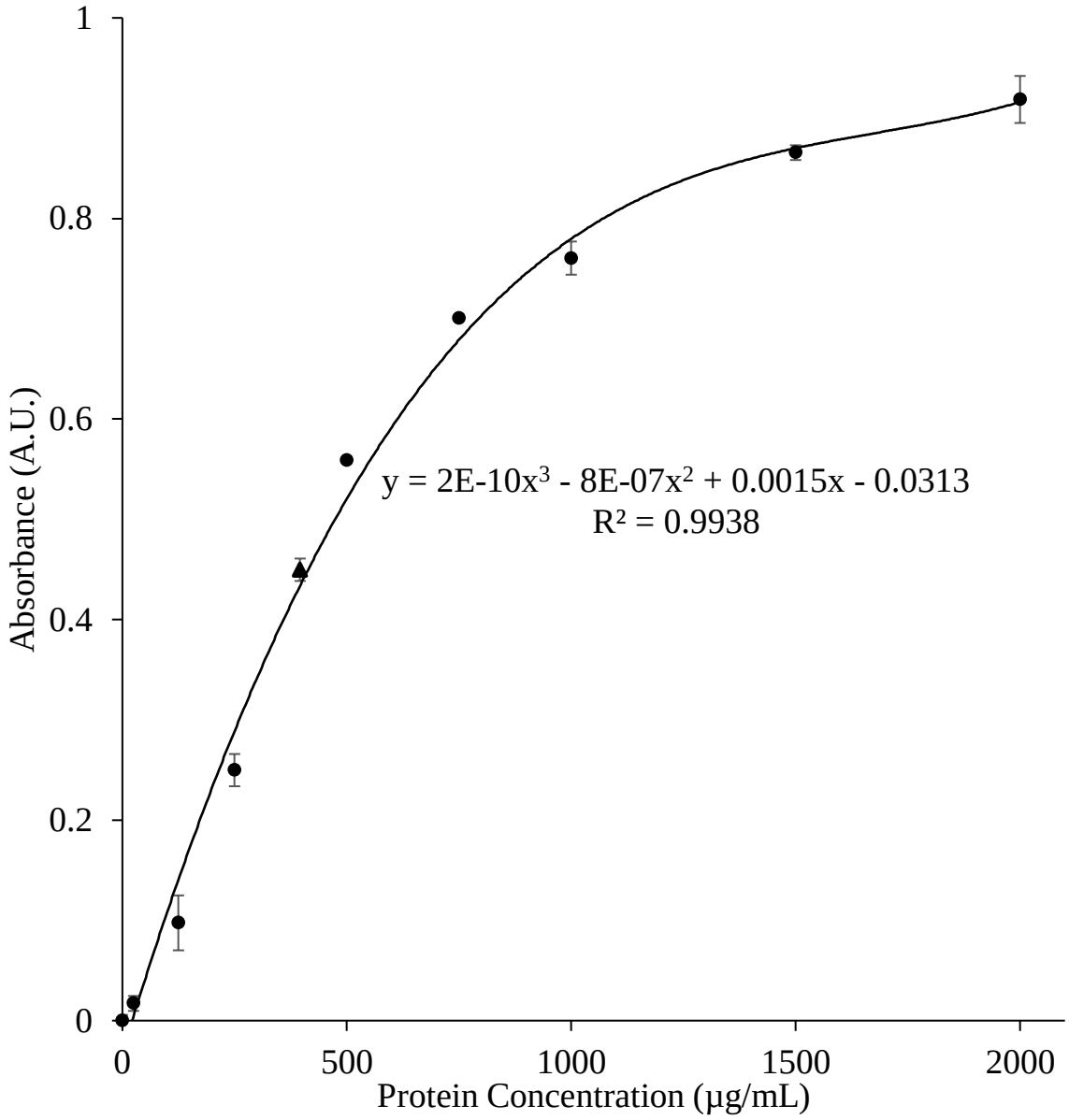

Figure 4-8 BCA assay standard curve of BSA concentration (●) vs. absorbance at 562 nm and CA 19-9 concentration of 314.87 U/mL (▲) vs. absorbance at 562 nm. Error bars represent one standard deviation of uncertainty.

protein.

The Protein A280 method is used for proteins containing tryptophan, tyrosine, or cysteine-cysteine disulfide bonds that absorb at 280 nm. The standard curve is not required, and hence, this method is faster. A general reference setting based on a 1 mg/mL protein yields an absorbance of 1.0 at 280 nm (Thermo Fisher Scientific, 2009). The absorbance of 2,099 U/mL CA 19-9 is 2.64, and hence, one unit of CA19-9 is estimated to contain 1.26 μg of protein.

Table 4-4 summarizes the results of the three methods of UV-Visible quantification of CA 19-9 mentioned above. It is determined that one unit of CA19-9 is estimated to contain 1.25 μg of protein. CA 19-9 is 85% carbohydrate by weight (Klug *et al*. 1988), and hence, the mass of one unit of CA 19-9 is estimated as 8.36 μg.

4.4.2 Protein Labeling using Chromeo Py-Dyes and Optimal Molar Ratios of Chromeo Py Dyes to CA 19-9

Native label-free CA 19-9 could also be detected using a UV laser-based wave-mixing detector since it exhibits optical absorption at UV wavelengths due to tyrosine and phenylalanine (Klug *et al*. 1988). However, labeling the protein with dyes allows one to use more compact and less expensive visible lasers.

Figure 4-9 shows molecular structures of Chromeo Py-Dyes used in this study. This study also uses Chromeo Py dyes, which are pyrylium dyes with heterocyclic aromatic rings with a bonded chromophore (McNeil 2012). Figure 4-10 shows pyrylium dyes converted to stable pyridium salts by reacting with the primary amine groups of the protein (McNeil, 2012; Bayer & König, 2016). Most importantly, one can skip the dialysis step.

Figure 4-11 shows UV-visible optical absorption of Chromeo P503-labeled CA 19-9 at the

Table 4-4 UV-Visible quantification of 1 unit of CA 19-9

Method	Absorbance	Standard Deviation of Absorbance (%)	% Coefficient of Variation of Absorbance (%)	Protein in 1 Unit CA 19-9 (µg)	Content in 1 Unit CA 19-9 (µg)
Bradford assay	0.124	0.184	1.49	1.25	8.33
BCA assay	0.450	1.12	2.49	1.26	8.39
Protein A280	2.64	1.70	0.643	1.26	8.38

a)

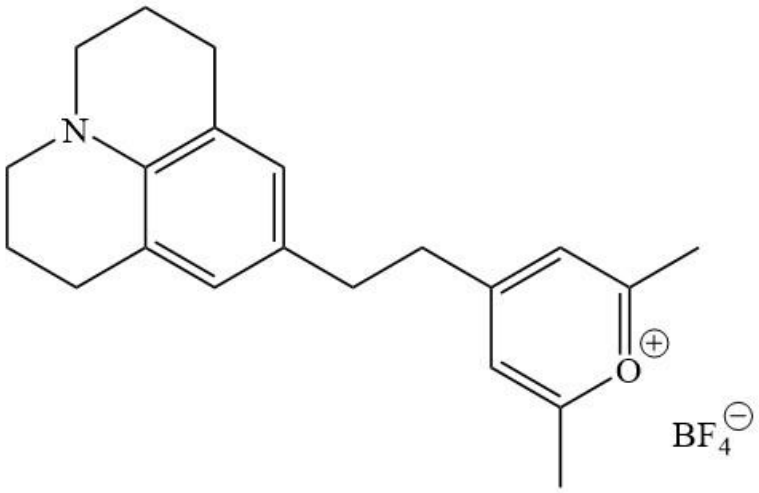

b)

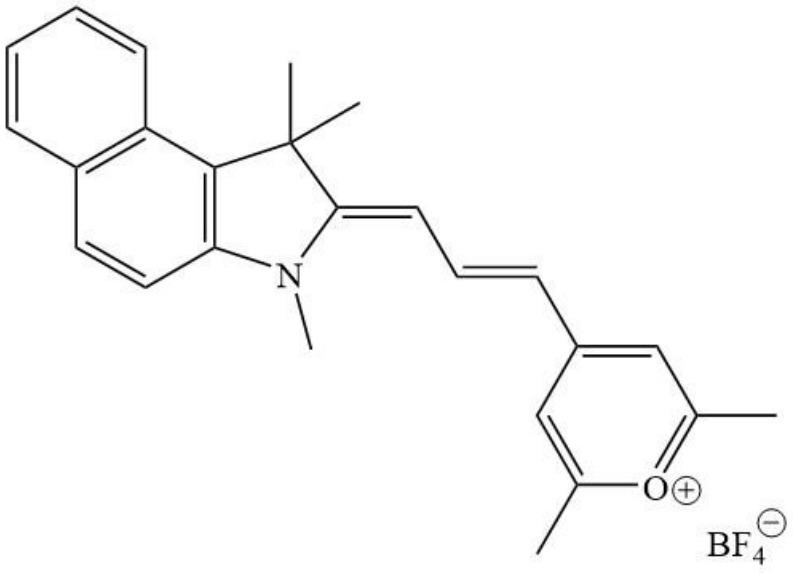

Figure 4-9 Structure of a) Chromeo P503 and b) Chromeo P540 (McNeil 2012)

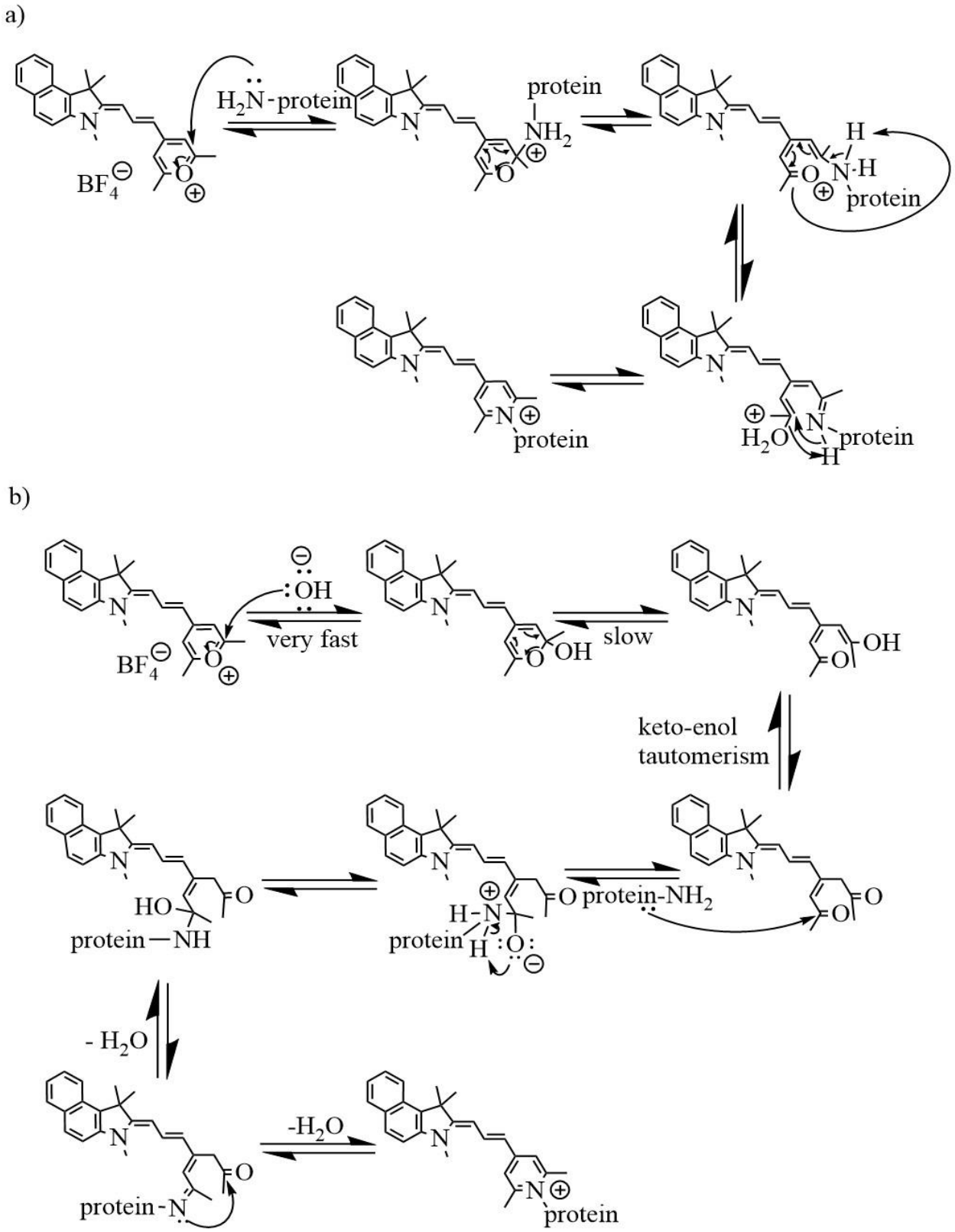

Figure 4-10 Two different labeling reaction mechanisms of Chromeo Py-dyes (McNeil 2012; Bayer & König, 2016)

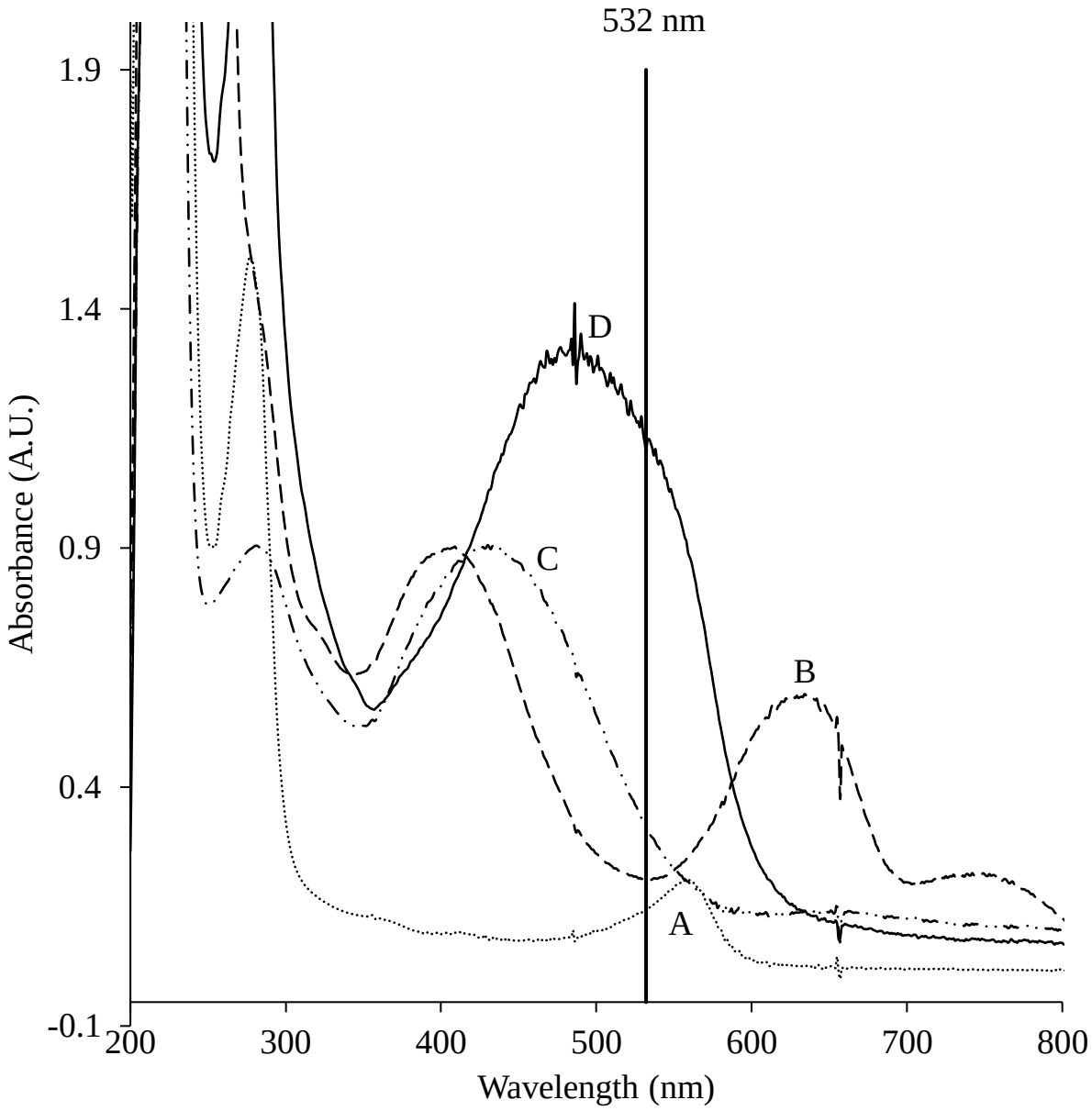

Figure 4-11 UV-visible absorption spectra of (A) 1600 U/mL CA 19-9 in 0.1M $NaHCO_3$, (B) 1.84 µL Chromeo P503 dissolved in DMF, (C) 1.84 µL Chromeo P503 in 0.1M $NaHCO_3$ and (D) 1600 U/mL Chromeo P503 conjugated-CA 19-9 in 0.1 M $NaHCO_3$.

label-protein ratio of 7:1 (within the manufacturer's recommended ratio range). The wavelength of maximum absorbance shifts from 612 nm to 503 nm upon covalently binding the protein, and hence, it undergoes a significant color change from blue to red, allowing an easy visual confirmation. The resulting product is stable for a month (Craig *et al*., 2005). Furthermore, its molar absorptivity is 24,000 M^{-1} cm^{-1} after conjugation with protein, and the wave-mixing detection sensitivity is excellent t since wave mixing is an absorption-based optical method. In addition, using Chromeo P503 as a label saves time since the labeling reaction time is short (30 minutes), and dialysis to remove excess dye is unnecessary when using a 532 nm laser as an excitation source. Chromeo P503 also degrades quickly due to ring-opening in a basic solution, and hence, excess-dye optical absorption is negligible at 532 (Bayer & König, 2016; Activemotif, n.d.-a).

The optimal molar ratio of Chromeo Py P503 to CA 19-9 is determined to minimize the excess Chromeo P503 and maximize the degree of labeling. Figure 4-12 shows UV-visible absorption spectra of Chromeo P503-conjugated CA 19-9 using various Chromeo P503 to CA 19-9 molar ratios and the corresponding amounts of Chromeo P503 without CA 19-9 dissolved in the same buffer. The net absorbance at 532 nm (absorbance of Chromeo P503-conjugated CA 19-9 minus absorbance of degraded Chromeo P503) increases steadily when the molar ratio is increased from 1:1 to 5:1. This increase significantly slows down when the molar ratio is increased from of 5:1 to 6:1. Hence, the ratio 5:1 is determined as the optimal molar ratio with the least amount of excess Chromeo P503 that could yield optical background.

Figure 4-13 compares the spectral features of Chromeo P540 label alone and Chromeo P540-labeled CA 19-9 using the ratio of 4:1 (within the manufacturer's recommended ratio range). The absorption maximum wavelength shifts from 587 nm to 533 nm upon covalently binding the

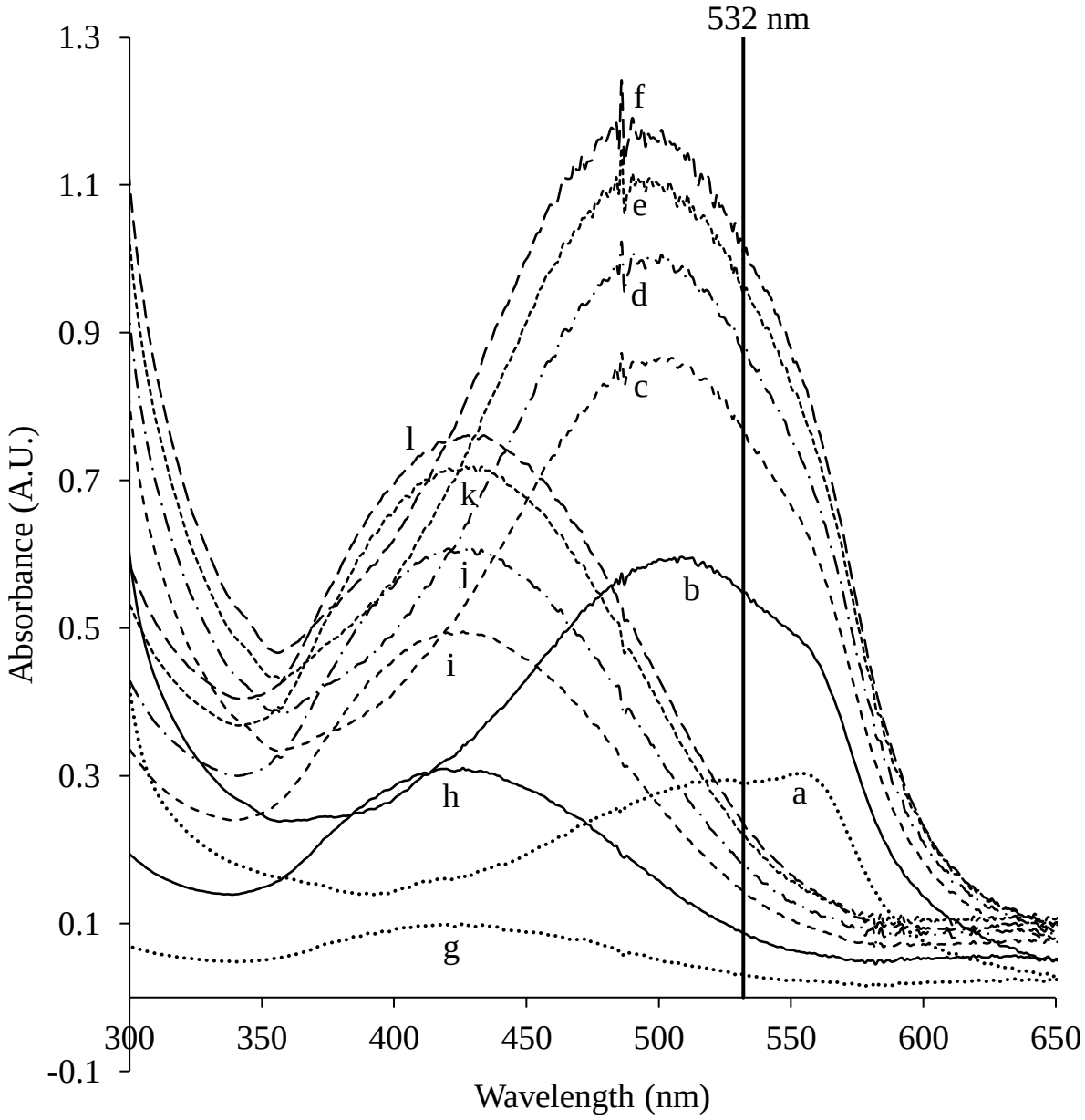

Figure 4-12 UV-visible absorption spectra of Chromeo P503-conjugated-CA 19-9 with various Chromeo P503 to CA 19-9 molar ratios of (a) 1:1, (b) 2:1, (c) 3:1, (d) 4:1, (e) 5:1 and (f) 6:1 in 500 µL of 0.1M $NaHCO_3$. Corresponding concentrations of Chromeo P503 without CA 19-9 are dissolved in 500 µL of 0.1M $NaHCO_3$ (g, h, i, j, k, and l).

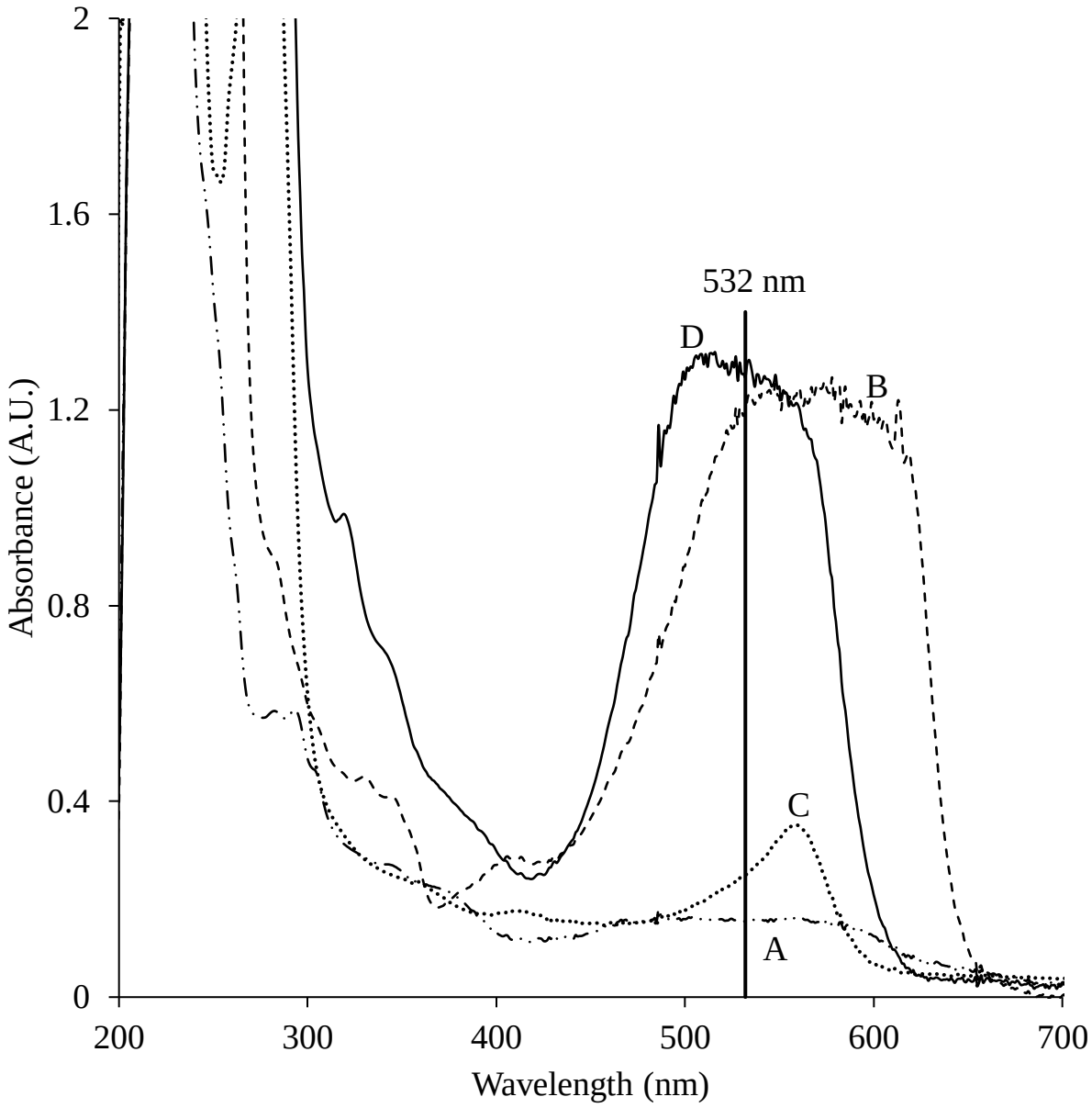

Figure 4-13 UV-visible absorption spectra of (A) 1600 U/mL CA 19-9 in 0.1M $NaHCO_3$, (B) 1.16 µL of stock Chromeo P540 dissolved in 0.1M $NaHCO_3$, (C) 1.16 µL of stock Chromeo P540 in 0.1M $NaHCO_3$ after heating at 55 ºC for 2 hours, and (D) 1600 U/mL Chromeo P540 conjugated-CA 19-9 in 0.1M $NaHCO_3$ after heating at 55 ºC for 2 hours.

protein. Hence, it undergoes a substantial color change (from purple to red), indicating the completion of the labeling reaction. Its molar absorptivity is 50,000 M^{-1} cm^{-1} after conjugation with the protein (Activemotif, n.d.-b), and it is higher than that of Chromeo P503-conjugated form (24,000 M^{-1} cm^{-1}). Additionally, its fluorescence quantum yield (20%) is lower than that of Chromeo P503 (50%). Hence, Chromeo P540-conjugated protein is expected to yield a better detection limit when using the same molar ratio for Chromeo Py and CA 19-9 (Vander Wal *et al*., 1992).

The excess Chromeo P540 label absorption at 532 nm is not negligible, and hence, dialysis is necessary to remove the excess Chromeo P540 label, or an extra step is needed to degrade Chromeo P540 in a basic solution to minimize background interference. Incubating Chromeo P540-conjugated protein at 55 °C for 2 hours in a basic solution significantly reduces optical absorption of any excess label at 532 nm, and it is faster than using dialysis (2 hours vs. 6 hours). We tested and confirmed that the optical absorption of degraded Chromeo P540 at 532 nm is much lower than that of Chromeo P540-conjugated CA 19-9 at 532 nm even when using an extremely high Chromeo P540 to CA 19-9 molar ratio of 1000:1.

A

Figure 4-14 shows UV-visible absorption spectra of Chromeo P540-conjugated CA 19-9 using various label-to-protein molar ratios in order to determine the optimal molar ratio for Chromeo P540 and CA 19-9. The absorbance increases at 532 nm and starts to level off between molar ratios of 2:1 and 4:1. Hence, the molar ratio of 2:1 is used to label CA 19-9 in order to minimize excess label when the extra heating step or dialysis is not performed.

The amino acid analysis of CA 19-9 indicates that this glycoprotein bears 42 lysine groups and one N-terminus on average (Klug *et al*. 1988), and hence, 43 labeling sites are available for conjugation with dyes. However, these labeling sites are not 100 % exposed or available for dye

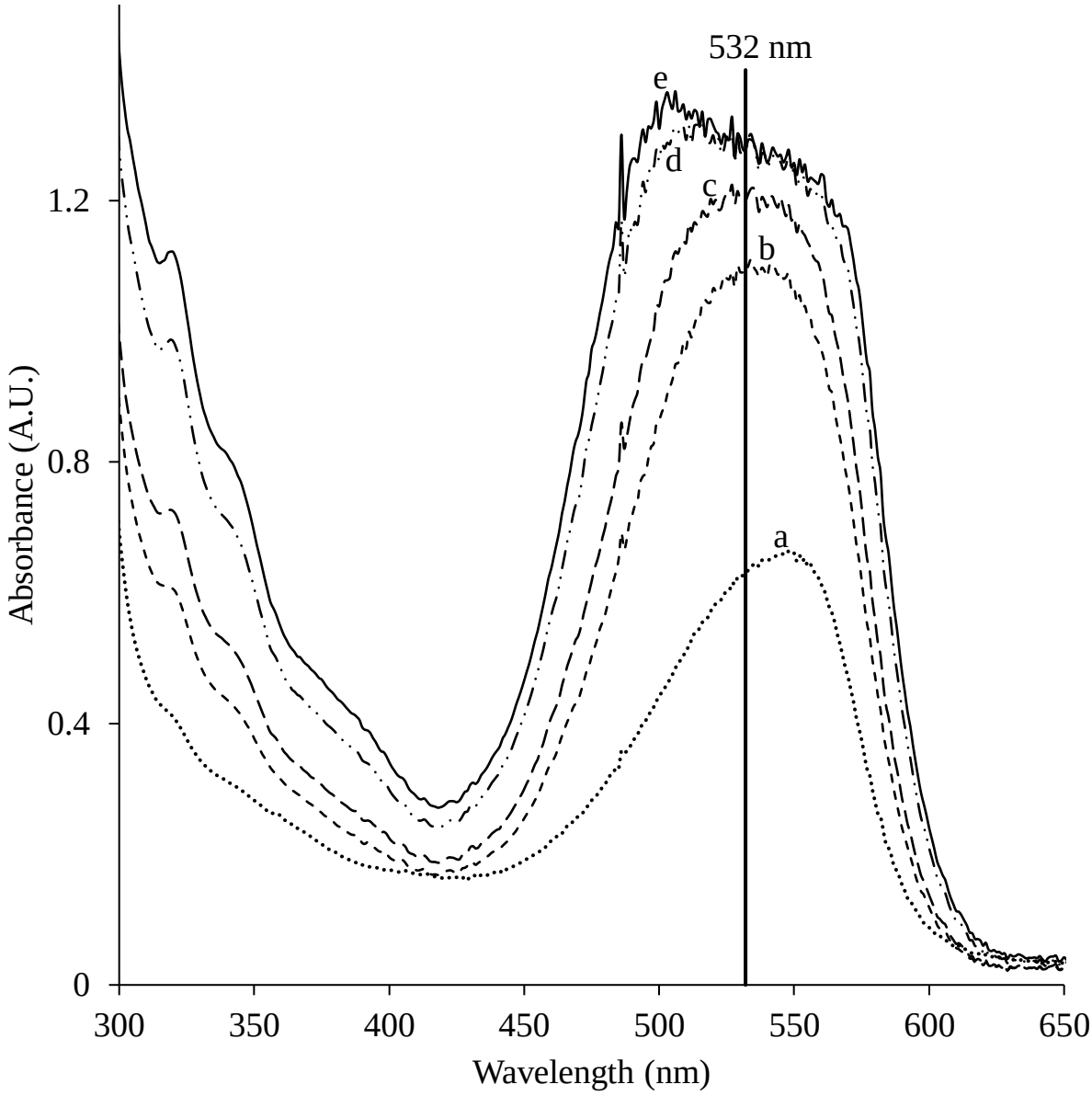

Figure 4-14 Absorption spectra of Chromeo P540 conjugated-CA 19-9 with various Chromeo P540 to CA 19-9 mole ratio of a) 1:1, b) 2:1, c) 3:1, d) 4:1 and e) 5:1.

conjugation because of abundant glycans and protein conformation. Using an optimal label-to-protein molar ratio and a suitable laser excitation wavelength (532 nm) offer better wave-mixing detection sensitivity levels.

Figure 4-15 shows the optical absorption of degraded Chromeo P540 at 532 nm is much lower than that of Chromeo P540-conjugated CA 19-9 at 532 nm even when using an extremely high Chromeo P540 to CA 19-9 molar ratio of 1000:1.

4.4.3 Confirmation of DFWM Signal Yielded from Chromeo P503-Conjugated CA 19-9

Low laser power is effectively used in the detection, taking advantage of the wave-mixing signal's cubic dependence on laser input power. The 450 U/mL CA 19-9 is detected using the following 473 nm laser input powers: 18.0 mW, 32.1 mW, 35.0 mW, 40.9 mW and 42.8 mW. Figure 4-16 shows a slope of 2.99 for our laser wave-mixing signals. A slope of 3.0 is expected for the power plot, as shown in Equation 4-1. For the concentration plot shown in Figure 4-17, we observe a slope of 1.99 for our laser wave-mixing signal over a range of analyte concentrations (56 U/mL, 128 U/ml, 256 U/mL, 450 U/mL, and 903 U/mL) using a 473 nm laser input power level of 38.5 mW. A slope of 2.0 is expected for the concentration plot, as shown in Equation 1. Our power-plot slope (2.99) and concentration-plot slope (1.99) are close to those theoretical values. They confirm that a nonlinear laser wave-mixing optical setup is properly aligned and optimized with a minimum background noise level.

4.4.4 Nanomolar Detection of Chromeo P503 conjugated CA 19-9 and Picomolar Detection of Chromeo P540 Conjugated CA 19-9

Figure 4-18 shows a CE-based wave-mixing detector yielding a concentration detection

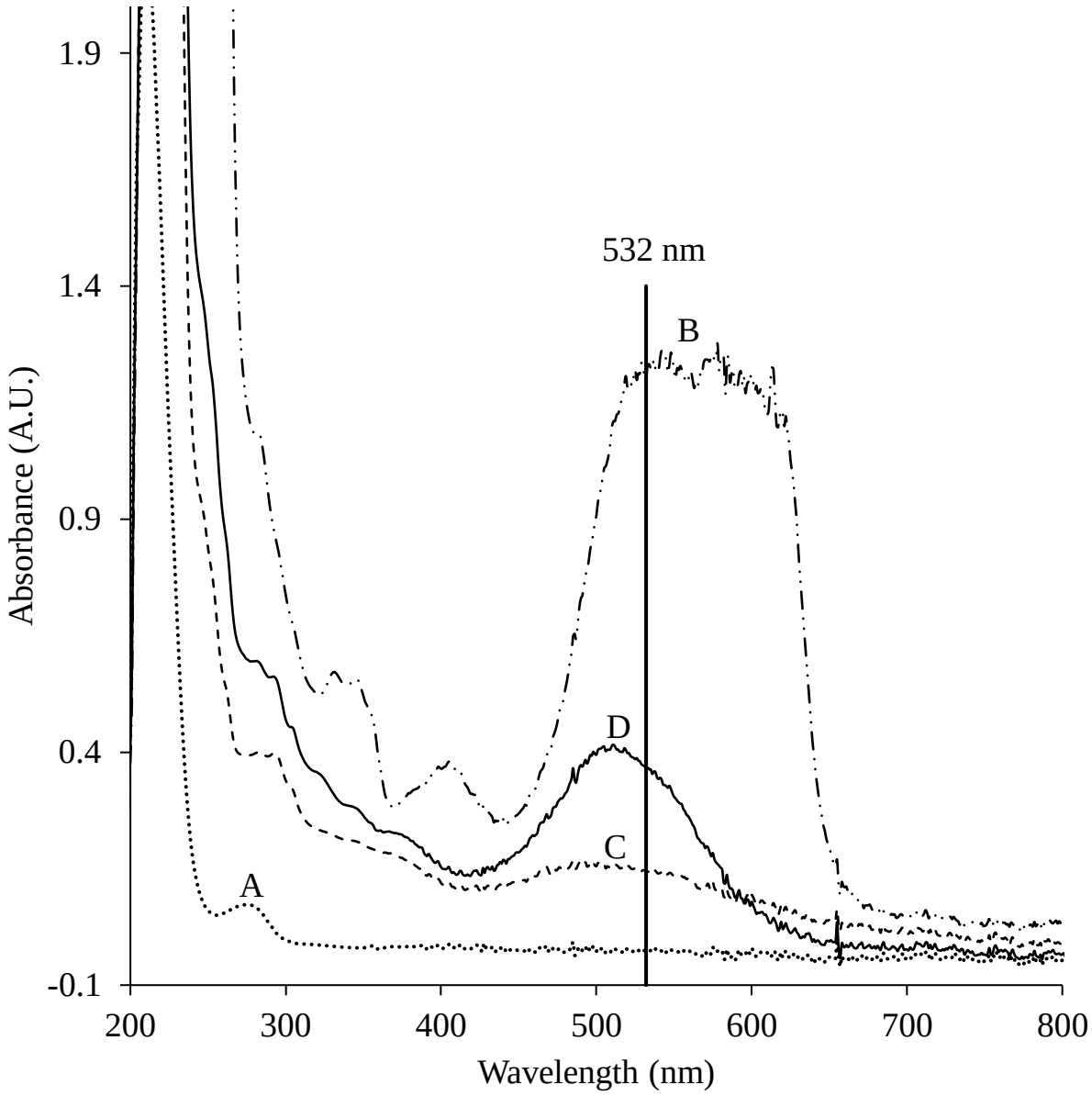

Figure 4-15 UV-visible absorption spectra of A) 9U/mL CA 19-9 is in 0.1M $NaHCO_3$, B) 0.1 μL Chromeo P540 dissolved in 300 μL DMF, C) 0.1 μL Chromeo P540 in 300 μL 0.1M $NaHCO_3$ after heated at 55ºC for 2 hours and D) 9 U/mL Chromeo P540 conjugated-CA 19-9 in 0.1M $NaHCO_3$ after heated at 55ºC for 2 hours.

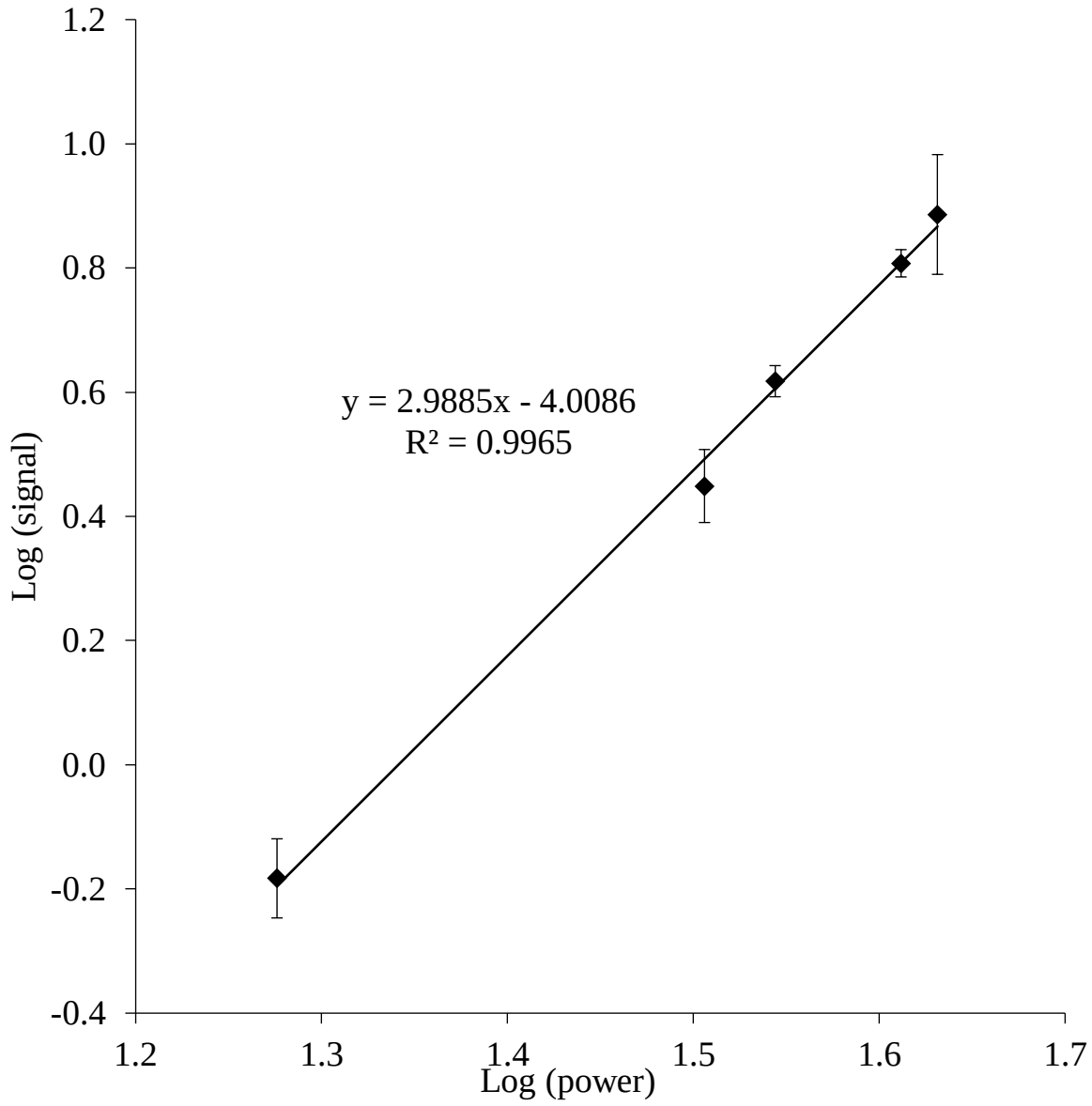

Figure 4-16 Cubic dependence of nonlinear wave-mixing signal of 450 U/mL CA 19-9 on input laser power.

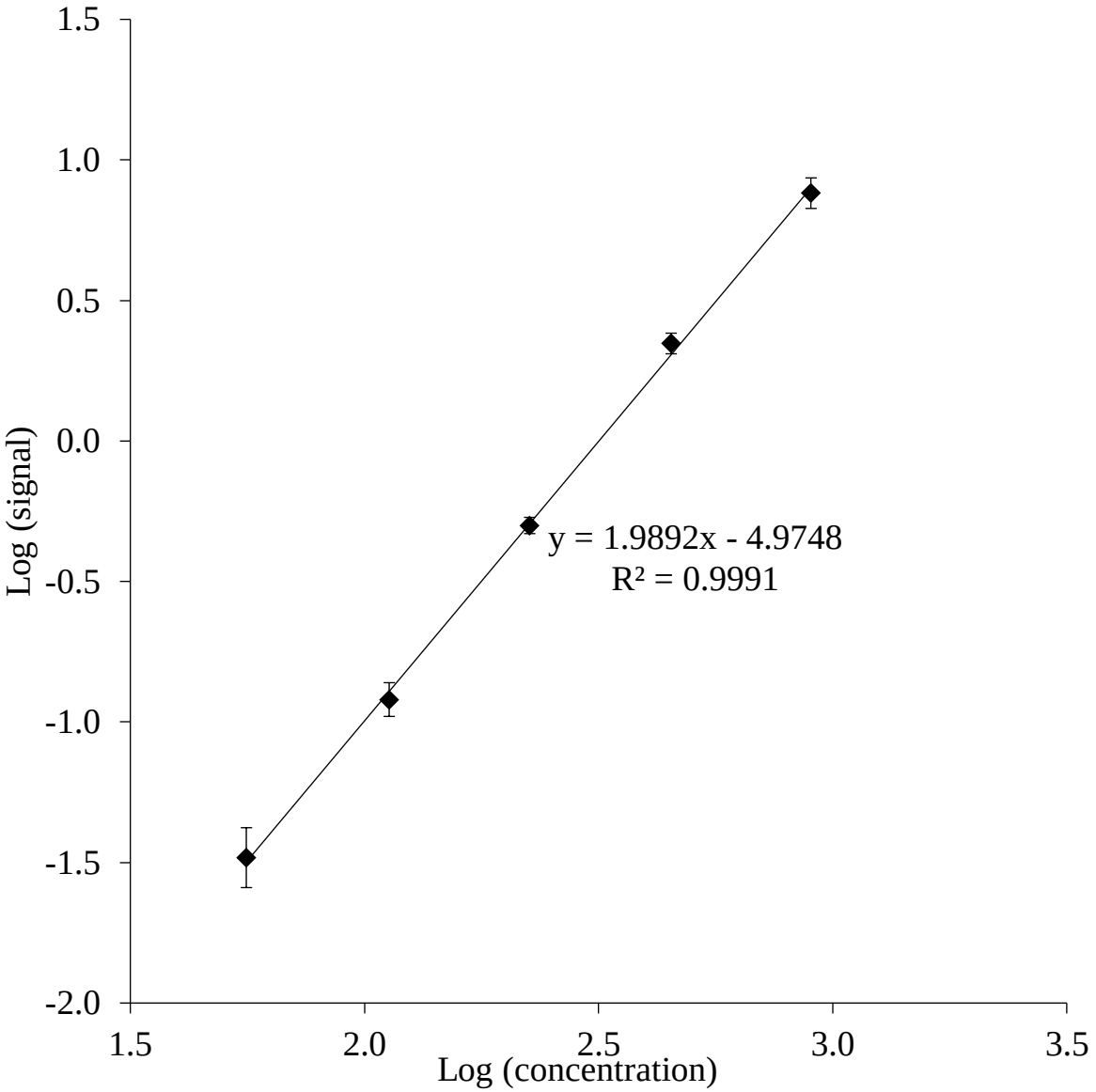

Figure 4-17 Quadratic dependence of the nonlinear wave-mixing signal on CA 19-9 concentration spanning from 56U/mL to 903 U/mL.

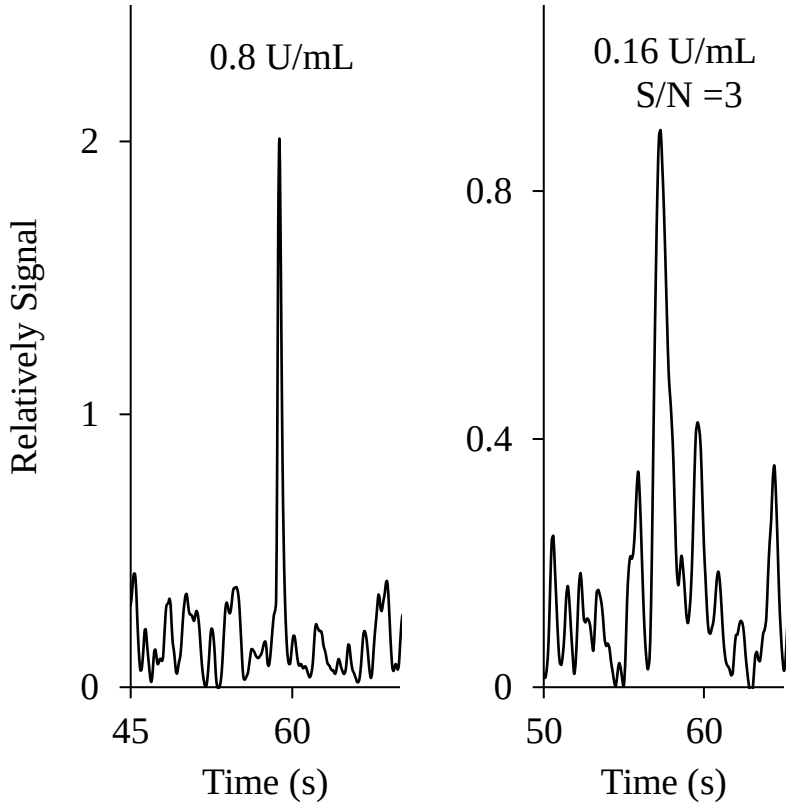

Figure 4-18 Electropherograms of Chromeo P540-conjugated CA 19-9 at concentrations of 8 U/mL and 0.8 U/mL. The Capillary (75 μm i.d., 40 cm total, 20 cm effective length) is rinsed with NaOH (0.1 M), water, UltraTrol LN, and background electrolyte (20 mM borate, pH 9.0) for 2 minutes. The sample is injected electrokinetically at -10 kV for 20 s, and -18 kV is applied for each run.

limit of 0.16 U/mL (1.3 nM) for Chromeo P503-conjugated CA 19-9 using a 5:1 molar ratio. The corresponding mass detection limit is determined as 98 zeptomole based on the estimated laser probe volume of 75 pL used in our wave-mixing setup (~59,000 molecules inside the probe volume).

Figure 4-19 shows a CE-based wave-mixing detector yielding a concentration detection limit of 0.8 U/mL (6.7 nM) for Chromeo P540-conjugated CA 19-9 using a 2:1 molar ratio. The corresponding mass detection limit is determined as 0.50 attomole based on the estimated laser probe volume of 75 pL used in our wave-mixing setup (~300,000 molecules inside the probe volume).

With a high Chromeo P540 to CA 19-9 molar ratio (1000: 1) and efficient degradation of free Chromeo P540, the best CA 19-9 concentration detection limit achieved is 75 pM (Figure 4-20). The mass detection limit is 5.6 zeptomole based on the small probe volume (75 pL) used in our wave-mixing setup (~ 3000 molecules inside the probe volume are detected).

4.4.5 Enhanced Detection Selectivity using Capillary Gel Electrophoresis

Capillary gel electrophoresis (CGE) separates proteins based on the difference in their molecular size. Cytochrome c is a heme protein containing a polypeptide chain and a heme group, and it is essential for cellular oxidation in animals (Sigma-Aldrich, n.d.). The maximum absorption wavelength of cytochrome c is 550 nm (Petersen & Andréasson, 1976). Hence, label-free absorption detection can be achieved by using a 532 nm laser. The working principle of capillary gel electrophoresis is the same as sodium dodecyl sulfate-polyacrylamide gel electrophoresis (SDS-PAGE), where SDS denatures the sample and yields the proteins at a similar charge-to-mass ratio. The voltage applied migrates the denatured negatively charged proteins to

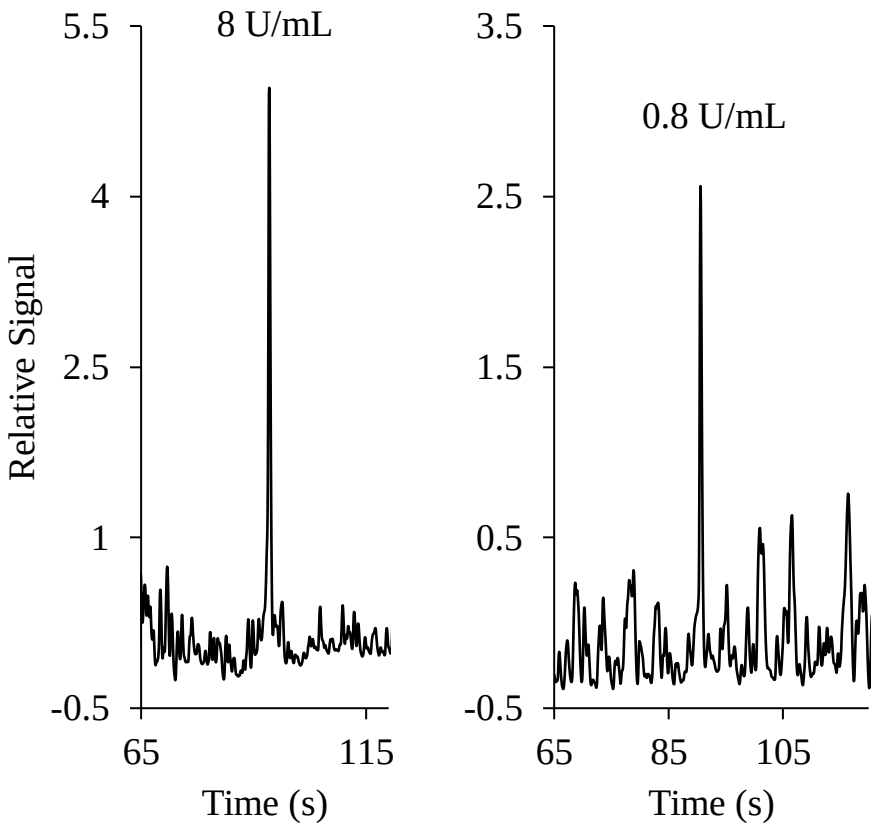

Figure 4-19 Electropherograms of Chromeo P503-conjugated CA 19-9 (0.8 U/mL and 0.16 U/mL). The capillary (75 μm i.d., 30 cm total, 15 cm effective length) is rinsed with NaOH (0.1 M), water, UltraTrol LN, and background electrolyte (20 mM borate, pH 9.0) for 2 minutes. The sample is injected electrokinetically at -10 kV for 20 s, and -18 kV is applied for each run.

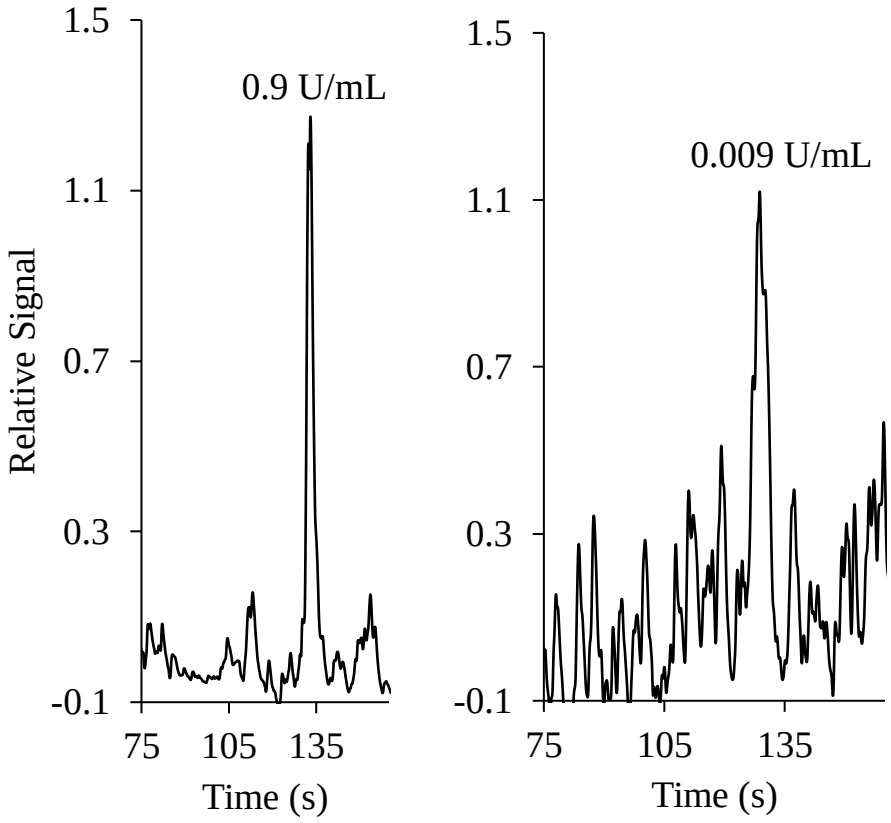

Figure 4-20 Electropherograms of Chromeo P540-conjugated CA 19-9 (0.9 U/mL, and 0.009 U/mL). Capillary: 75 μm i.d., 40 cm (25 cm effective length). Capillary is rinsed with NaOH (0.1 M), water, UltraTrol LN, and background electrolyte (20 mM borate, pH 9.0) for 2 minutes, respectively. The sample is injected electrokinetically at -10 kV for 20 s and 25s. -18 kV is applied for each run.

positively charged anode with different migration rates (Manns, 2011).

Figure 4-21 shows electropherograms of (1) cytochrome c, (2) CA 19-9, and (3) a mixture of cytochrome c and CA 19-9 detected by laser wave mixing using a 532 nm laser. The molecular mass of cytochrome c is 12,327 Da (Nakashima *et al*., 1966), much smaller than that of CA 19-9. Hence, the CE peak of cytochrome c appears before that of CA 19-9. The sample was prepared by denaturing the mixture of cytochrome c and labeled CA 19-9. Differences in the complexation of protein molecules with SDS during denaturation can cause peak broadening (Guttman, 1996), and a sieving matrix with a larger molecular weight or at a larger concentration is more suitable for resolving larger molecules like CA 19-9 (Yamaguchi *et al*., 2015). Although increasing the concentration of PEO or using PEO with a larger molecular mass can enhance resolution, it is harder to form a uniform matrix in the capillary and maintain the current level when voltage is applied.

4.5 Conclusion

Laser wave-mixing detection offers ultrasensitive detection limits of glycoprotein biomarker (CA 19-9) for pancreatic cancer. Chromeo P540-conjugated protein provides the best detection limit at 0.009 U/mL by incubating the excessive labeling reaction mixture at 55°C for two hours, which significantly reduces the absorbance of free Chromeo P540 at 532 nm. In addition, the signal is a coherent beam that can be collected with high efficiency. Laser wave-mixing detection offers better mass detection limits than commercially available methods, including CLIA and ECLIA. Using wave mixing, a wide range of proteins can be separated and detected simultaneously, and it is more convenient and faster than other detection methods. Potential applications include sensitive and rapid detection of CA 19-9 for early diagnosis of

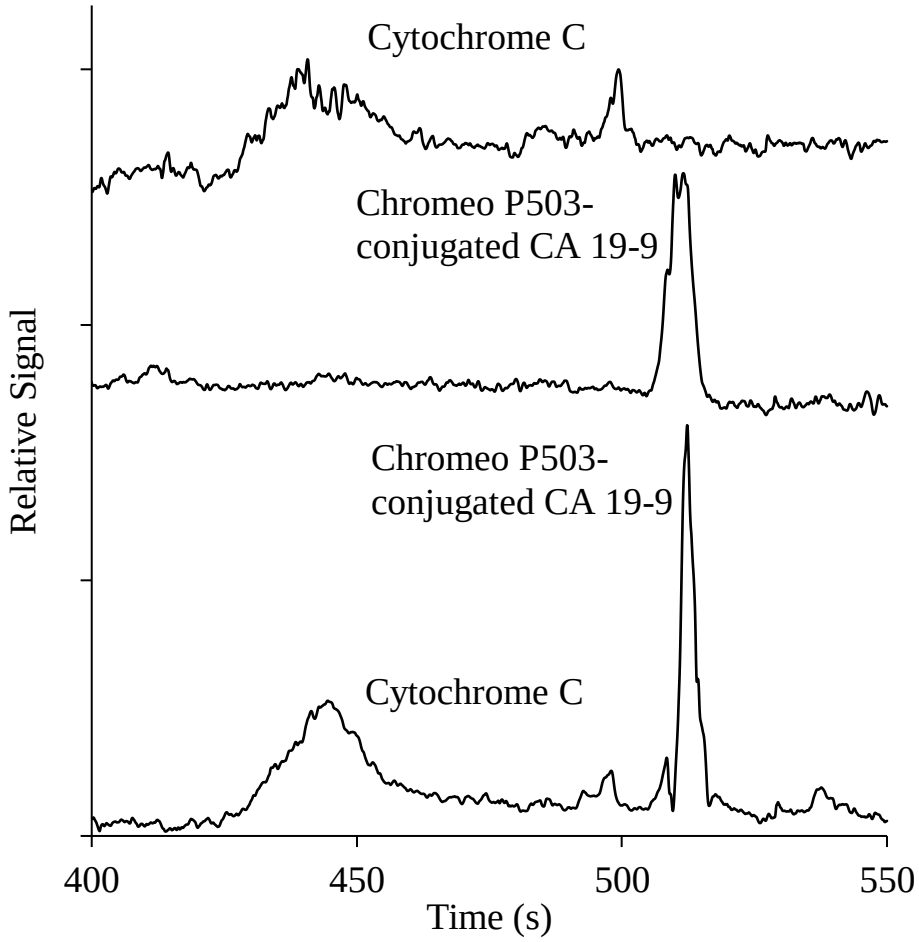

Figure 4-21 Electropherograms of cytochrome c (top), CA 19-9 (middle), and a mixture of cytochrome c and CA 19-9 (bottom) detected by laser wave mixing using a 532 nm laser, and 500 U/mL CA 19-9, 0.32 mM cytochrome c, and their mixture (1:1 volume ratio) are in a sample buffer with 25 mM Tris-CHES, pH 9.0, 2% SDS. The capillary (75 µm i.d., 45 cm total, 30 cm effective) is rinsed with NaOH (0.1 M), water, UltraTrol LN, and sieving matrix (100 mM Tris-CHES, pH 9.0, 0.1% SDS, 2% PEO 100,000) for 2 minutes. The sample is injected electrokinetically for 8 s, and -10 kV is applied for each run.

pancreatic cancer using just a few drops of samples. Our solid-state laser-based wave-mixing detector is compact and portable, and suitable for field use.

4.6 Acknowledgements

A part of the material for this chapter comes from a manuscript entitled "Sensitive multi-photon nonlinear laser wave-mixing detection of cancer and heart failure biomarkers," by Jie Liang, James Suprapto, Samantha Crawford, William G. Tong, published in Proc. SPIE 11105, Novel Optical Systems, Methods, and Applications XXII, 111050N., 2019. The dissertation author is the first author of this manuscript.

We acknowledge partial support of this work by the U.S. Dept. of Homeland Security Science and Technology Directorate, the U.S. Dept. of Defense, the Army Research Office, the NSF, the NIH (R01), and the NIH IMSD (2R25GM058906).

4.7 References

Abbott. (n.d.). *ARCHITECT i2000SR Immunoassay*. https://www.corelaboratory.abbott/us/en/offerings/brands/architect/architect-i2000SR

Activemotif. (n.d.-a). *Chromeo™ P503*. https://www.activemotif.com/documents/1641.pdf

Activemotif. (n.d.-b). *Chromeo™P540*. https://www.activemotif.com/documents/1642.pdf

Alarfaj, N., El-Tohamy, M., & Oraby, H. (2018). CA 19–9 Pancreatic Tumor Marker Fluorescence Immunosensing Detection via Immobilized Carbon Quantum Dots Conjugated Gold Nanocomposite. *International Journal of Molecular Sciences*, *19*(4), 1162. https://doi.org/10.3390/ijms19041162

American Cancer Society. (2022). *Cancer Facts & Figures 2022* (No. 500822). https://www.cancer.org/content/dam/cancer-org/research/cancer-facts-and-statistics/annual-cancer-facts-and-figures/2022/2022-cancer-facts-and-figures.pdf

American Society of Clinical Oncology. (2022, January 6). *Pancreatic Cancer - Stages*. Cancer.Net. https://www.cancer.net/cancer-types/pancreatic-cancer/stages

ANOVA. (n.d.). *CA19-9 (Human) CLIA Kit*. http://www.abnova.com/protocol_pdf/KA2812.pdf

Ballehaninna, U. K., & Chamberlain, R. S. (2013). Biomarkers for pancreatic cancer: promising new markers and options beyond CA 19–9. *Tumor Biology*, *34*(6), 3279–3292. https://doi.org/10.1007/s13277-013-1033-3

Bayer, M., & König, S. (2016). Pyrylium-based dye and charge tagging in proteomics. *ELECTROPHORESIS*, *37*(22), 2953–2958. https://doi.org/10.1002/elps.201600318

Beckman Coulter. (2015, June). *Unicel DxI - Access Immunoassay System*. Slideshare. https://www.slideshare.net/RolandoAlgarin/unicel-dxi-manual-de-operador-ingles

Berniolles, S., Wu, Z., & Tong, W. G. (1994). Diode laser-based nonlinear degenerate four-wave mixing analytical spectrometry. *Spectrochimica Acta Part B: Atomic Spectroscopy*, *49*(12–14), 1473–1481. https://doi.org/10.1016/0584-8547(94)80123-1

Bio-Rad Laboratories. (2019). *Critical Raw Materials - Cell Culture Derived Antigens and Antibodies*.

Centers for Disease Control and Prevention. (2022). *An Update on Cancer Deaths in the United States*. US Department of Health and Human Services, Centers for Disease Control and Prevention, Division of Cancer Prevention and Control. https://www.cdc.gov/cancer/dcpc/research/update-on-cancer-deaths/index.htm

Craig, D. B., Wetzl, B. K., Duerkop, A., & Wolfbeis, O. S. (2005). Determination of picomolar concentrations of proteins using novel amino reactive chameleon labels and capillary electrophoresis laser-induced fluorescence detection. *ELECTROPHORESIS*, *26*(11), 2208–2213. https://doi.org/10.1002/elps.200410332

Del Villano, B. C., Brennan, S., Brock, P., Bucher, C., Liu, V., McClure, M., Rake, B., Space, S., Westrick, B., Schoemaker, H., & Zurawski, V. R. (1983). Radioimmunometric assay for a monoclonal antibody-defined tumor marker, CA 19–9. *Clinical Chemistry*, *29*(3), 549–552. https://doi.org/10.1093/clinchem/29.3.549

Du, D., Xu, X., Wang, S., & Zhang, A. (2007). Reagentless amperometric carbohydrate antigen 19–9 immunosensor based on direct electrochemistry of immobilized horseradish peroxidase. *Talanta*, *71*(3), 1257–1262. https://doi.org/10.1016/j.talanta.2006.06.028

Du, D., Yan, F., Liu, S., & Ju, H. (2003). Immunological assay for carbohydrate antigen 19–9 using an electrochemical immunosensor and antigen immobilization in titania sol-gel matrix. *Journal of Immunological Methods*, *283*(1–2), 67–75. https://doi.org/10.1016/j.jim.2003.08.014

Duffy, M. J. (1998). CA 19–9 as a Marker for Gastrointestinal Cancers: A Review. *Annals of Clinical Biochemistry: International Journal of Laboratory Medicine*, *35*(3), 364–370. https://doi.org/10.1177/000456329803500304

Gee, C. T., Kehoe, E., Pomerantz, W. C. K., & Penn, R. L. (2017). Quantifying Protein Concentrations Using Smartphone Colorimetry: A New Method for an Established Test. *Journal of Chemical Education*, *94*(7), 941–945. https://doi.org/10.1021/acs.jchemed.6b00676

Gu, B., Xu, C., Yang, C., Liu, S., & Wang, M. (2011). ZnO quantum dot labeled immunosensor for carbohydrate antigen 19–9. *Biosensors and Bioelectronics*, *26*(5), 2720–2723. https://doi.org/10.1016/j.bios.2010.09.031

Guttman, A. (1996). Capillary sodium dodecyl sulfate-gel electrophoresis of proteins. *Electrophoresis*, *17*(8), 1333–1341. https://doi.org/10.1002/elps.1150170810

Hu, F., Chen, S., & Yuan, R. (2013). Application of magnetic core–shell microspheres on reagentless immunosensor based on direct electrochemistry of glucose oxidase for detection of carbohydrate antigen 19–9. *Sensors and Actuators B: Chemical*, *176*, 713–722. https://doi.org/10.1016/j.snb.2012.08.072

Huang, C., Yang, Q., Song, F., Chen, N., Yao, B., Liao, X., Zhang, S., Chen, Y., & Jin, G. (2016). Label-free multiplex immunoassay of AFP, CEA and CA19-9 by integrated microfluidic biosensor based on imaging ellipsometry. *Integrated Ferroelectrics*, *171*(1), 59–69. https://doi.org/10.1080/10584587.2016.1171664

Huang, T., Long, M., & Huo, B. (2010). Competitive Binding to Cuprous Ions of Protein and BCA in the Bicinchoninic Acid Protein Assay. *The open biomedical engineering journal*, *4*, 271–278. https://doi.org/10.2174/1874120701004010271

Jawad, Z. A. R., Theodorou, I. G., Jiao, L. R., & Xie, F. (2017). Highly Sensitive Plasmonic Detection of the Pancreatic Cancer Biomarker CA 19–9. *Scientific Reports*, *7*(1). https://doi.org/10.1038/s41598-017-14688-z

Klug, T. L., LeDonne, N. C., Greber, T. F., & Zurawski, V. R., Jr (1988). Purification and composition of a novel gastrointestinal tumor-associated glycoprotein expressing sialylated lacto-N-fucopentaose II (CA 19-9). *Cancer research*, *48*(6), 1505–1511.

Ko, J., & Lim, H. B. (2014). Multicore Magnetic Nanoparticles (MMNPs) Doped with Cs and FITC for the Determination of Biomarker in Serum using ICP-MS. *Analytical Chemistry*, *86*(9), 4140–4144. https://doi.org/10.1021/ac4036668

La'ulu, S. L., & Roberts, W. L. (2007). Performance Characteristics of Five Automated CA 19–9 Assays. *American Journal of Clinical Pathology*, *127*(3), 436–440. https://doi.org/10.1309/h52vet3m6p7gywg1

Leng, Y., Wu, W., Li, L., Lin, K., Sun, K., Chen, X., & Li, W. (2016). Magnetic/Fluorescent Barcodes Based on Cadmium-Free Near-Infrared-Emitting Quantum Dots for Multiplexed Detection. *Advanced Functional Materials*, *26*(42), 7581–7589. https://doi.org/10.1002/adfm.201602900

Lin, J., Yan, F., Hu, X., & Ju, H. (2004). Chemiluminescent immunosensor for CA19-9 based on antigen immobilization on a cross-linked chitosan membrane. *Journal of Immunological Methods*, *291*(1–2), 165–174. https://doi.org/10.1016/j.jim.2004.06.001

Manns, J. M. (2011). SDS-Polyacrylamide Gel Electrophoresis (SDS-PAGE) of Proteins. *Current Protocols in Microbiology*, *22*(1). https://doi.org/10.1002/9780471729259.mca03ms22

McNeil, H., Macnamara, K. G. (2012). Pre-staining Protocol for a Protein Sample with Pyrylim Dye and Respective Kit (U.S. patent No. 8,303,790 B2). U.S. Patent and Trademark Office. https://patft.uspto.gov/netacgi/nph-Parser?Sect1=PTO2&Sect2=HITOFF&p=1&u=%2Fnetahtml%2FPTO%2Fsearch-bool.html&r=1&f=G&l=50&co1=AND&d=PTXT&s1=8,303,790.PN.&OS=PN/8,303,790&RS=PN/8,303,790

MyBioSource. (n.d.). *CA 19–9 native protein*. https://www.mybiosource.com/native-protein/ca-19-9/537854

Nakashima, T., Higa, H., Matsubara, H., Benson, A. M., & Yasunobu, K. T. (1966). The Amino Acid Sequence of Bovine Heart Cytochrome *c*. *Journal of Biological Chemistry*, *241*(5), 1166–1177. https://doi.org/10.1016/s0021-9258(18)96817-1

Petersen, L. C., & Andréasson, L. E. (1976). The reaction between oxidized cytochrome *c* and reduced cytochrome*c*oxidase. *FEBS Letters*, *66*(1), 52–57. https://doi.org/10.1016/0014-5793(76)80583-2

Poruk, K. E., Firpo, M. A., Adler, D. G., & Mulvihill, S. J. (2013). Screening for Pancreatic Cancer. *Annals of Surgery*, *257*(1), 17–26. https://doi.org/10.1097/sla.0b013e31825ffbfb

Rahib, L., Smith, B. D., Aizenberg, R., Rosenzweig, A. B., Fleshman, J. M., & Matrisian, L. M. (2014). Projecting Cancer Incidence and Deaths to 2030: The Unexpected Burden of Thyroid, Liver, and Pancreas Cancers in the United States. *Cancer Research*, *74*(11), 2913–2921. https://doi.org/10.1158/0008-5472.can-14-0155

Richter, M. M. (2004). Electrochemiluminescence (ECL). *Chemical Reviews*, *104*(6), 3003–3036. https://doi.org/10.1021/cr020373d

Roche Diagnostics. (2017). *Elecsys CA 19–9*. https://labogids.sintmaria.be/sites/default/files/files/ca_19-9_2018-07_v23.pdf

Scarà, S., Bottoni, P., & Scatena, R. (2015). CA 19–9: Biochemical and Clinical Aspects. *Advances in Cancer Biomarkers*, 247–260. https://doi.org/10.1007/978-94-017-7215-0_15

Sha, Y., Guo, Z., Chen, B., Wang, S., Ge, G., Qiu, B., & Jiang, X. (2015). A one-step electrochemiluminescence immunosensor preparation for ultrasensitive detection of carbohydrate antigen 19–9 based on multi-functionalized graphene oxide. *Biosensors and Bioelectronics*, *66*, 468–473. https://doi.org/10.1016/j.bios.2014.12.013

Sherovski, P., Stojković, G., & Ristovska, N. (2018). Development, validation and application of first derivative spectroscopy ratio method for estimation of Bradford assay. *Analytical Biochemistry*, *558*, 35–40. https://doi.org/10.1016/j.ab.2018.07.027

Shi, M., Zhao, S., Huang, Y., Zhao, L., & Liu, Y. M. (2014). Signal amplification in capillary electrophoresis based chemiluminescent immunoassays by using an antibody–gold nanoparticle–DNAzyme assembly. *Talanta*, *124*, 14–20. https://doi.org/10.1016/j.talanta.2014.02.032

Siegel, R. L., Miller, K. D., Fuchs, H. E., & Jemal, A. (2021). Cancer Statistics, 2021. *CA: A Cancer Journal for Clinicians*, *71*(1), 7–33. https://doi.org/10.3322/caac.21654

Siemens Healthineers. (n.d.). *ADVIA Centaur XP Immunoassay System*. https://www.siemens-healthineers.com/en-us/immunoassay/systems/advia-centaur-xp

Siemens Medical Solutions Diagnostics. (2007, February). *IMMULITE® 2000/2500 Operator's Manual*. http://sky2.ch/Doc/I2500.pdf

Sigma-Aldrich. (n.d.-a). *Bradford Reagent*. https://www.sigmaaldrich.com/deepweb/assets/sigmaaldrich/product/documents/384/034/b6916bul.pdf

Sigma-Aldrich. (n.d.-b). *Cytochrome c from bovine heart*. https://www.sigmaaldrich.com/deepweb/assets/sigmaaldrich/product/documents/304/588/c3131pis.pdf

Sirohi, R. S. (2017). *Introduction to Optical Metrology*. Amsterdam University Press.

Smith, P., Krohn, R., Hermanson, G., Mallia, A., Gartner, F., Provenzano, M., Fujimoto, E., Goeke, N., Olson, B., & Klenk, D. (1985). Measurement of protein using bicinchoninic acid. *Analytical Biochemistry*, *150*(1), 76–85. https://doi.org/10.1016/0003-2697(85)90442-7

Song, J., Sokoll, L. J., Chan, D. W., & Zhang, Z. (2021). Validation of Serum Biomarkers That Complement CA19-9 in Detecting Early Pancreatic Cancer Using Electrochemiluminescent-Based Multiplex Immunoassays. *Biomedicines*, *9*(12), 1897. https://doi.org/10.3390/biomedicines9121897

Sun, A. L., & Qi, Q. A. (2016). Silver-functionalized g-C3N4 nanohybrids as signal-transduction tags for electrochemical immunoassay of human carbohydrate antigen 19–9. *The Analyst*, *141*(14), 4366–4372. https://doi.org/10.1039/c6an00696e

Tang, C. C., von Ah, D., & Fulton, J. S. (2018). The Symptom Experience of Patients With Advanced Pancreatic Cancer. *Cancer Nursing*, *41*(1), 33–44. https://doi.org/10.1097/ncc.0000000000000463

Tang, D., Hou, L., Niessner, R., Xu, M., Gao, Z., & Knopp, D. (2013). Multiplexed electrochemical immunoassay of biomarkers using metal sulfide quantum dot nanolabels and trifunctionalized magnetic beads. *Biosensors and Bioelectronics*, *46*, 37–43. https://doi.org/10.1016/j.bios.2013.02.027

Thermo Fisher Scientific. (2009, March). *NanoDrop 2000/2000c Spectrophotometer V1.0 User Manual*. https://assets.thermofisher.com/TFS-Assets/CAD/manuals/NanoDrop-2000-User-Manual-EN.pdf

Thermo Fisher Scientific. (2021, November 22). *Human CA19-9 ELISA Kit*. https://www.thermofisher.com/document-connect/document-connect.html?url=https://assets.thermofisher.com/TFS-Assets%2FLSG%2Fmanuals%2FEHCA199.pdf

Vander Wal, R., Holmes, B., Jeffries, J., Danehy, P., Farrow, R., & Rakestraw, D. (1992). Detection of HF using infrared degenerate four-wave mixing. *Chemical Physics Letters*, *191*(3–4), 251–258. https://doi.org/10.1016/0009-2614(92)85296-m

Wiechelman, K. J., Braun, R. D., & Fitzpatrick, J. D. (1988). Investigation of the bicinchoninic acid protein assay: Identification of the groups responsible for color formation. *Analytical Biochemistry*, *175*(1), 231–237. https://doi.org/10.1016/0003-2697(88)90383-1

Winter, J. M., Yeo, C. J., & Brody, J. R. (2012). Diagnostic, prognostic, and predictive biomarkers in pancreatic cancer. *Journal of Surgical Oncology*, *107*(1), 15–22. https://doi.org/10.1002/jso.23192

Yamaguchi, Y., Li, Z., Zhu, X., Liu, C., Zhang, D., & Dou, X. (2015). Polyethylene Oxide (PEO) and Polyethylene Glycol (PEG) Polymer Sieving Matrix for RNA Capillary Electrophoresis. *PLOS ONE*, *10*(5), e0123406. https://doi.org/10.1371/journal.pone.0123406

Yang, F., Yang, Z., Zhuo, Y., Chai, Y., & Yuan, R. (2015). Ultrasensitive electrochemical immunosensor for carbohydrate antigen 19–9 using Au/porous graphene nanocomposites as platform and Au@Pd core/shell bimetallic functionalized graphene nanocomposites as signal enhancers. *Biosensors and Bioelectronics*, *66*, 356–362. https://doi.org/10.1016/j.bios.2014.10.066

Zhang, A., Xiang, H., Zhang, X., Guo, W., Yuan, E., Huang, C., & Jia, N. (2016). A novel sandwich electrochemiluminescence immunosensor for ultrasensitive detection of carbohydrate antigen 19–9 based on immobilizing luminol on Ag@BSA core/shell microspheres. *Biosensors and Bioelectronics*, *75*, 206–212. https://doi.org/10.1016/j.bios.2015.08.047

Zhang, Y., Yang, J., Li, H., Wu, Y., Zhang, H., & Chen, W. (2015). Tumor markers CA19-9, CA242 and CEA in the diagnosis of pancreatic cancer: a meta-analysis. *International journal of clinical and experimental medicine*, *8*(7), 11683–11691.

Zhou, L., Zhou, J., Feng, Z., Wang, F., Xie, S., & Bu, S. (2016). Immunoassay for tumor markers in human serum based on Si nanoparticles and SiC@Ag SERS-active substrate. *The Analyst*, *141*(8), 2534–2541. https://doi.org/10.1039/c6an00003g

Zhu, H., Fan, G. C., Abdel-Halim, E., Zhang, J. R., & Zhu, J. J. (2016). Ultrasensitive photoelectrochemical immunoassay for CA19-9 detection based on CdSe@ZnS quantum dots sensitized TiO 2 NWs/Au hybrid structure amplified by quenching effect of Ab 2 @V 2+ conjugates. *Biosensors and Bioelectronics*, *77*, 339–346. https://doi.org/10.1016/j.bios.2015.09.051

CHAPTER 5

SENSITIVE DETECTION OF SURFACE-MOUNTED OR THIN BIOMARKERS USING LASER WAVE-MIXING SPECTROSCOPY

5.1 Abstract

Degenerate four-wave mixing (DFWM) is presented as a detector for biomarkers for the early detection and diagnosis of cancers and other diseases. One can use imaging techniques such as magnetic resonance imaging and computed tomography to detect cancers only if a malignant tumor has grown to a certain size at a later stage of the disease. Hence, more sensitive detection methods for biomarkers are required to detect at earlier stages. Ultrasensitive detectors are also needed for viruses before they transmit widely. Enzyme-linked immunosorbent assay (ELISA), electrochemiluminescence immunoassay (CLISA), and various laser-based fluorescence methods are widely used for the detection of biomarkers and viruses. Our laser wave-mixing detection methods offer significant advantages over currently available methods, including ultrasensitive detection limit, high spatial resolution due to small probe volumes (nL to pL), and the use of millimeter-thin samples that can be mounted on microfluidics and microarrays controlled by piezo actuators. We demonstrated excellent detection sensitivity levels for thin samples of pancreatic cancer biomarker carbohydrate antigen 19-9 (CA 19-9) and breast cancer biomarker (human epidermal growth factor receptor 2) HER-2 at femtomole and zeptomole levels, respectively. Detection of HIV-1 p24 at the zeptomole level was also demonstrated. Since wave mixing requires much smaller probe volumes (nL to pL) we obtained much better mass detection limits and spatial resolution as compared to other methods, such as colorimetric assay and immunoassay (50 -100 µL sample volumes). Hence, wave mixing allows convenient interface to microfluidics and microchip-based detectors that are suitable for field use.

5.2 Introduction

5.2.1 Biomarkers

The pancreatic cancer biomarker CA 19-9, breast cancer biomarker HER-2, and HIV-1 p24 antigen are the thin samples on surfaces and microarrays used to demonstrate the sensitivity levels of laser wave-mixing detectors in this study. Pancreatic cancer is one of the most aggressive cancers worldwide. The 5-year survival rate could be improved by using multi-agent cytotoxic therapies (Park *et al.*, 2021); however, the diagnosis of pancreatic cancer remains challenging because most patients have nonspecific symptoms at a possible-surgical stage or even a more advanced stage (Siegel *et al.*, 2021). Secretin-enhanced magnetic resonant imaging (MRI) and magnetic resonance cholangiopancreatography (MRCP) combined with endoscopic ultrasound (EUS) could be used to identify pancreatic lesions. For more economical blood-based detection options, the Food and Drug Administration (FDA) approved CA 19-9 as the only biomarker, a cell surface glycoprotein complex defined by the antibody in a colorectal carcinoma cell line (Lee *et al.*, 2020).

Breast cancer is the most common cancer for women (Łukasiewicz *et al.*, 2021). The 5-year survival rate dramatically increases to 90% due to advanced screening programs based on breast cancer subtype classification and treatment personalization (Nardin *et al.*, 2020). Imaging of the breast (e.g., ultrasonography, mammography, single photon emission computed tomography (SPECT), positron emission tomography (PET), and MRI) is the most common way of diagnosis of breast cancers (Bhushan *et al.*, 2021). However, more sensitive biomarker-based detection methods are needed to complement imaging methods. Approximately 30% of breast cancers have amplification or overexpression of the HER-2 gene (Mitri *et al.*, 2012). It is a transmembrane receptor tyrosine kinase belonging to the erythroblastic oncogene B (ErbB) protein family. It

consists of an extracellular region with a ligand binding domain, a hydrophobic transmembrane region, and an intracellular region with a tyrosine kinase domain (Roskoski, 2014). HER-2 is activated by ligand-independent dimerization with all the other ErbB family members. The heterodimer of HER-2 and HER-3 are the most active combination that initiates downstream signaling pathways and promotes tumors (Mitri *et al*., 2012; Gajria & Chandarlapaty, 2011). HER-2 can form a breast cancer biomarker panel with estrogen receptor (ER) and progesterone receptor (PR) (Gamble *et al*., 2021). Immunohistochemistry (IHC) and in-situ hybridization (ISH) are two FDA-approved clinical assays for the detection of HER-2 (Hicks *et al*., 2018). According to the FDA, the cutoff value of HER-2 concentration in breast cancer is 15.0 ng/mL (Shamshirian *et al*.). Table 5-1 compares currently available optical detection methods for HER-2, and some of them are relatively expensive and time-consuming methods.

Research in viral biology, pathogenesis, and antiretroviral therapies, has been enlightened by HIV studies (Schwetz & Fauci, 2019). More than 40 million people have died from HIV-related causes, and 84.2 million people have been infected with HIV since the epidemic started (Joint United Nations Progamme on HIV/AIDS, 2022). HIV infections have increased during the COVID-19 pandemic due to slow response and disruption of HIV-related service. The most commonly used HIV diagnostic tests rely on reactive antibody production. However, the immune system of infected people takes 28 days (window period) to develop enough antibodies to be detected (World Health Organization, 2022). Early, reliable and sensitive diagnosis could reduce the risk of transmission, especially during this 28-day time window. Detection of viral RNA and virological biomarker p24 antigen can be achieved during this time window (Gray *et al*., 2019).

Capsid protein p24 is a 24 kDa protein that can be polymerized to form a protective shell of the HIV virion. The concentration of the p24 antigen is 50 attomolar to 15 femtomolar in the first

Table 5-1 Comparison of detection methods for HER-2

Methods	Concentration (ng/mL)	Probe Volume (nL)	Mass Detection Limit (ng)	Time (min)	Reference
ELISA	8.0e-3	5.0e4	4.0e-4	285	ErbB2 (HER2) Human ELISA Kit, Invitrogen
Opto-fluidic ring resonator	13	2.0e4	2.6e-1	30	Gohring *et al.*, 2010
Fiber-optic ball-tip resonator	1.5e-8	2.6e4	3.9e-10	15	Sypabekova *et al.*, 2022
Electrochemiluminescence	2.0e-2	5.0e2	1.0e-5	14	Guerrero-Esteban *et al.*, 2021
Plasmonic optical fiber assay	9.3	1.25e5	1.2	10	Loyez *et al.*, 2021
Photoelectrochemical sensor	2.6e-5	9.0e5	2.3e-5	1	Luo *et al.*, 2021
Laser wave mixing	**40.**	**0.16**	**6.4e-6**	**<1**	**This study**

infected phase. Current published ultrasensitive detection methods can detect 2 HIV-1 p24 proteins in 100 µL volume. For example, expensive gold nanoparticles are needed to enhance the sensitivity levels of some of the currently available detection methods (Macchia *et al.*, 2019). Table 5-2 compares currently available optical detection methods for p24 antigen.

5.2.2 Current Optical Detection Methods

Immunoassays, including the enzyme-linked immunosorbent assay (ELISA) and chemiluminescence immunoassay (CLIA), are major techniques currently available for the detection of biomarkers used in this study (CA 19-9, HER-2, and p24). The biomarkers are sandwiched between the capture antibody and the detection antibodies. The capture antibodies are immobilized on the surface of the wells, and blocking reagents are added before antigens to avoid nonspecific binding. The detection antibodies are conjugated with enzymes that develop some color upon binding to substrates. Gold nanoparticles could be used to enhance fluorescence signals, as previously reported (Jawad *et al.*, 2017; Hicks *et al.*, 2018; Kosaka *et al.*).

5.2.3 DFWM Spectroscopy Interfaced with Customized Sample Cell

Our laser wave-mixing detection methods offer less expensive and faster analyses while allowing the use of smaller sample probe volumes (nL to pL) that are inherently suitable for microarrays and microfluidics. Equation 5-1 shows that the wave-mixing signal (I_{signal}) exhibits a quadratic dependence on analyte concentration (α) and a cubic dependence on laser power (I_1 and I_2). The effective use of low laser power levels (mW) allows minimize photodegradation and still yields significant signal response.

$$I_{signal} \approx \left(\frac{b}{8\pi}\right)^2 I_1{}^2 I_2 \frac{\lambda^2}{\sin^4\left(\frac{\theta}{2}\right)} \left(\frac{dn}{dT}\right)^2 \frac{\alpha^2}{\kappa^2} \qquad (5-1)$$

Proper alignment of the laser wave mixing setup is critical in achieving excellent sensitivity levels. Optical background noise levels are easily eliminated using spatial filters since the signal

Table 5-2 Comparison of detection methods for p24 antigen

Methods	Concentration (pg/mL)	Sample Volume (nL)	Mass Detection Limit (pg)	Time	Reference
Nanomechanical and optoplasmonic transduction	1.0e-5	1.0e6	1.0e-5	4hr 45min	Kosaka *et al*., 2017
ELISA with thio-NAD cycling	2.0e-2	5.0e4	1.0e-3	4hr 30min	Nakatsuma *et al*., 2015
Immunofluorescent cytometric bead assay	4.0e-1	5.0 4	2.0e-2	4hr 20min	Biancotto *et al*., 2009
Laser wave mixing	**1.3e2**	**1.0e5**	**1.3e2**	**4hr**	**This work**

beam is a coherent laser-like beam. The angle between two beams (θ) should be as small as possible to obtain wider and more stable grating period, and hence, stronger signals via non-radiative thermal relaxation (J. H. Kim *et al*., 1995; Heilweil & Hochstrasser, 1985). The smaller crossing angle can be achieved by minimizing the distance between two parallel input beams before they pass through the focusing lens. The sample holder, positioned at the focal point, is mounted on an XYZ-translational stage (Figure 5-1a) for precise positioning. Thermal conductivity (κ) is important and most buffer media used for biosamples are suitable for wave-mixing detection. If the heat dissipation is small, the refractive index change with temperature change (dn/dT) is more significant (Aggarwal & Fan, 2005).

Figure 5-1b shows the customized sample cell used in this work. An electrical tape or a silicone isolator is sandwiched between two slides to isolate the sample spots and avoid cross-contamination. The thickness of the electrical tape or the silicone isolator determines the optical path length (b). The sample probe volume is determined from the thickness of the sample and the laser probe volume (overlapping beam volume) at the focal point, and the following equation can be used to estimate the probe volume,

$$V = (\frac{2\lambda F}{\pi\omega})^2 \pi b \qquad (5-2)$$

where λ denotes the excitation laser wavelength, F represents the focal length, ω is the beam diameter, and b is the thickness of the sample cell (Sirohi, 2017). Our example probe volume is estimated to be 0.16 nL when using a 532 nm laser with a beam diameter of 1.9 mm, 10-cm focusing lens, and a 0.16 mm thick sample sandwiched by 2 glass slides. When using a 0.5 mm thick silicone isolator, the sample probe volume increases is estimated to be 0.5 nL.

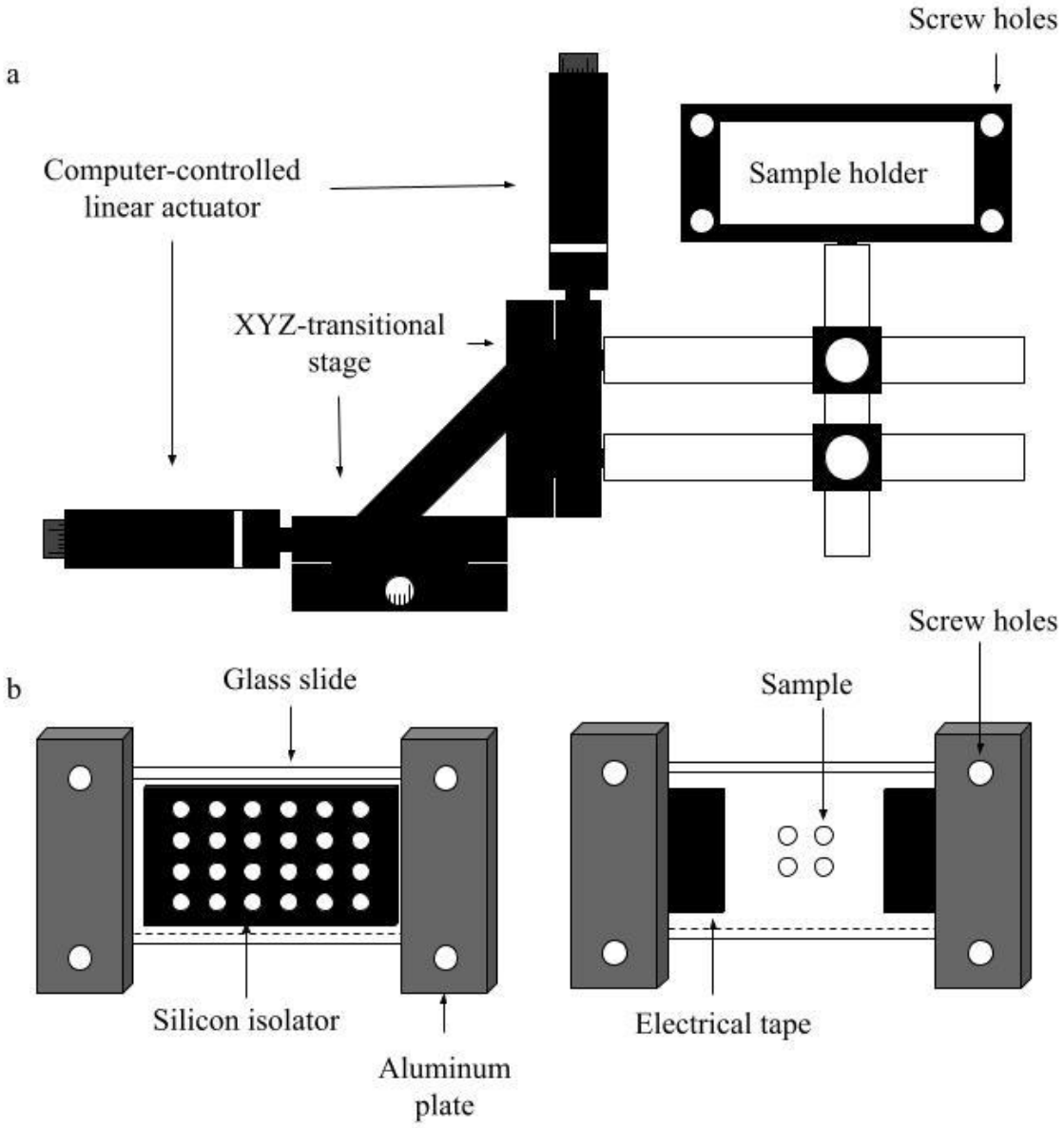

Figure 5-1 (a) Sample holder mounted on XYZ translational stage, and (b) customized sample cell designs.

5.2.4 Immunoassay Performed on a Glass Slide to Enhance Specificity Level

Immobilization of proteins (antibodies or antigens) can be achieved by pretreatment of microscope glass slide with triethoxysilane (APTES) and N-hydroxysulfosuccinimide (Sulfo-NHS)/1-ethyl-3-[3-dimethylaminopropyl] carbodiimide (EDC) (Didar, 2011), and APTES is used to coat the surface of a glass slide for the wave-mixing detection system, and then NHS/EDC coupling is performed to immobilize the antigen. However, EDC is highly moisture sensitive and affects the coupling reaction. Alternatively, functionalizing the APTES-coated glass with glutaraldehyde allows aldehyde functionality. The glutaraldehyde forms stable C=N covalent linkages with the amine groups of both APTES and protein molecules to achieve the immobilization of proteins on a glass slide (Chuah *et al*., 2015).

To simplify the preparation process and omit plastic antibody-coated microplates, the direct ELISA is adopted by immobilization antigen on a glass slide in this work. Instead of pre-coating the surface of wells with the capture antibody, immobilization of antigen on a glass slide is performed on the APTES-coated glass.

5.3 Experimental

5.3.1 Laser Wave-Mixing Setup

Figure 5-2 shows a schematic diagram of a forward-scattering laser wave-mixing setup. A diode-pumped solid-state laser (MBL-III-473nm-100mW, BL-III-447nm-200mW or MGL-III-532nm-100mW, Opto Engine LLC., Midvale, UT) serves as the excitation source. The laser power measured in front of the sample is approximately 30 mW. A 70:30 (T: R) beam splitter splits the laser beam into two input beams. These two input beams are refocused and mixed inside the sample cell after traveling the same distance using mirrors (PF10-03-G01, Thorlabs, Newton, NJ) and a 10-cm focusing lens (LA1509-A, Thorlabs, Newton, NJ). One of the input beams is optically

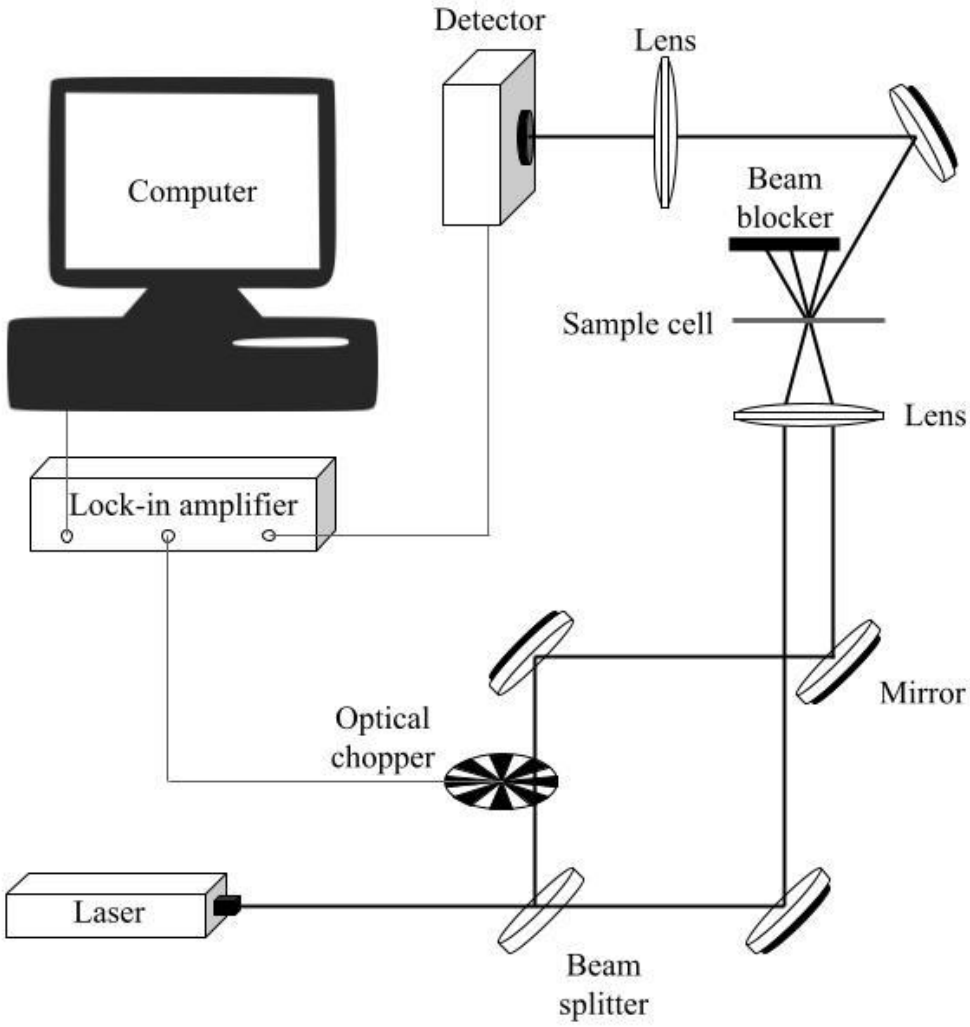

Figure 5-2 Forward-scattering laser wave-mixing setup.

chopped at 320 Hz, and the optical chopper is interfaced with a lock-in amplifier to enhance the signal-to-noise ratio (S/N). A microfluidic chip (Model X3550, Micronit, Netherlands) is used for wave-mixing signal optimization. Analog signals collected by a photodiode detector (PDA36A, Thorlabs, Newton, NJ) are digitized and recorded by the customized software (AIDA). Crystal Violet (Thermo Fisher Scientific, Waltham, MA) is used as the alignment dye for the 532 nm laser wave-mixing setup; Congo red (Thermo Fisher Scientific, Waltham, MA) is used as the alignment dye for the 473 nm laser wave-mixing setup; and ethyl orange (Thermo Fisher Scientific, Waltham, MA) is used as the alignment dye for the 447 nm laser wave-mixing setup.

5.3.2 Customized Sample Cells

As shown in Figure 5-1b, two customized sample cells are used in this work. The first cell is assembled by putting two small pieces of electrical tape near the edge of a microscope glass slide (Thermo Fisher Scientific, Waltham, MA). The electrical tape thickness is the sample thickness. After pipetting the 0.5 µL sample on the bottom microscope glass slide, the top or cover slide (Thermo Fisher Scientific, Waltham, MA) is mounted to hold a thin layer of sample.

The second cell or sample holder is assembled by using a press-to-seal silicone isolator with 24 wells (2 mm diameter x 0.5 mm depth) from Grace Bio Labs (Bend, OR). When it is sandwiched between two glass slides, the volume capacity of each well is 1.57 µL. The sample volume (1.2 µL) deposited is less than the volume capacity of the well to avoid cross-contamination between wells. The thin sample spots could be held vertically or horizontally inside the laser wave-mixing detection setup using an XYZ translational stage (Newport, Irvine, CA) for precise positioning and alignment. The XYZ translational stage is controlled by two linear computer-controlled actuators (Model TLA-28A and Model TLA-60A, Zaber Technologies, Vancouver, Canada) on the X-axes and the Z-axes, as shown in Figure 5-1a.

5.3.3 Chemicals and Reagents

All solutions and buffers are prepared using ultrapure water, sonicated, and filtered through a 0.20 μm syringe filter (GVS North America, Sanford, ME). Sodium bicarbonate, bovine serum albumin (BSA), methanol, and acetone are acquired from MilliporeSigma (Burlington, MA). A BCA protein assay kit, N, N-*Dimethylformamide* (DMF), QSY 7 Carboxylic Acid, Succinimidyl Ester, 5-(and 6)-carboxytetramethylrhodamine, succinimidyl ester (NHS Rhodamine), regenerated cellulose dialysis tubing (MW_{CO} 12-14 kDa), APTES, and Tween-20 are purchased from Thermo Fisher Scientific (Waltham, MA). Chromeo P540 is obtained from Active Motif (Carlsbad, CA). HER-2 (ACROBiosystems, Newark, DE), CA 19-9 native proteins (My BioSource, San Diego, CA), and HIV-1 p24 antigen ELISA kit (ZeptoMetrix, Buffalo, NY) are analytes studied in this work.

5.3.4 Sample Preparation

The working reagent is prepared for the BCA assay by mixing 0.5 mL of 4% $CuSO_4$ and 10 μl of 1% of BCA from Pierce BCA protein assay kit. BSA or HER-2 is dissolved in 0.1 M sodium bicarbonate, and 50 μL of working reagents are added to 50 μL of protein solution at various concentrations. These mixtures are incubated at 60°C for 30 minutes. The optical absorption spectra at 562 nm are collected using a UV-visible spectrophotometer.

To label proteins, 1 mg Chromeo P540, NHS-Rhodamine, or QSY 7 is dissolved in 100 μL DMF. The dye solution is slowly added to the 1 mL of 2 mg/mL protein solution to obtain a 4: 1 (dye: protein) molar ratio and mixed. The Chromeo P540-conjugated protein solution is incubated at 55 °C for 2 hours, and NHS-Rhodamine-conjugated protein solution and QSY 7-conjugated protein solution are incubated at room temperature for 1 hour. Excess dye is removed by dialysis. A snake scan is performed on a dry spot of 5×10^{-4} M ethyl orange prepared in

methanol. The solution is deposited on the same area of a microscope glass side three times. The bottom layer is dried before applying the next layer.

To pre-coat a microscope glass slide, 2% solution of APTES in acetone is deposited on the glass slide. The glass slide is then rinsed with acetone after 30 s. After the surface of the glass slide is dried, 100 µL of 125 µg/mL p24 antigen is deposited on the pre-coated glass slide and then stored at room temperature for 1 hour in a sealed container to avoid air drying. The surface of the glass slide is then rinsed with diluted (1:10) plate wash buffer in the ELISA kit three times. Subsequently, 100 µL of blocking solution (5% w/v non-fat dry milk and 0.1% Tween-20 in assay diluent in the ELISA kit) is deposited on the glass slide and incubated for 1 hour before the second wash. The same amount of reconstituted HIV-1 p24 detector antibody, streptavidin-peroxidase working solution, and substrate working solution are deposited successively on the glass slide and incubated for 30 to 60 minutes. The stop solution is deposited to develop a color change from blue to yellow.

5.3.5 UV-Visible Spectra

A UV-visible spectrophotometer (8453, Agilent, Santa Clara, CA) is used to obtain the UV-visible spectra using a Quartz cuvette (Starna Cells, Inc., Atascadero, CA) with a 1-cm path length. The UV-visible spectrophotometer is blanked with the solvent for all the analytes.

5.4 Result and Discussion

5.4.1 Lower Detection Limits of BSA and HER-2

The BCA assay protocol is modified by adjusting the sample to BCA working reagent volume ratio from 8:1 to 1:1 in order to enhances the sensitivity levels from 5 µg/mL to 0.02 µg/mL (Brescia & Banks, 2021). Figure 5-3 shows that the absorbance difference is insignificant at low BSA concentrations but laser wave-mixing detection can still yield strong signals since the

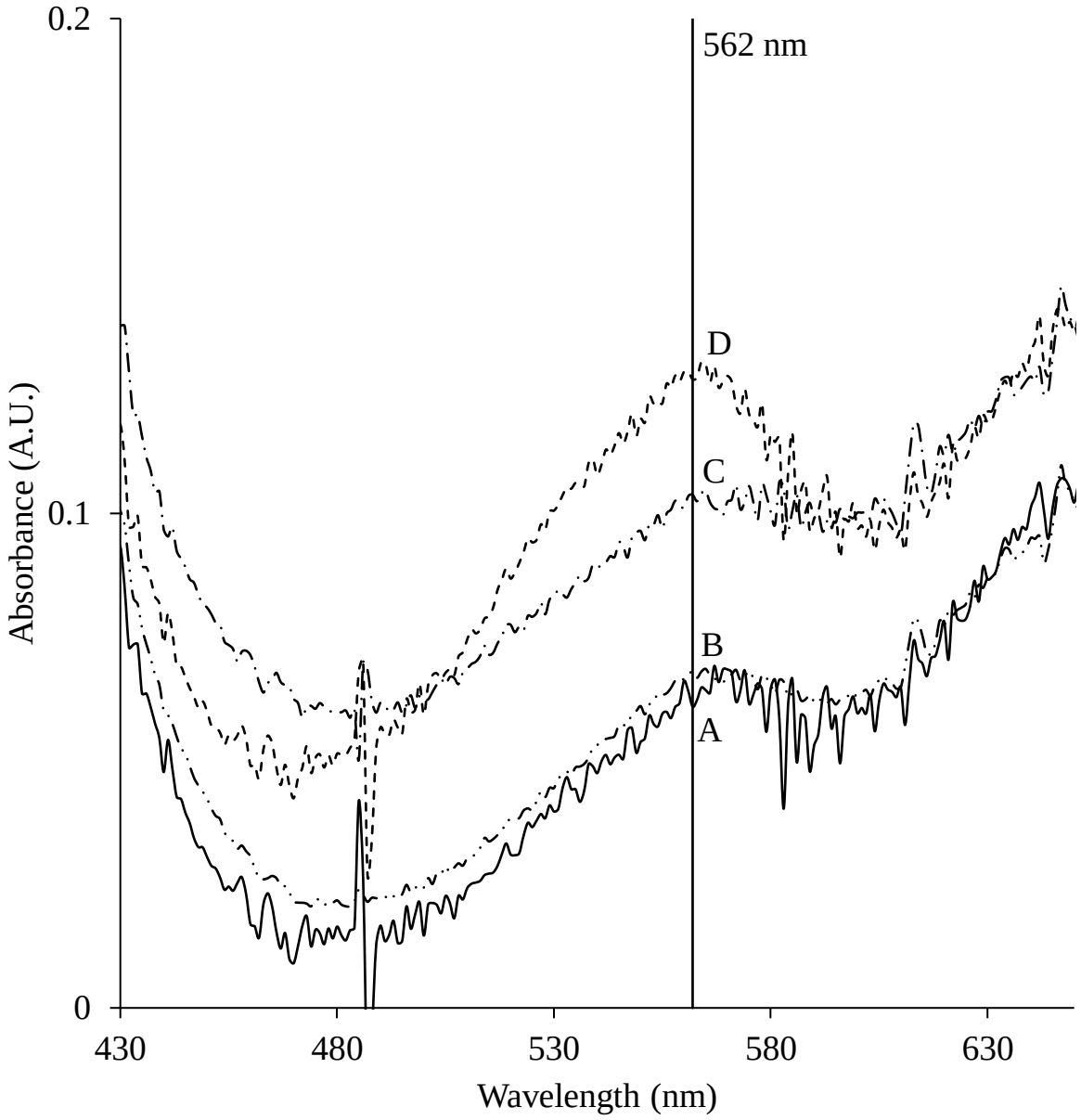

Figure 5-3 UV-visible absorption spectra of BCA reagent mixed with BSA at concentrations of (A) 0 µg/mL, (B) 0.02 µg/mL, (C) 0.2 µg/mL, and (D) 2 µg/mL (BSA to BCA working reagent volume ratio is 1:1).

signal has a quadratic dependence on analyte concentration.

The purple-colored Cu(I)-BCA complex has an absorption peak at 562 nm. and hence, a 532 nm solid-state laser is used as the laser excitation source. The sample cell is created by using a 0.16 mm thin electrical tape sandwiched between two glass slides. The colored Cu(I)-BCA complex is utilized as a chromogenic reporter for demonstrating excellent detection limits of BSA, as shown in Figure 5-4, and HER-2, as shown in Figure 5-5. The laser wave-mixing signal is confirmed for each analyte by alternately blocking one of the input beams and observing the signal peaks in Figure 5-4 and Figure 5-5 when both input beams are present. The baseline indicates the thermal grating disappears when one of two input beams is manually blocked. Hence, the signal drops back to the baseline in an ideal situation. However, when the unchopped input beam is blocked (e.g., the first baseline), the background noise (inherent laser noise or noise scattered from the sample cell and the optical components) that has the same frequency as the reference frequency is recorded. The agitation of the sample molecules results from the laser heating up the sample may cause the fluctuation in the signal intensity.

Figure 5-6 shows the wave-mixing signal and its quadratic dependence on sample thickness, i.e., optical path length. The thickness of an electrical tape is 0.16 mm, and the sample thickness, i.e., the gap between the glass slides holding the sample, is increased to yield stronger wave-mixing signals (up to a thickness of 0.64 mm tested).

Figure 5-7 shows the photodegradation study of colored Cu(I)- BCA complex produced from HER-2 at 1.5 µg/mL and 4 µg/mL concentration levels. The colored Cu(I)- BCA complex from 4 µg/mL of HER-2 yields less photodegradation those from HER-2 at 1.5 µg/mL after it is exposed to 30 mW laser power for 2 minutes. The higher concentration sample yields less photodegradation as expected (Torniainen *et al*., 1996; Groeneveld *et al*., 2022). Nevertheless,

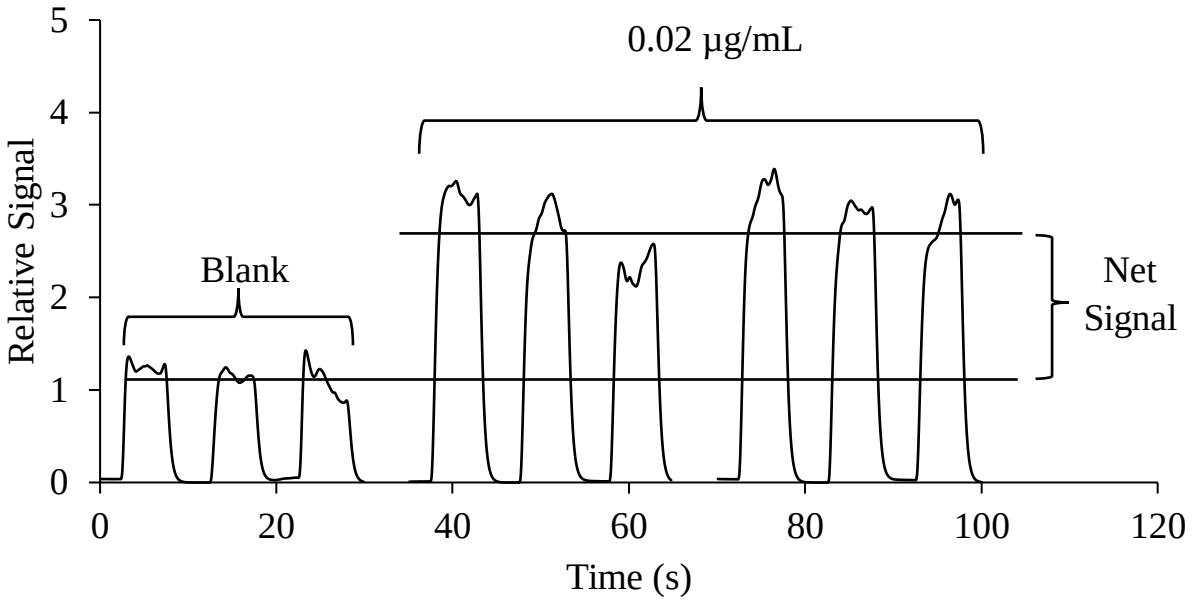

Figure 5-4 The wave-mixing signals of colored Cu(I)-BCA complex produced from BSA at concentrations of 0 µg/mL (blank) and 0.02 µg/mL (BSA to BCA working reagent volume ratio is 1:1).

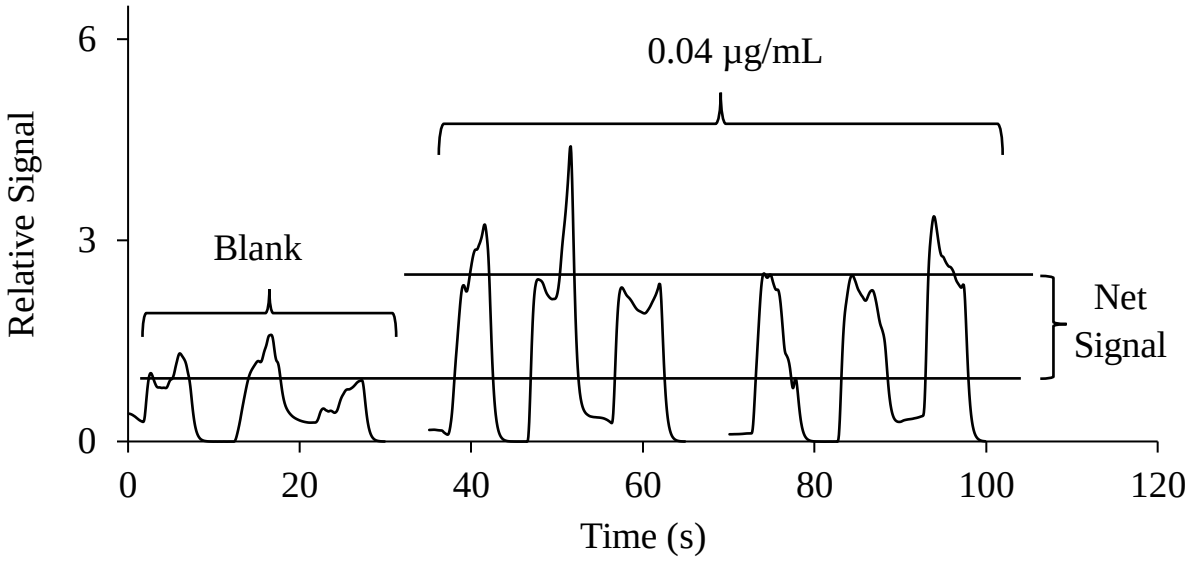

Figure 5-5 Laser wave-mixing signals of colored Cu(I)-BCA complex produced from HER-2 at 0 µg/mL and 0.04 µg/mL concentration levels (HER-2 to BCA working reagent volume ratio is 1:1).

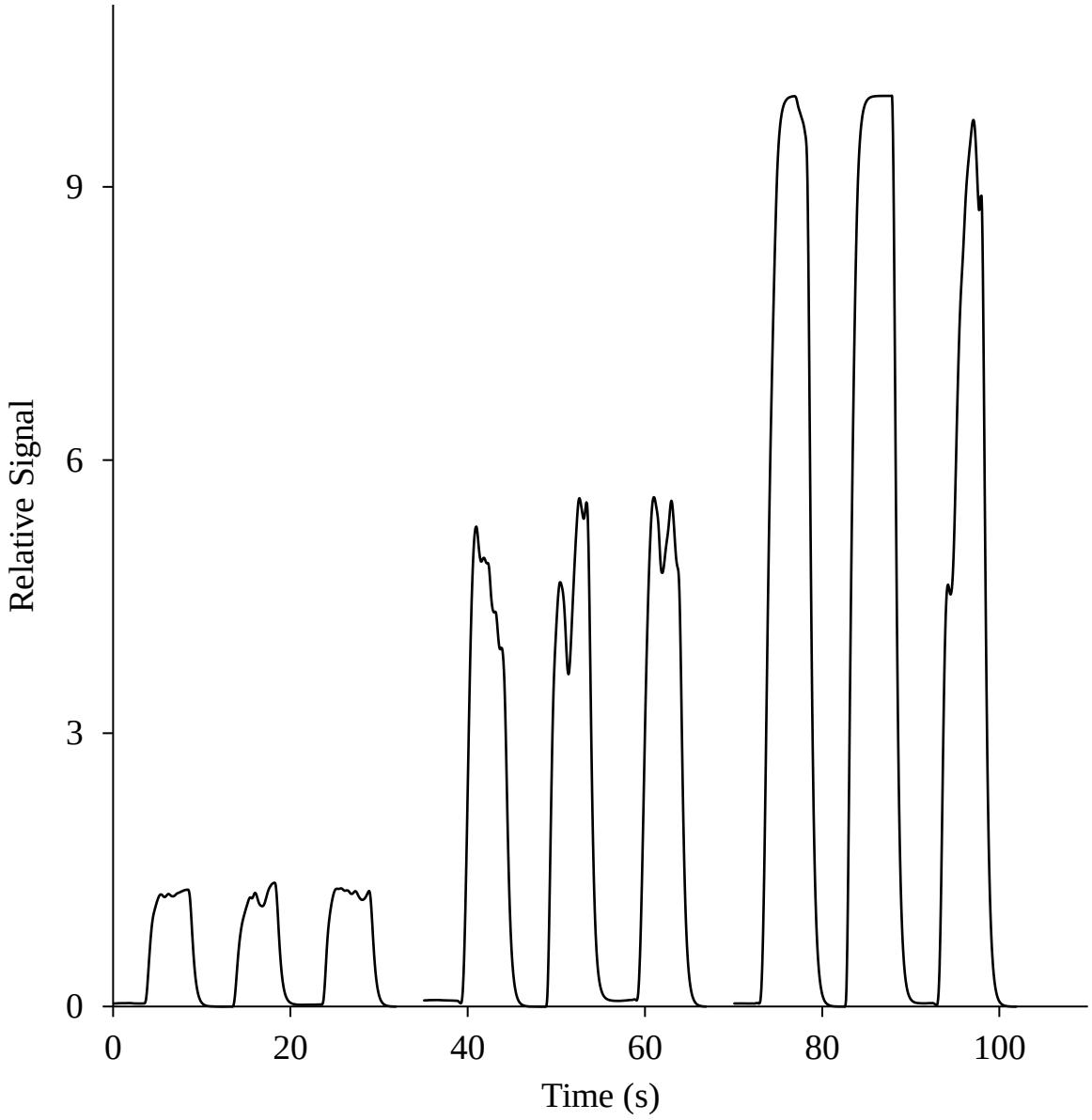

Figure 5-6 Laser wave-mixing signals of colored Cu(I)-BCA complex produced from 0.4 µg/mL HER-2 using different optical path lengths or sample thicknesses (0.16 mm, 0.32 mm, and 0.48 mm).

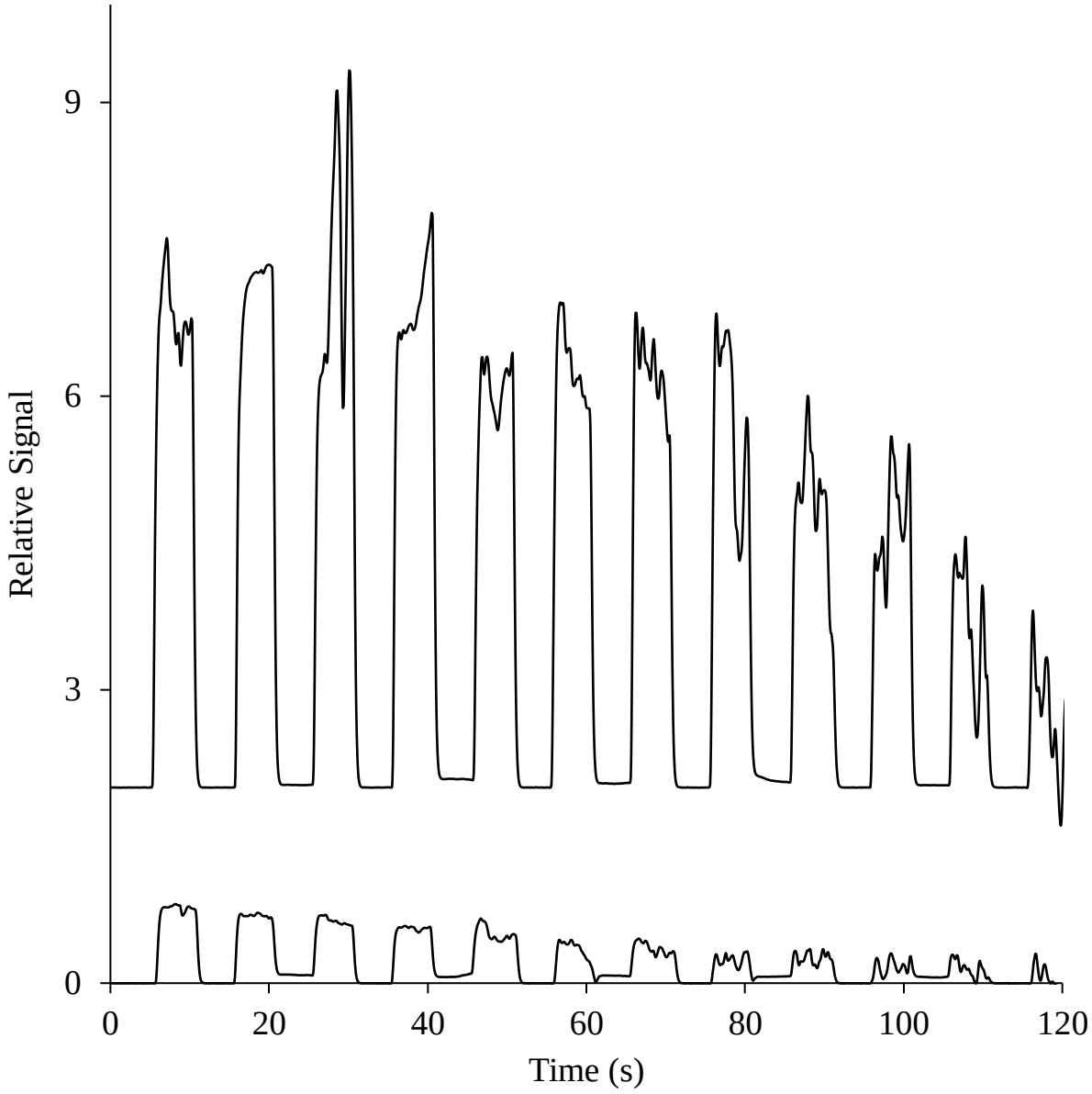

Figure 5-7 Laser wave-mixing signals of colored Cu(I)-BCA complex produced from HER-2 at 1.5 µg/mL (bottom) and 4 µg/mL (top) concentration levels (HER-2 to BCA working reagent volume ratio is 1:1).

photodegradation is negligible at any concentration level, even for static samples, not to mention flowing samples as in microfluidics, since the wave-mixing signals are recorded in milliseconds, not minutes.

5.4.2 Wave-Mixing Detection by Scanning

In addition to using thin samples sandwiched between 2 glass slides, dried samples on glass slides are tested for our wave-mixing detector. Two spots of colored Cu(I)-BCA complex from HER-2 at 0 μg/mL (blank) and 4 μg/mL (sample) are deposited and then dried on a glass slide. Figures 5-8 shows wave-mixing signals from 1.2 μL of colored Cu(I)-BCA complex and the blank (containing cupric ions and BCA) spots that are dried on a glass slide. The two sample spots are scanned horizontally using a computer-controlled linear actuator. Air-dried sample spots on a glass slide yield multi-peak signal profiles due to the inhomogeneous distribution of the analytes, which is confirmed with microscopy. This basic and fast mode of detection offers convenient sample drops that yield good detection limits even when using micrometer-thin samples.

The 532 nm green solid-state laser is compact, inexpensive, and suitable for the excitation of many protein labels, as summarized in Table 5-3. These amine-active labels form covalent bonds with primary amines in proteins. Figure 5-9 shows UV-visible absorption spectra of native CA 19-9, Chromeo P540-conjugated CA 19-9, NHS-Rhodamine-conjugated CA 19-9, and QSY 7-conjugated CA 19-9. The wavelength of the absorption peak of Chromeo P540 shifts to 533 nm upon binding to a protein, with the quantum yield increases to 20%. Although NHS-Rhodamine has an absorption peak at 552 nm (not as close to the 532 nm laser line), its extinction coefficient is significantly higher than that of Chromeo P540, and its quantum yield is also high at 80% (Savarese *et al.*, 2012). Our laser wave-mixing method is an absorption-based method, and hence, molar absorptivity is more important than the quantum yield (Vander Wal *et al.*, 1992). QSY 7 is

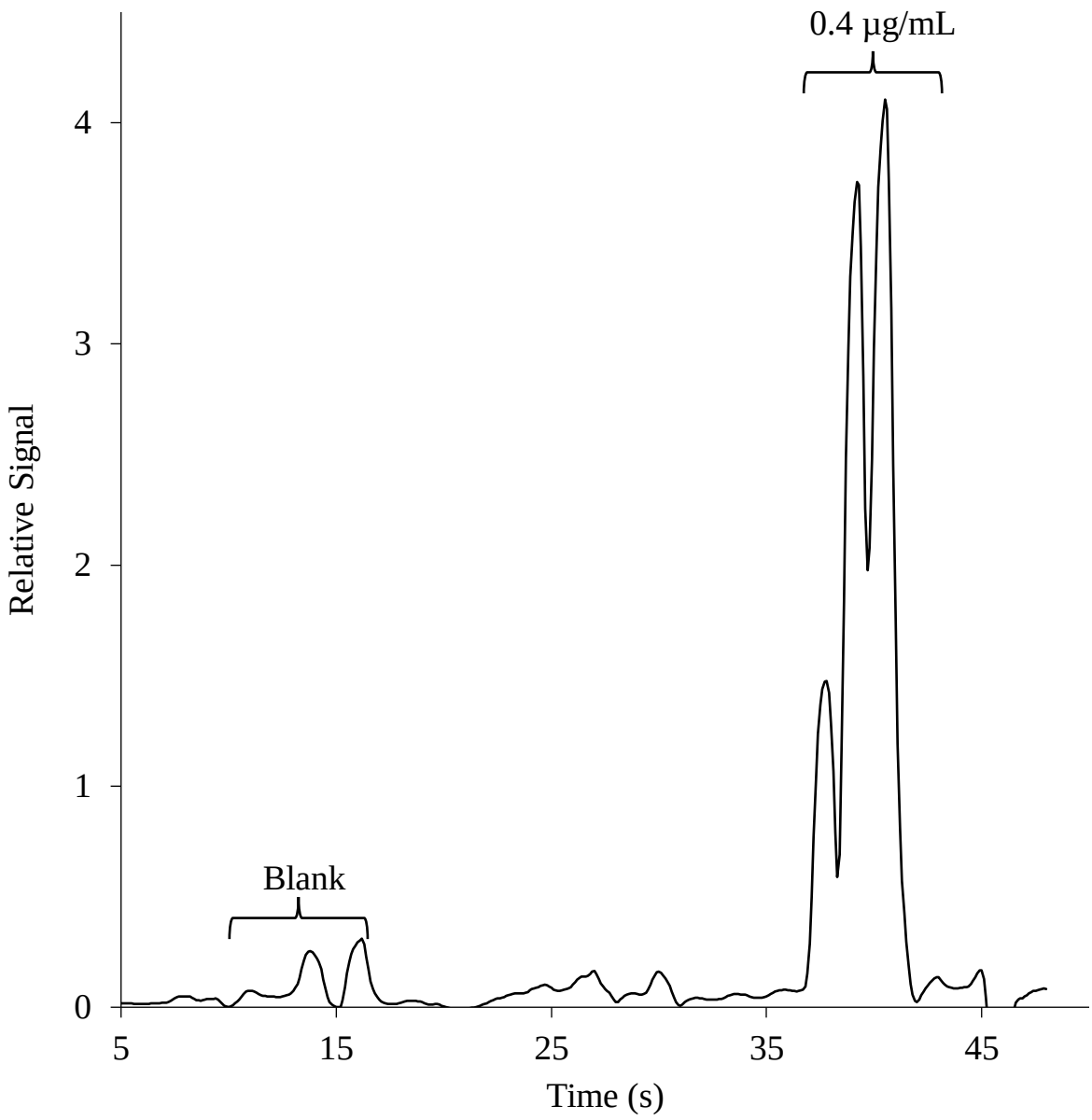

Figure 5-8 Laser wave-mixing signals of HER-2 at the concentrations of 0 µg/mL (blank) and 0.4 µg/mL. The samples are deposited on a glass slide and then dried.

Table 5-3 Comparison of protein labels

Label	Extinction Coefficient (M^{-1} cm^{-1})	Quantum Yield	Degradation of Excess Dye
NHS-Rhodamine	80,000	80%	No
QSY 7	90,000	<0.001%	No
Chrome P540	50,000	20 %	Yes

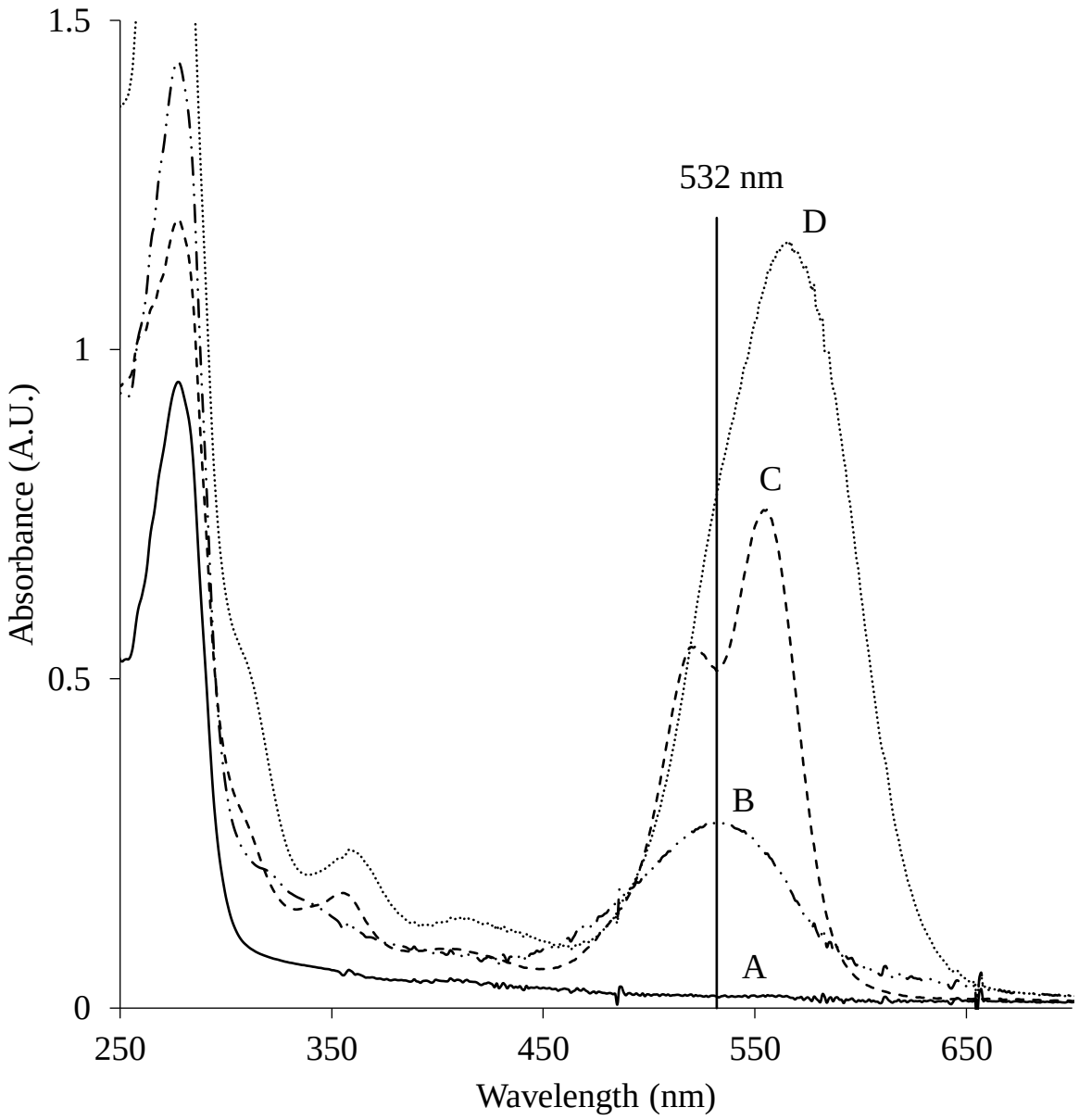

Figure 5-9 UV-visible absorption spectra of (A) 160 U/mL native CA 19-9, (B) Chromeo P540-conjugated CA 19-9, (C) NHS-Rhodamine-conjugated CA 19-9, and (D) QSY 7-conjugated CA 19-9.

a chromophore label (not fluorophore) that has a very strong absorption peak at 532 nm. Therefore, Chromeo P540 and QSY 7 are chosen to label the CA 19-9 biomarker for our wave-mixing detection.

Figures 5-10 and 5-11 show laser wave-mixing signals from a horizontal scan of 160 U/mL labeled CA 19-9 and its control in sample wells (2 mm diameter) created by the silicone isolator. Some variations in the signal levels may be cause by the sample wells not being uniformly filled with the samples.

Python codes (see Figures 5-12 and 5-13) were written to control the actuator movements. Figure 12a shows the scanning pattern of the actuator driven by Python codes to scan and detect three sets of 5×10^{-4} M ethyl orange. Since ethyl orange has a strong absorption peak at 447 nm, a 447 nm compact solid-state laser is used as the laser excitation source. The actuator scanning pattern (i.e., a snake scan) probe sample locations from top to bottom in the first column, from bottom to top in the second column, from top to bottom in the third column, etc. Detection reproducibility of a snake scanning pattern is better compared to that of a raster scan, in which the sample well is probed and scanned from top to bottom in the first column and again from top to bottom in the second and third columns (Vani & Sangeetha, 2012). Figure 5-14b shows the signal intensity vs. time during the snake scanning pattern, i.e., the sample probe positions are estimated in the 2D space based on the time needed to scan the sample well and digitize the signal using our custom-built data acquisition software (AIDA).

Figure 5-15 shows laser wave-mixing signals from horizontal scans of a microchannel filled with 160 U/mL of Chromeo P540-conjugated CA 19-9. As expected, the use of a slower scan rate at 0.2 mm/s yields better signal-to-noise ratios and higher spatial resolution compared to those when using a faster scan rate of 1.5 mm/s. Ideally, the signal peaks should be symmetrical

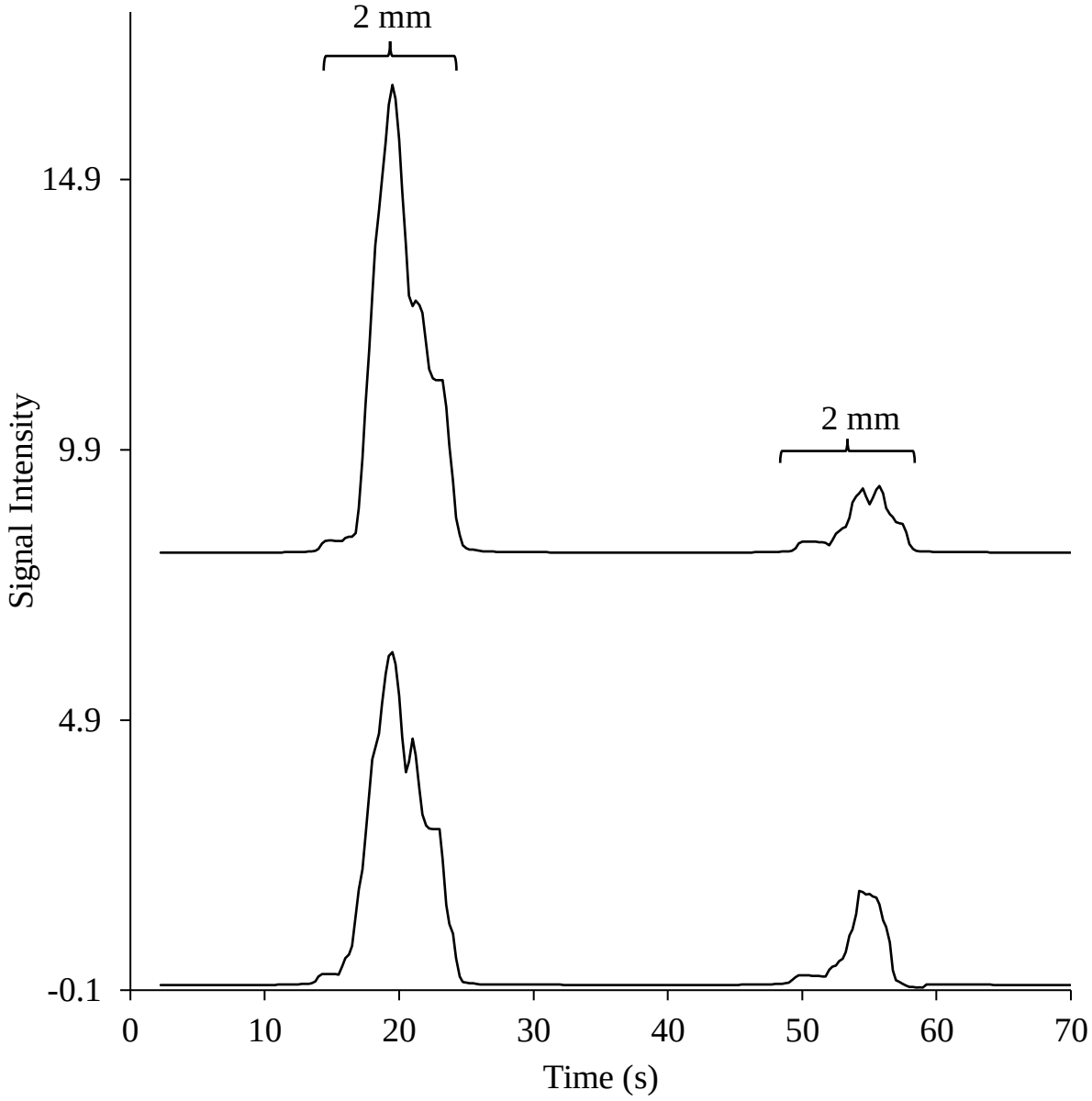

Figure 5-10 Reproducible laser wave-mixing signals from a horizontal scan of 160 U/mL Chromeo P540-conjugated CA 19-9 in 0.1M sodium bicarbonate buffer and Chromeo P540 (blank) in different wells separated by the silicone isolator. The actuator scan rate is 0.2 mm/s.

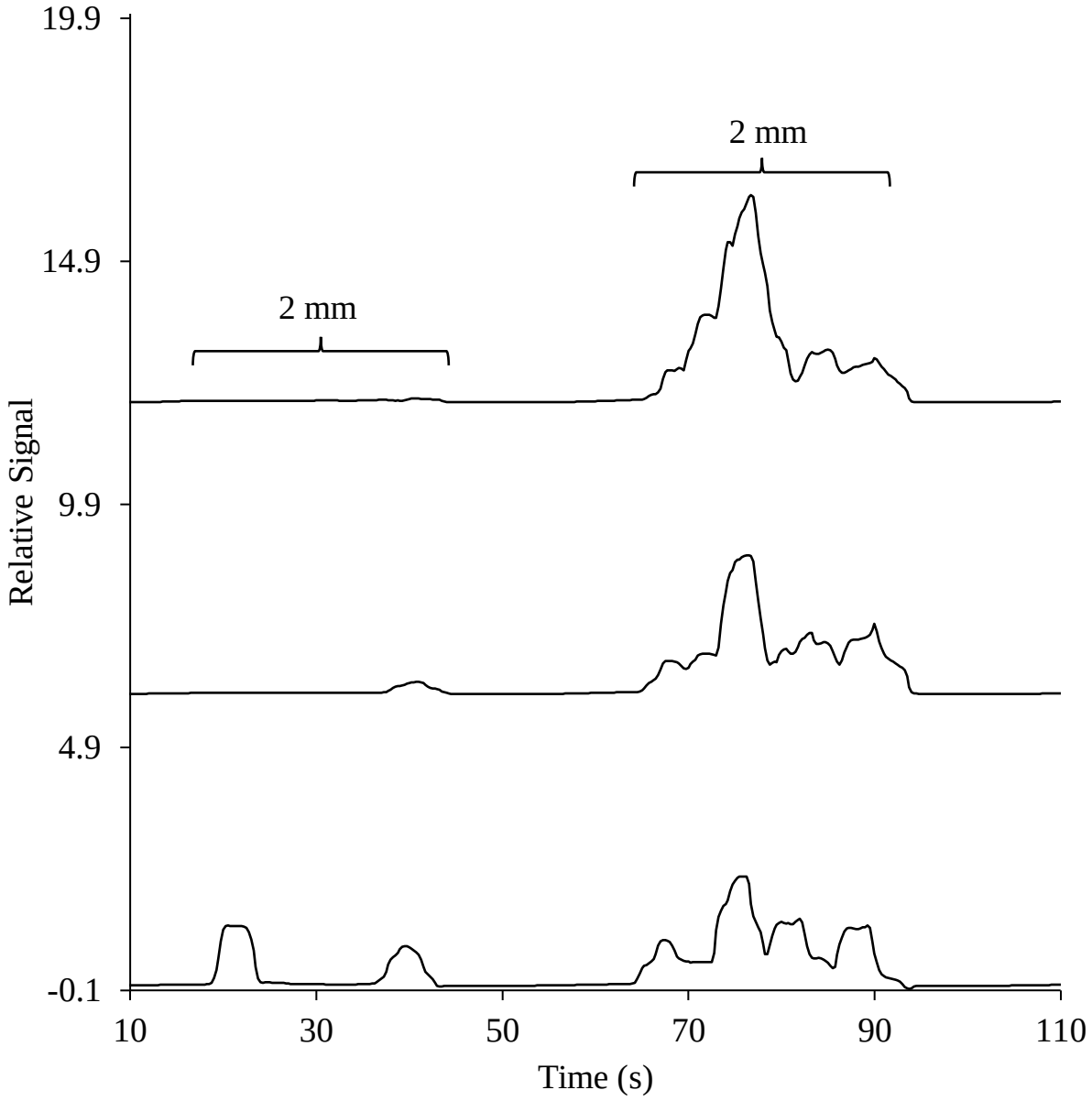

Figure 5-11 Laser wave-mixing signals from a horizontal scan of 0.1M sodium bicarbonate (blank) and 160 U/mL QSY 9-conjugated CA 19-9 in different wells separated by the silicone isolator. The actuator scan rate is 0.08 mm/s.

```
from zaber_motion import *
from zaber_motion.binary import Connection
from zaber_motion import Units

Library.enable_device_db_store()

with Connection.open_serial_port("/dev/tty.usbserial-AD0JEGCD") as connection:
    device_list = connection.detect_devices()
    print("Found {} devices".format(len(device_list)))

    # indent this code under the "with" statement
    y_axis = device_list[0]
    x_axis = device_list[1]

    y_axis.home()
    x_axis.home()

    start_y = 0
    start_x = 0
    cols = 4
    rows = 3
    spacing = 1

    y_axis.move_absolute(start_y, Units.LENGTH_MILLIMETRES)
    x_axis.move_absolute(start_x, Units.LENGTH_MILLIMETRES)

    print("Start Scan")

    for i in range (0,cols):
        if i != 0:
            x_axis.move_relative(spacing, Units.LENGTH_MILLIMETRES)

        if (i % 2) == 0: #even
            y_axis.move_relative(spacing, Units.LENGTH_MILLIMETRES)
            y_axis.move_relative(spacing, Units.LENGTH_MILLIMETRES)
            y_axis.move_relative(spacing, Units.LENGTH_MILLIMETRES)
        else:
            y_axis.move_relative(-spacing, Units.LENGTH_MILLIMETRES)
            y_axis.move_relative(-spacing, Units.LENGTH_MILLIMETRES)
            y_axis.move_relative(-spacing, Units.LENGTH_MILLIMETRES)
```

Figure 5-12 Python commands for snake scan step by step.

```
from zaber_motion import *
from zaber_motion.binary import Connection
from zaber_motion import Units
import time

Library.enable_device_db_store()

with Connection.open_serial_port("/dev/tty.usbserial-AD0JEGCD") as connection:
    device_list = connection.detect_devices()
    print("Found {} devices".format(len(device_list)))

    # indent this code under the "with" statement
    y_axis = device_list[0]
    x_axis = device_list[1]

    y_axis.home()
    x_axis.home()

    start_y = 0
    start_x = 0
    cols = 4
    rows = 3
    spacing = 1

    y_axis.move_absolute(start_y, Units.LENGTH_MILLIMETRES)
    x_axis.move_absolute(start_x, Units.LENGTH_MILLIMETRES)

    print("Start Scan")

    for i in range (0,cols):
        if (i != 0):
            x_axis.move_relative(spacing, Units.LENGTH_MILLIMETRES)


        if (i % 2) == 0:# even
            for j in range (0,rows):
                y_axis.move_relative(spacing, Units.LENGTH_MILLIMETRES)
                continue

        else: #odd
            for k in range (0,rows):
                y_axis.move_relative(-spacing, Units.LENGTH_MILLIMETRES)
                continue
```

Figure 5-13 Python commands for snake scan using a for-loop.

a)

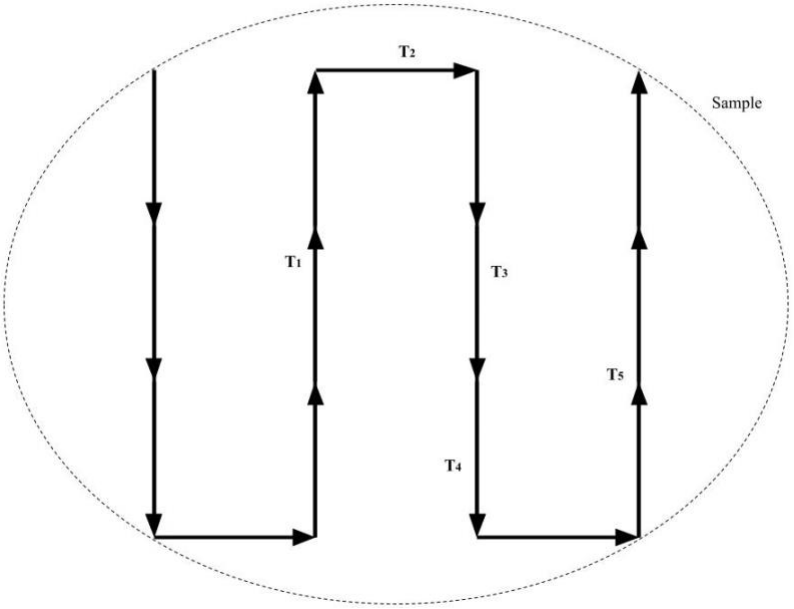

b)

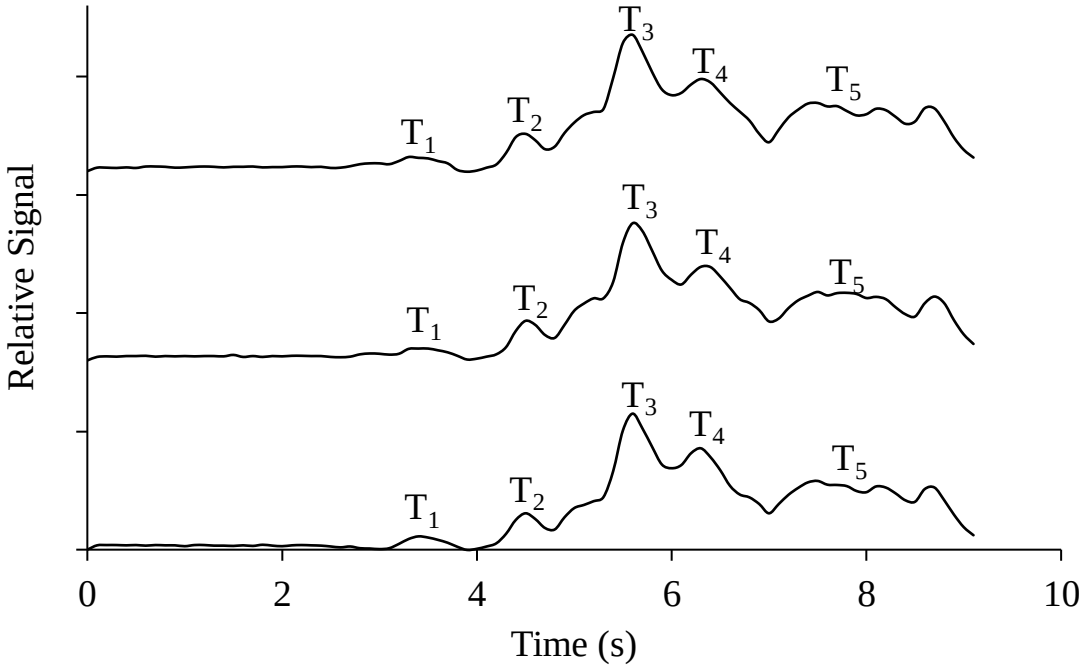

Figure 5-14 (a) The scanning pattern for the actuator (snake scan) and (b) reproducible laser-wave mixing signals from the snake scan of 3 different wells with 5 x 10^{-4} M ethyl orange. The corresponding signal peaks and times along the scanning pattern are labeled.

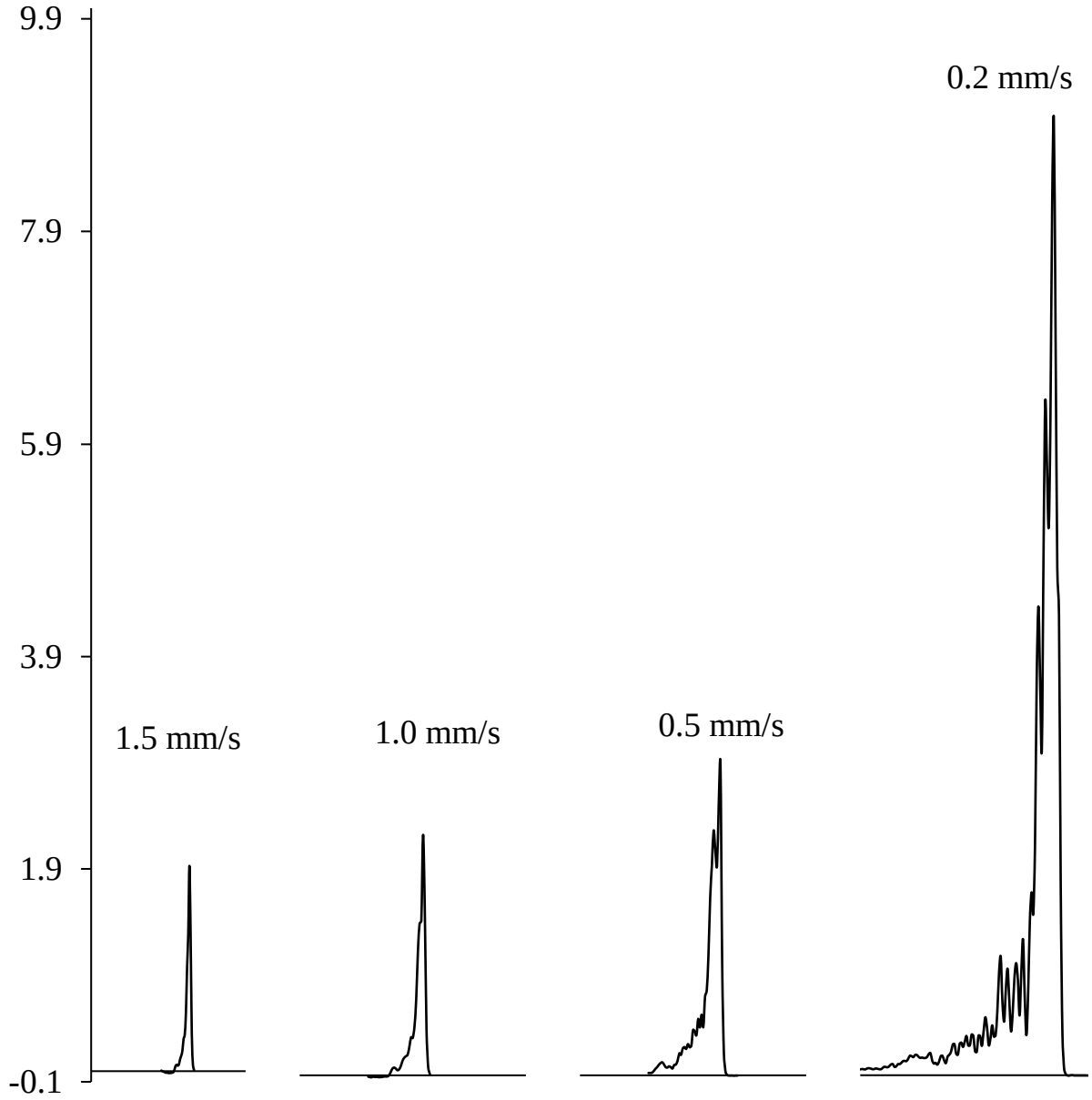

Figure 5-15 Laser wave-mixing signals from horizontal scans of a microchannel filled with 160 U/mL Chromeo P540-conjugated CA 19-9. The actuator scan rates are 1.5 mm/s, 1.0 mm/s, 0.5 mm/s, and 0.2 mm/s.

since the analyte volume at the bottom of the microchannel is round and that at the top of the microchannel is flat. However, a non-symmetrical peak could be observed if the probe laser beams do not pass through the sample volume inside the microchannel perpendicularly.

5.4.3 Utilization of antibodies to enhance detection selectivity

The utilization of antibodies in wave-mixing detection could significantly enhance detection selectivity as in other detection methods. Figure 5-16 shows direct ELISA on a microscope glass slide offers simple and fast detection with higher selectivity. Although an antibody-coated plastic microplate is not suitable for forward-scattering laser wave-mixing detection, i.e., the transmitted signal beams are collected on the other side of the plate, it is suitable for backward-scattering wave-mixing detection, i.e., the reflected signal beams are collected on the same side of the plate. In any case, a glass microscope slide offers better wave-mixing signal-to-noise ratios as compared to plastic slides. In our simplified sample holder, a Teflon tape is used to divide the glass slide into two parts to avoid cross-contamination between the color-forming complex produced by the analyte and the control. The reagents are directly drawn from the HIV-1 p24 antigen ELISA kit, and the ELISA protocol is slightly modified. APTES is used to pre-coat the glass slide to immobilize the p24 antigen. The interaction of APTES with the p24 antigen is mainly by physical adsorption mediated by surface charges on protonated amine of APTES, and the surface charges interact with the charges on the p24 antigen in aqueous solution (Aissaoui *et al*., 2011). Blocking reagent, reconstituted HIV-1 p24 detector antibody, streptavidin-peroxidase working solution, and substrate working solution are applied successively on the glass slide. Incubations and washes are conducted between these steps. The blue color is observed before adding stop solutions, and the blue color-forming complex can then be detected using 635 nm compact solid-state lasers. The stop solution containing the proprietary content can be applied to

a)

b)

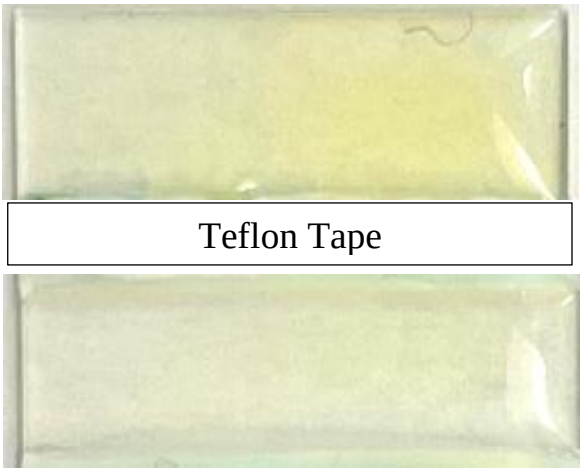

Figure 5-16 a) Photos of the color-forming complex. a) p24 antigen, detector antibody, streptavidin-peroxidase, and substrate b) p24 antigen, detector antibody, streptavidin-peroxidase, substrate, and stop solution. p24 antigen at concentration levels of 125 pg/mL (top) and 0 pg/mL (bottom) is immobilized on the glass slides.

develop a color change from blue to yellow so that blue solid-state lasers can be used for detection (HIV-1 P24 Antigen ELISA, 2021).

Figure 5-17 shows the wave-mixing signal of the color-forming complex produced by 5.2 pM p24 antigen and its control. Direct ELISA can be adopted conveniently for fast and selective detection of p24 on a microscope glass slide using laser wave mixing.

5.4.4 The Mass Detection Limit of Biomarkers

The mass detection limit of biomarkers is determined based on the concentration of the analyte and the small (usually nL to pL) probe volume used in our laser wave-mixing setup. However, a relatively larger sample volume (e.g., 50 µL -100 µL) is required to perform BCA assay (e.g., 50 µL) and ELISA (e.g., 100 µL) before using our laser wave-mixing detector. Table 5-4 summarizes the concentration and mass detection limit of CA 19-9, HER-2, and p24 antigen. Our preliminary mass detection limits using our simplified and fast wave-mixing detectors are suitable for various applications. Optimizing the optical alignment further and reducing the sample thickness on the host surface using a thinner separator instead of a Teflon tape could enhance mass sensitivity levels significantly. In addition, one could also use microchannels (20 µm) or LC or CE capillaries (75 µm) to further enhance laser wave-mixing mass detection limits, as demonstrated in our previous reports.

5.5 Conclusion

We demonstrate sensitive detection of cancer biomarkers (CA 19-9 and HER-2) and HIV-1 biomarker (p24 antigen) on simplified surface-based sample holders. Current detection methods require time-consuming and complicated labeling or sample preparation steps. Nonlinear laser wave-mixing detection methods offer significant advantages, including excellent sensitivity, small sample requirements, short optical path length and thin samples, and portable, inexpensive detector

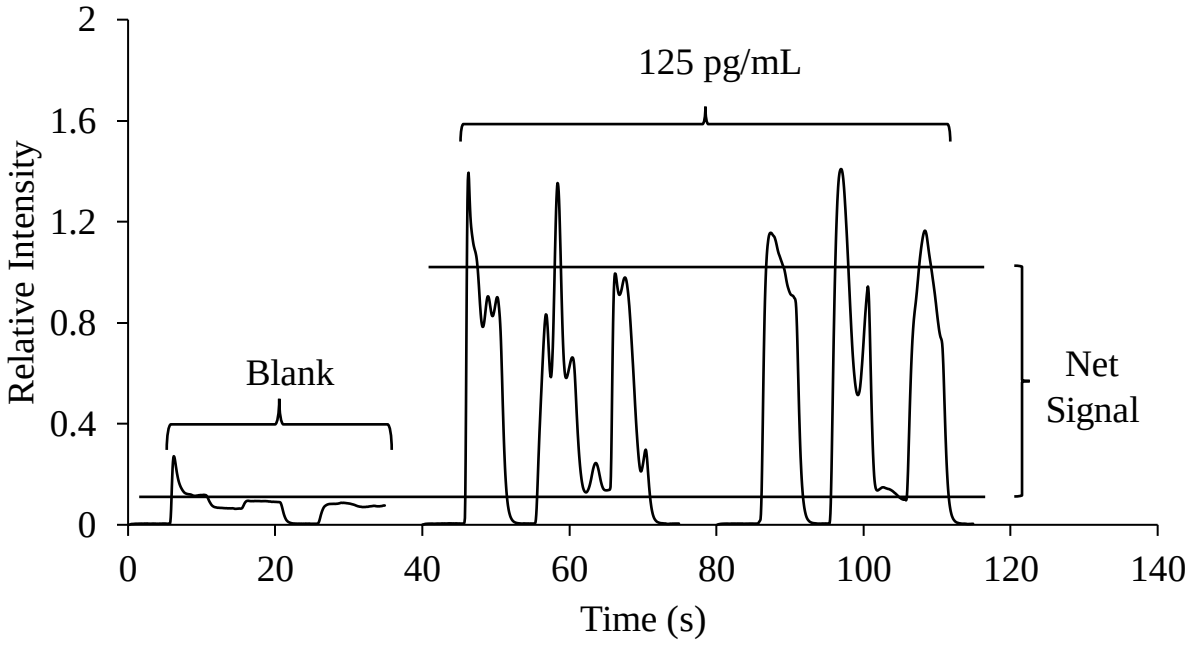

Figure 5-17 Laser wave-mixing signals obtained from the color-forming complex (p24 antigen, detector antibody, streptavidin-peroxidase, substrate, and stop solution) in the HIV-1 p24 antigen ELISA kit. Concentration levels of the p24 antigen are 0 pg/mL (blank) and 125 pg/mL (analyte).

Table 5-4 Laser wave mixing concentration and mass detection limits for CA 19-9, HER-2, and p24 antigen.

	Concentration Sensitivity	Probe Volume*	Mass Detection Limit Based on Probe Volume
CA 19-9	160 U/mL	0.50 nL	670 attomole
HER-2	40 ng/mL	0.16 nL	91 zeptomole
p24 antigen	125 pg/mL	0.20 nL	1.0 zeptomole

*Analyte probe volume depends on the probe laser diameter and the sample thickness.

designs. The coherent laser-like wave-mixing signal beam can be collected with virtually 100% efficiency and a high signal-to-noise ratio. The signal has a quadratic dependence on the analyte concentration, and hence, smaller changes can be detected more effectively. Since wave mixing is an absorption-based method, we could use both fluorophore (e.g., Chromeo P540) and chromophore labels (e.g., QSY 7). Preliminary mass detection limits of 680 attomoles, 91 zeptomoles, and 1.0 zeptomoles are reported for CA 19-9, HER-2, and p24 antigen. Since the wave-mixing probe volume is small (nL to pL), it is inherently suitable for microfluidics or microarray systems. The utilization of antibodies can further enhance detection selectivity. The simplified surface-based wave-mixing detection allows portable detectors for field use for a range of applications, including the detection of viruses and biomarkers.

5.6 Acknowledgement

Chapter 5, in part, is currently being prepared for submission for publication of the material. Jie Liang, and William G. Tong, 2023. The dissertation author was the primary investigator and author of this manuscript.

We acknowledge partial support of this work by the U.S. Department of Homeland Security Science and Technology Directorate, the U.S. Department of Defense, the Army Research Office, NSF, NIH (R01), and NIGMS IMSD (2R25GM058906).

5.7 Reference

Aggarwal, R. L., & Fan, T. Y. (2005). Thermal diffusivity, specific heat, thermal conductivity, coefficient of thermal expansion, and refractive-index change with temperature in AgGaSe_2. *Applied Optics*, *44*(13), 2673. https://doi.org/10.1364/ao.44.002673

Aissaoui, N., Bergaoui, L., Landoulsi, J., Lambert, J. F., & Boujday, S. (2011). Silane Layers on Silicon Surfaces: Mechanism of Interaction, Stability, and Influence on Protein Adsorption. *Langmuir*, *28*(1), 656–665. https://doi.org/10.1021/la2036778

Bhushan, A., Gonsalves, A., & Menon, J. U. (2021). Current State of Breast Cancer Diagnosis, Treatment, and Theranostics. *Pharmaceutics*, *13*(5), 723. https://doi.org/10.3390/pharmaceutics13050723

Biancotto, A., Brichacek, B., Chen, S., Fitzgerald, W., Lisco, A., Vanpouille, C., Margolis, L., & Grivel, J. (2009). A highly sensitive and dynamic immunofluorescent cytometric bead assay for the detection of HIV-1 p24. *Journal of Virological Methods*, *157*(1), 98–101. https://doi.org/10.1016/j.jviromet.2008.11.013

Brescia, P., & Banks, P. (2021). In-situ Micro-Volume Bicinchoninic Acid Protein Assay. *Agilent Technologies, Inc.* (No. 5994-2609EN). Retrieved December 6, 2022, from https://www.agilent.com/cs/library/applications/microvolume-bicinchoninic-acid-protein-assay-5994-2609EN-agilent.pdf

Chuah, Y. J., Kuddannaya, S., Lee, M. H. A., Zhang, Y., & Kang, Y. (2015). The effects of poly(dimethylsiloxane) surface silanization on the mesenchymal stem cell fate. *Biomaterials Science*, *3*(2), 383–390. https://doi.org/10.1039/c4bm00268g

Didar, T. F., Foudeh, A. M., & Tabrizian, M. (2011). Patterning Multiplex Protein Microarrays in a Single Microfluidic Channel. *Analytical Chemistry*, *84*(2), 1012–1018. https://doi.org/10.1021/ac2025877

ErbB2 (HER2) Human ELISA Kit - Invitrogen. (n.d.). https://www.thermofisher.com/elisa/product/ErbB2-HER2-Human-ELISA-Kit/EHERBB2

Gajria, D., & Chandarlapaty, S. (2011). HER2-amplified breast cancer: mechanisms of trastuzumab resistance and novel targeted therapies. *Expert Review of Anticancer Therapy*, *11*(2), 263–275. https://doi.org/10.1586/era.10.226

Gamble, P., Jaroensri, R., Wang, H., Tan, F., Moran, M., Brown, T., Flament-Auvigne, I., Rakha, E. A., Toss, M., Dabbs, D. J., Regitnig, P., Olson, N., Wren, J. H., Robinson, C., Corrado, G. S., Peng, L. H., Liu, Y., Mermel, C. H., Steiner, D. F., & Chen, P. H. C. (2021). Determining breast cancer biomarker status and associated morphological features using deep learning. *Communications Medicine*, *1*(1). https://doi.org/10.1038/s43856-021-00013-3

Gohring, J., Dale, P. S., & Fan, X. (2010). Detection of HER2 breast cancer biomarker using the opto-fluidic ring resonator biosensor. *Sensors and Actuators B-Chemical*, *146*(1), 226–230. https://doi.org/10.1016/j.snb.2010.01.067

Gray, E. R., Bain, R., Varsaneux, O., Peeling, R. W., Stevens, M. M., & McKendry, R. A. (2018). p24 revisited. *AIDS*, *32*(15), 2089–2102. https://doi.org/10.1097/qad.0000000000001982

Groeneveld, I. F., Kanelli, M., Ariese, F., & Van Bommel, M. R. (2022). Parameters that affect the photodegradation of dyes and pigments in solution and on substrate – An overview. *Dyes and Pigments*, *210*, 110999. https://doi.org/10.1016/j.dyepig.2022.110999

Guerrero-Esteban, T., Gutiérrez-Sánchez, C., García-Mendiola, T., Revenga-Parra, M., Pariente, F., & Lorenzo, E. (2021). Bifunctional carbon nanodots for highly sensitive HER2 determination based on electrochemiluminescence. *Sensors and Actuators B-Chemical*, *343*, 130096. https://doi.org/10.1016/j.snb.2021.130096

Heilweil, E. J., & Hochstrasser, R. M. (1985). Nonlinear spectroscopy and picosecond transient grating study of colloidal gold. *The Journal of Chemical Physics*, *82*(11), 4762–4770. https://doi.org/10.1063/1.448693

Hicks, D. G., Buscaglia, B., Goda, H., McMahon, L., Natori, T., Turner, B., Soukiazian, A., Okada, H., & Nakano, Y. (2018). A novel detection methodology for HER2 protein quantitation in formalin-fixed, paraffin embedded clinical samples using fluorescent nanoparticles: an analytical and clinical validation study. *BMC Cancer*, *18*(1). https://doi.org/10.1186/s12885-018-5172-1

HIV-1 p24 Antigen ELISA. (2021, June 14). ZeptoMatrix. Retrieved December 8, 2022, from https://www.zeptometrix.com/media/documents/PI0801111.pdf

Jawad, Z. A. R., Theodorou, I. G., Jiao, L. R., & Xie, F. (2017). Highly Sensitive Plasmonic Detection of the Pancreatic Cancer Biomarker CA 19–9. *Scientific Reports*, 7(1). https://doi.org/10.1038/s41598-017-14688-z

Joint United Nations Progamme on HIV/AIDS. (2022). *Global HIV & AIDS statistics* [Fact sheet] http://www.unaids.org/en/resources/fact-sheet.

Kim, J. H., Chi, D., Kim, S. W., Choi, C. K., & Rhee, C. (1995). The effects of grating period and heating duration time on the measurement of thermal diffusivity of liquids using photothermal grating spectroscopy. *Measurement*, 15(3), 159–164. https://doi.org/10.1016/0263-2241(94)00043-7

Kosaka, P. M., Pini, V., Calleja, M., & Tamayo, J. (2017). Ultrasensitive detection of HIV-1 p24 antigen by a hybrid nanomechanical-optoplasmonic platform with potential for detecting HIV-1 at first week after infection. *PLOS ONE*, *12*(2), e0171899. https://doi.org/10.1371/journal.pone.0171899

Lee, T., Teng, T. Z. J., & Shelat, V. G. (2020). Carbohydrate antigen 19-9 — tumor marker: Past, present, and future. *World Journal of Gastrointestinal Surgery*, *12*(12), 468–490. https://doi.org/10.4240/wjgs.v12.i12.468

Loyez, M., Lobry, M., Hassan, E. S., DeRosa, M. C., Caucheteur, C., & Wattiez, R. (2021). HER2 breast cancer biomarker detection using a sandwich optical fiber assay. *Talanta*, *221*, 121452. https://doi.org/10.1016/j.talanta.2020.121452

Łukasiewicz, S., Czeczelewski, M., Forma, A., Baj, J., Sitarz, R., & Stanisławek, A. (2021). Breast Cancer—Epidemiology, Risk Factors, Classification, Prognostic Markers, and Current Treatment Strategies—An Updated Review. *Cancers*, *13*(17), 4287. https://doi.org/10.3390/cancers13174287

Luo, J., Liang, D., Li, X., Liu, S., Deng, L., Ma, F., Wang, Z., Yang, M., & Chen, X. (2021). Photoelectrochemical detection of human epidermal growth factor receptor 2 (HER2) based on Co3O4-ascorbic acid oxidase as multiple signal amplifier. *Mikrochimica Acta*, *188*(5). https://doi.org/10.1007/s00604-021-04829-7

Macchia, E., Sarcina, L., Picca, R. A., Manoli, K., Di Franco, C., Scamarcio, G., & Torsi, L. (2019). Ultra-low HIV-1 p24 detection limits with a bioelectronic sensor. *Analytical and Bioanalytical Chemistry*, *412*(4), 811–818. https://doi.org/10.1007/s00216-019-02319-7

McGuigan, A., Kelly, P., Turkington, R. C., Jones, C., Coleman, H. G., & McCain, R. S. (2018). Pancreatic cancer: A review of clinical diagnosis, epidemiology, treatment and outcomes. *World Journal of Gastroenterology*, *24*(43), 4846–4861. https://doi.org/10.3748/wjg.v24.i43.4846

Mitri, Z., Constantine, T., & O'Regan, R. (2012). The HER2 Receptor in Breast Cancer: Pathophysiology, Clinical Use, and New Advances in Therapy. *Chemotherapy Research and Practice*, *2012*, 1–7. https://doi.org/10.1155/2012/743193

Nakatsuma, A., Kaneda, M., Kodama, H., Morikawa, M., Watabe, S., Nakaishi, K., Yamashita, M., Yoshimura, T., Miura, T., Ninomiya, M., & Ito, E. (2015). Detection of HIV-1 p24 at Attomole Level by Ultrasensitive ELISA with Thio-NAD Cycling. *PLOS ONE*, *10*(6), e0131319. https://doi.org/10.1371/journal.pone.0131319

Nardin, S., Mora, E., Varughese, F. M., D'Avanzo, F., Vachanaram, A. R., Rossi, V., Saggia, C., Rubinelli, S., & Gennari, A. (2020). Breast Cancer Survivorship, Quality of Life, and Late Toxicities. *Frontiers in Oncology*, *10*. https://doi.org/10.3389/fonc.2020.00864

Park, W., Chawla, A., & O'Reilly, E. M. (2021). Pancreatic Cancer. *JAMA*, *326*(9), 851. https://doi.org/10.1001/jama.2021.13027

Roskoski, R. (2014). The ErbB/HER family of protein-tyrosine kinases and cancer. *Pharmacological Research*, *79*, 34–74. https://doi.org/10.1016/j.phrs.2013.11.002

Savarese, M., Aliberti, A., De Santo, I., Battista, E., Causa, F., Netti, P. A., & Rega, N. (2012). Fluorescence Lifetimes and Quantum Yields of Rhodamine Derivatives: New Insights from Theory and Experiment. *The Journal of Physical Chemistry A*, *116*(28), 7491–7497. https://doi.org/10.1021/jp3021485

Schwetz, T. A., & Fauci, A. S. (2018). The Extended Impact of Human Immunodeficiency Virus/AIDS Research. *The Journal of Infectious Diseases*. https://doi.org/10.1093/infdis/jiy441

Shamshirian, A., Aref, A. R., Yip, G. W., Ebrahimi Warkiani, M., Heydari, K., Razavi Bazaz, S., Hamzehgardeshi, Z., Shamshirian, D., Moosazadeh, M., & Alizadeh-Navaei, R. (2020). Diagnostic value of serum HER2 levels in breast cancer: a systematic review and meta-analysis. *BMC Cancer*, *20*(1). https://doi.org/10.1186/s12885-020-07545-2

Siegel, R. L., Miller, K. D., Fuchs, H. E., & Jemal, A. (2021). Cancer Statistics, 2021. *CA: A Cancer Journal for Clinicians*, *71*(1), 7–33. https://doi.org/10.3322/caac.21654

Sirohi, R. S. (2017). *Introduction to Optical Metrology*. Amsterdam University Press.

Sypabekova, M., Amantayeva, A., Vangelista, L., González-Vila, Á., Caucheteur, C., & Tosi, D. (2022). Ultralow Limit Detection of Soluble HER2 Biomarker in Serum with a Fiber-Optic Ball-Tip Resonator Assisted by a Tilted FBG. *ACS Measurement Au*, *2*(4), 309–316. https://doi.org/10.1021/acsmeasuresciau.2c00008

Torniainen, K., Tammilehto, S., & Ulvi, V. (1996). The effect of pH, buffer type and drug concentration on the photodegradation of ciprofloxacin. *International Journal of Pharmaceutics*, *132*(1–2), 53–61. https://doi.org/10.1016/0378-5173(95)04332-2

Vander Wal, R., Holmes, B., Jeffries, J., Danehy, P., Farrow, R., & Rakestraw, D. (1992). Detection of HF using infrared degenerate four-wave mixing. *Chemical Physics Letters*, *191*(3–4), 251–258. https://doi.org/10.1016/0009-2614(92)85296-m

Vani, R., & Sangeetha, M. (2012). Survey on H.264 Standard. *Lecture Notes of the Institute for Computer Sciences, Social Informatics and Telecommunications Engineering*, 397–410. https://doi.org/10.1007/978-3-642-27317-9_41

World Health Organization. (2022). *HIV*. [Fact sheet]. https://www.who.int/news-room/fact-sheets/detail/hiv-aids